

# **Drivers of Marine Heatwaves in the North Pacific Inferred from Adjoint Sensitivities**

Dissertation

with the aim of achieving a doctoral degree

at the Faculty of Mathematics, Informatics and Natural Sciences Department

of Earth Sciences

at Universität Hamburg

submitted by

**Xiaoxue Wang**

from Harbin, China

Hamburg, 2025

Department of Earth Sciences

Date of Oral Defense:

26.06.2025

Reviewers:

Prof. Dr. Detlef Stammer

Dr. Armin Köhl

Members of the examination commission:

Chair Prof. Dr. Detlef Stammer

Dr. Armin Köhl

Dr. Johann Jungclaus

Prof. Dr. Elisa Schaum

Prof. Dr. Christian Beer

Chair of the Subject Doctoral Committee

Earth System Sciences:

Prof. Dr. Hermann Held

Dean of Faculty MIN:

Prof. Dr.-Ing. Norbert Ritter

## Abstract

Marine Heatwaves (MHWs) in the North Pacific (NP) have attracted widespread attention due to their adverse effects. Recent studies have focused on understanding the mechanisms driving NP MHWs, particularly during events like the significant 2014-2016 Northeast Pacific (NEP) MHWs, to improve early forecasting and reduce their negative effects. This study investigates the drivers of MHWs using the Estimating the Circulation and Climate of the Ocean technology, which incorporates the Massachusetts Institute of Technology general circulation model along with its adjoint model. The adjoint method enables efficient detection of causal relationships by tracing observed effects back to potential causes. Two main target regions have been selected ( $145^{\circ} \sim 160^{\circ}\text{W}$ ,  $48^{\circ} \sim 56^{\circ}\text{N}$ ;  $163^{\circ} \sim 169^{\circ}\text{E}$ ,  $52^{\circ} \sim 56^{\circ}\text{N}$ ) based on year-long anomalous warming in the upper 100 m of the ocean to identify the drivers influencing the NEP MHWs, Northwest Pacific (NWP) MHWs. For NEP MHWs, atmospheric forcing anomalies that occur within three months before an MHW year are particularly critical in driving these events. Local turbulent surface heat flux is identified as the main factor, responsible for up to 80% of temperature anomalies during MHW years, with air temperature, specific humidity, and longwave radiation being significant contributors. Horizontal winds, which are associated with a deepened or shallowed mixed layer, are less influential in the NEP, where they appear to precondition MHWs through climate oscillations rather than directly causing them. In contrast, NWP MHWs are greatly affected by wind-related processes and are quite responsive to the background conditions, which do not significantly impact the NEP MHWs. In the NWP, both heat flux and wind-induced vertical advection play dominant roles. Air temperature, horizontal winds, and radiative flux each contribute approximately 30%, while specific humidity, which contributes significantly to the NEP, has the smallest contribution ( $\sim 10\%$ ) to the NWP. These complex mechanisms highlight the coupled processes and regional specificity in understanding and predicting MHWs across the NP and the globe.

## Zusammenfassung

Marine Hitzewellen (MHWs) im Nordpazifik (NP) haben aufgrund ihrer negativen Auswirkungen große Aufmerksamkeit erregt. Neueste Studien konzentrieren sich darauf, die Mechanismen zu verstehen, die die MHWs im NP antreiben, insbesondere während Ereignissen wie den bedeutenden Hitzewellen im Nordostpazifik (NEP) von 2014 bis 2016. Ziel ist es, die Frühprognose zu verbessern und ihre negativen Effekte zu verringern. Diese Studie untersucht die Treiber von MHWs unter Verwendung der Technologie zur Schätzung der Zirkulation und des Klimas des Ozeans. Diese umfasst das allgemeine Zirkulationsmodell des Massachusetts Institute of Technology sowie dessen adjungiertes Modell. Die adjungierte Methode ermöglicht eine effiziente Erkennung kausaler Beziehungen, indem beobachtete Effekte auf mögliche Ursachen zurückverfolgt werden. Zwei Hauptzielregionen wurden ausgewählt ( $145^{\circ} \sim 160^{\circ}\text{W}$ ,  $48^{\circ} \sim 56^{\circ}\text{N}$ ;  $163^{\circ} \sim 169^{\circ}\text{E}$ ,  $52^{\circ} \sim 56^{\circ}\text{N}$ ), basierend auf einjährigen anomal warmen Oberflächenschichten bis zu 100 m Tiefe im Ozean. Ziel ist es, die Treiber zu identifizieren, die die NEP-MHWs und die MHWs im Nordwestpazifik (NWP) beeinflussen. Für NEP-MHWs sind atmosphärische Anomalien, die innerhalb von drei Monaten vor einem MHW-Jahr auftreten, besonders entscheidend für die Entstehung dieser Ereignisse. Der lokale turbulente Oberflächenwärmefluss wird als Hauptfaktor identifiziert, der bis zu 80 % der Temperaturanomalien während der MHW-Jahre verursacht. Lufttemperatur, spezifische Feuchtigkeit und langwellige Strahlung leisten dabei signifikante Beiträge. Horizontale Winde, die mit einer vertieften oder flacher gewordenen Mischschicht verbunden sind, haben im NEP einen geringeren Einfluss. Sie scheinen die MHWs durch Klimaschwankungen vorzubedingen, anstatt sie direkt zu verursachen. Im Gegensatz dazu werden die NWP-MHWs stark von windbezogenen Prozessen beeinflusst und reagieren stark auf die Hintergrundbedingungen, die NEP-MHWs nicht wesentlich beeinflussen. Im NWP spielen sowohl der Wärmefluss als auch die windbedingte vertikale Advektion eine dominierende Rolle. Lufttemperatur, horizontale Winde und Strahlungsfluss tragen jeweils etwa 30 % bei, während die spezifische Feuchtigkeit, die im NEP erheblich beiträgt, den geringsten Einfluss (~10 %) auf den NWP hat. Diese komplexen Mechanismen verdeutlichen die gekoppelten Prozesse und die regionale Spezifität im Verständnis und in der Vorhersage von MHWs im NP und weltweit.

## Abbreviations

AF	Atmospheric Forcing
ECCO	Estimating the Circulation and Climate of the Ocean
ENSO	El Niño-Southern Oscillation
EOF	Empirical Orthogonal Function
ETOPO5	Earth Topography 5-arc-min grid dataset
GM	Gent–McWilliams
KE	Kuroshio Extension
KOE	Kuroshio-Oyashio Extension
KP	Kamchatka Peninsula
KPP	K-Profile Parameterization scheme
LW	Downward Longwave Radiation
MHW	Marine Heatwave
MITgcm	Massachusetts Institute of Technology general circulation model
NEP	Northeast Pacific
NP	North Pacific
NPGO	North Pacific Gyre Oscillation
NPSH	North Pacific Subtropical High
NWP	Northwest Pacific
PDO	Pacific Decadal Oscillation
PRE	Precipitation
SH	Specific Humidity
SOMs	Self-Organizing Maps
SSH	Sea Surface Height
SSHa	Sea Surface Height anomalies
SSST	Sea Subsurface Temperature
SSSTa	Sea Subsurface Temperature anomalies
SST	Sea Surface Temperature
SSTa	Sea Surface Temperature anomalies
SW	Downward Shortwave Radiation
T2M	Air Temperature
TAF	Transformation of Algorithms in Fortran
U	Zonal Wind Velocity
V	Meridional Wind Velocity
WAF	Wave Activity Flux
WBS	Western Bering Sea

## List of Publications

The first part of the results presented in this dissertation has been accepted for publication as:

1. *Xiaoxue Wang, Armin Köhl, Detlef Stammer. Northeast Pacific Marine Heatwaves Mechanism Inferred from Adjoint Sensitivities. Journal of Climate. (accepted and in production)*

The second part of the results presented in this dissertation has been prepared for publication as:

2. *Xiaoxue Wang, Armin Köhl, Detlef Stammer. Potential Drivers of Northwest Pacific Marine Heatwaves Inferred from Adjoint Sensitivities. (to be submitted)*

# Table of Contents

<b>ABSTRACT</b> .....	<b>3</b>
<b>ZUSAMMENFASSUNG</b> .....	<b>4</b>
<b>ABBREVIATIONS</b> .....	<b>5</b>
<b>LIST OF PUBLICATIONS</b> .....	<b>6</b>
<b>1 INTRODUCTION</b> .....	<b>9</b>
<i>1.1 Motivation</i> .....	9
<i>1.2 Thesis objectives</i> .....	11
<i>1.3 Outline of the thesis</i> .....	11
<b>2 BACKGROUND</b> .....	<b>13</b>
<i>2.1 Definition of MHWs</i> .....	13
<i>2.2 Determinants of Temperature</i> .....	15
<i>2.3 Progress in MHW Research</i> .....	17
<b>3 DATA AND METHODOLOGY</b> .....	<b>25</b>
<i>3.1 Data Source</i> .....	25
<i>3.2 MITgcm</i> .....	27
<i>3.3 Adjoint Method</i> .....	33
<i>3.4 Contribution Analysis</i> .....	36
<i>3.5 Perturbation Experiments</i> .....	38
<i>3.6 Adjoint Validation</i> .....	40
<b>4 RESULTS</b> .....	<b>44</b>
<i>4.1 Northeast Pacific Marine Heatwaves Mechanism</i> .....	44
4.1.1. NEP MHW Research Region .....	45
4.1.2. NEP MHW Model Set-up .....	48
4.1.3. NEP MHW Sensitivities .....	51
4.1.4. NEP MHW Reconstruction .....	69
4.1.5. NEP MHW Forecast Potential .....	73
4.1.6. NEP Monthly MHWs.....	77
4.1.7. NEP MHW Discussion .....	80
4.1.8. NEP MHW Summary .....	83
<i>4.2 Northwest Pacific Marine Heatwaves Mechanism</i> .....	84
4.2.1. NWP MHW Research Region .....	85
4.2.2. NWP MHW Model Set-up.....	87
4.2.3. NWP MHW Sensitivities .....	89
4.2.4. NWP MHW Perturbation Experiments.....	104
4.2.5. NWP Surface MHW in July 2022.....	108
4.2.6. NWP MHW Discussion .....	113
4.2.7. NWP MHW Summary .....	115
<b>5 CONCLUSION AND DISCUSSION</b> .....	<b>116</b>
<i>5.1 Summary</i> .....	116
<i>5.2 Discussion</i> .....	118

<i>5.3 Outlook</i> .....	121
<b>REFERENCES</b> .....	125
<b>DATA AND CODE AVAILABILITY</b> .....	147
<b>ACKNOWLEDGMENTS</b> .....	148

# 1 Introduction

## 1.1 Motivation

In the past, heatwaves on land have received more attention due to their immediate effects on human society (e.g. wildfires, [Jain et al., 2024](#)). There have been numerous land heatwave events in recent decades, with the 2003 heatwave being particularly notable due to its severe effects ([Russo et al., 2015](#); [Christidis et al., 2015](#); [Stott et al., 2004](#)). However, there has been an increasing emphasis on marine heatwaves (MHWs) recently owing to their huge impacts on the ecosystems ([Frölicher & Laufkötter, 2018](#)). MHWs have been linked to adverse effects such as coral bleaching ([Wyatt et al., 2023](#)), changes in species distributions ([Welch et al., 2023](#)), and negative effects on the health of fish, marine mammals, and other marine organisms ([Fazli et al., 2025](#); [Joyce et al., 2023](#); [Pearce & Feng, 2013](#)). Additionally, MHWs can influence human health ([Campbell et al., 2018](#)) and food productivity by affecting the reproduction and growth of plankton ([Zhan et al., 2024](#); [Chauhan et al., 2023](#)). These phenomena also pose risks to infrastructure ([Hartog et al., 2023](#); [Smith et al., 2021](#)).

An MHW event is essentially a phenomenon of abnormally high ocean temperatures, including both ocean surface and subsurface layers. The occurrence and intensity of these anomalous temperature events have been rising ([Mohamed et al., 2022](#); [Perkins & Lewis, 2020](#); [Schlegel et al., 2017](#)), as a consequence of climate change ([Capotondi et al., 2024](#); [Spillman et al., 2021](#); [Intergovernmental Panel on Climate Change \(IPCC\), 2023](#)). This trend is expected to exacerbate further during the coming decades based on the climate projections ([Dubey & Kumar, 2023](#); [Amaya et al., 2021](#); [Qiu et al., 2021](#); [Hayashida et al., 2020](#); [Plecha & Soares, 2020](#); [Alexander et al., 2018](#)). Multiple studies have been carried out to determine the drivers of MHWs, with heat budget analysis being a commonly employed method ([Athanase et al., 2024](#); [Bian et al., 2023](#); [Wang et al., 2022c](#)). In addition, some researchers employ statistical analysis ([Zhang et al., 2024a](#)), wave activity flux (WAF, [Shi et al., 2024a](#); [Ha et al., 2022](#)), and self-organizing maps (SOMs, [Oliver et al., 2018](#); [Schlegel et al., 2017](#)) to analyze the potential remote drivers and to detect the subsurface MHWs. The first goal of this research is to build on existing methods by investigating the potential drivers of these extreme events using a novel methodology from a different perspective, and to provide predictive signals or, at the very least, enhance the understanding of such phenomena to mitigate their adverse impacts.

Among all MHWs, the North Pacific (NP) region is notably affected due to its significant impact on ecosystems and their overall functioning ([Welch et al., 2023](#)). This area hosts some of the most productive marine environments in the world and supports diverse coastal communities, making it particularly vulnerable to changes in temperature. Additionally, the NP is also critical to global climate systems, mainly due to the interactions that occur between the ocean and the atmosphere. For instance, Northeast Pacific (NEP) MHWs can be modulated by the Pacific Decadal Oscillation (PDO, [Ren et al., 2023](#)). The North Pacific Oscillation can further modulate the stratospheric polar vortex, as well as influence the El Niño–Southern Oscillation (ENSO) and other climate patterns ([Sung, 2025](#)). Yet, the drivers of NP MHWs including atmospheric forcing (AF), ocean circulation shifts, and global warming remain incompletely understood, limiting the ability to predict.

However, recent research on MHWs has predominantly concentrated on the NEP ([Fig. 1](#), [Song et al., 2023b](#); [Ren et al., 2023](#); [Chen et al., 2023](#); [Capotondi et al., 2022](#); [Amaya et al., 2020](#)), with relatively fewer studies examining the Northwest Pacific (NWP; [Noh et al., 2023](#); [Li et al., 2023](#); [Du et al., 2022](#)). Most studies targeting the NWP have focused on the South China Sea and East Sea ([Liu et al., 2022](#); [Oliver et al., 2021](#); [Yao & Wang, 2021](#)). Notably, NEP MHWs are interconnected with NWP dynamics, as highlighted by [Silva & Anderson \(2023\)](#), who demonstrated that NEP MHWs are linked to Kuroshio Extension (KE) variability through atmospheric teleconnections. Also, recent research has primarily focused on surface MHWs, while subsurface MHWs are increasingly being recognized for their significant ecological and climatic effects ([Guo et al., 2024](#); [McAdam et al., 2023](#); [Sun et al., 2023](#)). Despite this emerging interest, there are still comparatively fewer studies focusing on the physical drivers of subsurface MHWs. Importantly, subsurface MHWs can be more intense and long-lasting than surface ones ([Fragkopoulou et al., 2023](#)). The secondary objective of this study is to examine whether the drivers of MHWs are uniformly consistent across the NP. Specifically, this study aims to determine whether the mechanisms underlying long-lasting subsurface MHWs in the NWP differ from those in the NEP. Meanwhile, certain residual terms in the NWP remain difficult to explain through conventional heat budget analysis ([Song et al., 2024](#)). This study will also explore whether using an adjoint method can provide alternative insights into these unresolved phenomena.

In addition to the study region analyzed by Song et al. ([2024](#)), the year 2022 witnessed numerous significant MHWs ([Oh et al., 2023](#); [Zhao et al., 2023](#)) within the context of elevated warming. According to the annual report from the National Centers for Environmental Information ([NCEI, 2022a](#)), 2022 exhibited the highest ocean heat content levels in both the Southern Pacific Ocean and the NP Ocean since 1955 ([Cheng et al., 2023](#)). As mean warming contributes to trends in MHWs across approximately two-thirds of the world's oceans ([Oliver, 2019](#); [Xu et al., 2022](#)), this study will also include a preliminary discussion and outlook of potential connections between NP MHWs and elevated warm conditions in the NP. For instance, there are notable changes in the dominant modes of sea surface temperature (SST) variability ([Werb & Rudnick, 2023](#)). It is essential to note that while MHWs are influenced by global warming, they also contribute to climate change in turn.

## 1.2 Thesis objectives

In this study, by using an adjoint ocean model, the following two research questions will be investigated:

- a. What is the main atmospheric driver for the NEP MHWs? Are the results comparable to those obtained through heat budget analysis or other methods?
- b. Are MHW mechanisms in the NWP different from those in the NEP? Can the results explain the unresolved residual terms in the previous study?

## 1.3 Outline of the thesis

This dissertation is structured as follows: Following this brief introduction ([Chapter 1](#)), [Chapter 2](#) provides the background information relevant to the study fields. [Chapter 3](#) describes the data sources and methods utilized, including the model setup, adjoint method and its validation, contribution analysis, and perturbation experiments. [Chapter 4](#) presents the main results in two sections: the first, on NEP MHWs, has been accepted by the Journal of Climate for publication, and the second, on NWP MHWs, has been prepared for submission. [Chapter 5](#) concludes the dissertation, including further discussions of the results and directions for future research.

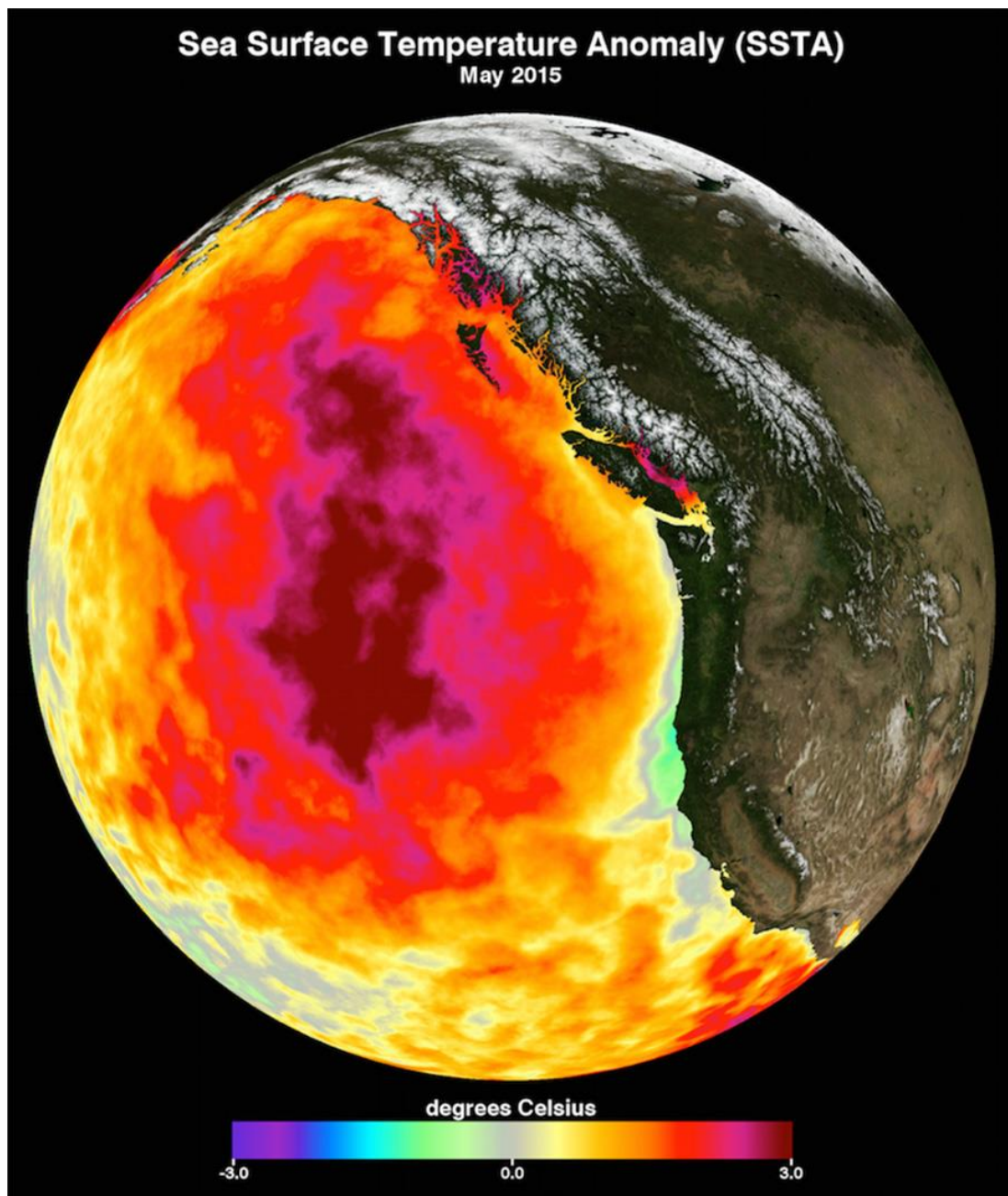


Fig. 1. An image shows the monthly average sea surface temperature for May 2015. The image is taken from NASA Physical Oceanography Distributed Active Archive Center ([Gentemann et al., 2017](#)).

## 2 Background

### 2.1 Definition of MHWs

When discussing MHWs (a term first introduced by [Pearce et al., 2011](#)), it refers specifically to anomalously high temperatures in the ocean. Defining heatwave events with precision across various locations and time scales has been challenging until the introduction of percentile-based indices ([Perkins & Alexander, 2013](#); [Alexander et al., 2006](#)). Subsequent studies have provided more accurate delineations by utilizing particular research occurrences as the basis for their definitions ([Russo et al., 2015](#); [Stefanon et al., 2012](#)). Hobday et al. ([2016, 2018](#)) further define MHWs as deviations from expected temperatures for distinct locations and persist for a certain duration, a definition that has gained broad recognition within the community ([Fig. 2.1](#)). MHWs can be further categorized into four distinct classes according to how much temperatures exceed local climatological averages.

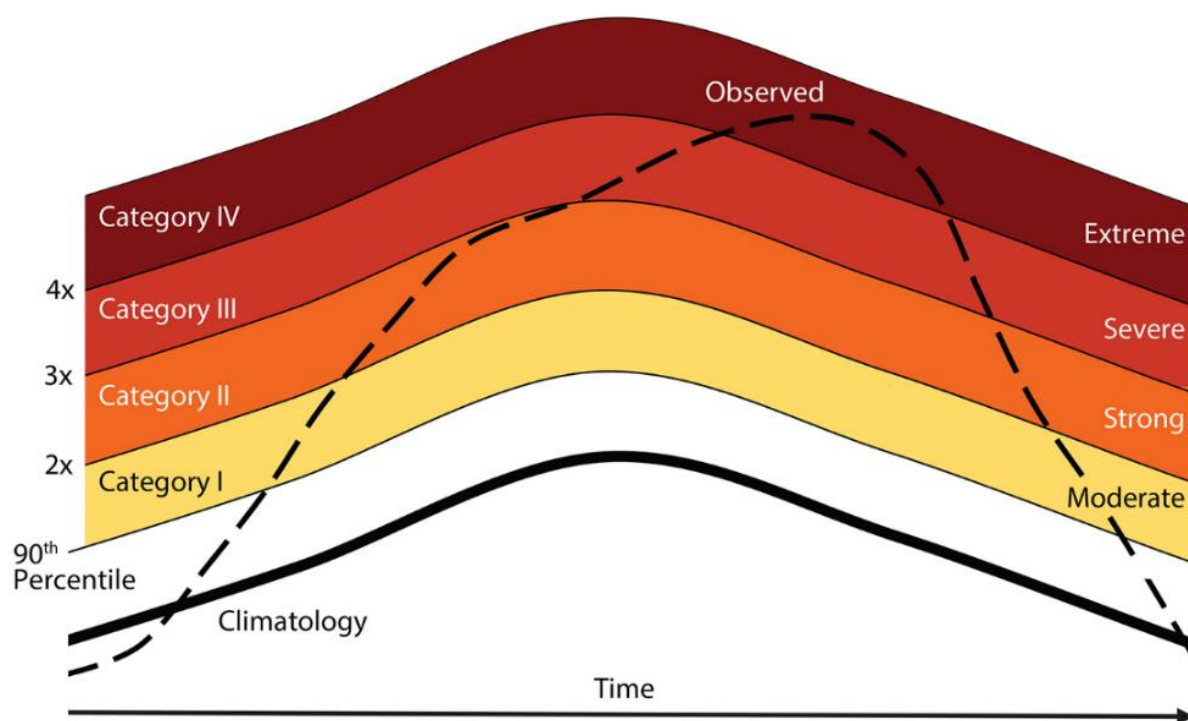


Fig. 2.1. Categorization schematic for MHWs. The image is taken from Hobday et al. ([2018](#)).

The most notable MHW is referred to as Blob, a name given by Bond et al. (2015). It was first observed in October 2013 (Peterson et al., 2015) and continued to spread throughout 2014 and 2015 (Fig. 1). This event was characterized by anomalously warm water that dominated much of the NEP region off the North American coast. In 2019, Blob 2.0 occurred in the same region of the NEP primarily driven by a multi-month reduction in the strength of the North Pacific Subtropical High (NPSH, Amaya et al., 2020). The term Southern Blob is also employed to refer to the warming of the upper ocean in the subtropical southwest Pacific (Garreaud et al., 2021).

Several studies have investigated the driving mechanism behind seasonal, monthly (Capotondi et al., 2022; Chen et al., 2021; Shi et al., 2024a; Silva & Anderson, 2023; Xu et al., 2022) or daily (Kajtar et al., 2022; Li et al., 2020; Oliver, 2019; Zschenderlein et al., 2019) MHWs according to their definitions by using either heat budget analysis or composite and statistical analysis. Few studies investigate NEP MHWs over extended time scales, particularly regarding the anomalously warm SST observed in 2014, which persisted for more than 2 years (Schmeisser et al., 2019). MHWs on long-time scales should not be overlooked, as they can last for multiple years and have a lasting impact on marine ecosystems.

For long-term MHWs, the definition is established by NOAA Physical Sciences Laboratory (Jacox et al., 2020, 2022), which states that MHW occurs when SST anomalies (SSTa, with respect to the 1991 - 2020 monthly climatology) exceed a specific threshold for every month of the year. These thresholds are determined as the 90th percentile of SSTa within a 3-month period (for example, for January MHWs, the 90th percentile of all December to February SSTa). The threshold may be adjusted to the 95th or 99th percentile, depending on the severity of the extreme event being analyzed.

Sun et al. (2023) demonstrate a significant increase in subsurface MHWs associated with subsurface mean-state warming over the past three decades. They emphasize the necessity for further research on subsurface MHWs. According to the percentile-based definition, the occurrence of subsurface marine heatwaves can be determined using a threshold derived from sea subsurface temperature anomalies (SSSTa).

However, the definitions of MHWs are still being debated (Capotondi et al., 2024), particularly regarding the selection of a baseline for establishing climatology and the treatment of climate signals. Smith et al. (2025) examine different baseline choices involving a fixed

baseline, a shifting baseline, a detrended baseline, and an adaption-adjusted baseline and indicate markedly varied trends in the characteristics of MHW in a warming climate in terms of different baselines. In this study, the warming trend is not removed, as the detected AF inherently includes this warming trend. The effect of global warming on AF is not considered separately. The decision to use a fixed or moving baseline, or whether to apply detrending, should be tailored to the specific research question ([Oliver et al., 2021](#)). For instance, many species are at risk from both short-term temperature extremes and prolonged warming trends. Adapting to gradual temperature changes may take several generations ([Smith et al., 2023](#)). Therefore, detrending could underestimate the ecological pressures on these species by separating episodic extremes from the ongoing climate changes they must deal with over time.

## 2.2 Determinants of Temperature

The ocean occupies approximately seventy percent of the Earth's area and is continuously dynamic. Consequently, air-sea interactions play a crucial role in variations in oceanic conditions. The temperature within the surface mixed layer (normally the top 200 m), which is directly influenced by atmospheric conditions, is often assumed to be mixed and homogeneous to a certain degree. This layer is affected by various factors ([Fig. 2.2](#)), including surface winds, waves, and currents that mix the upper water and facilitate the distribution of heat throughout the layer. The ocean absorbs incoming solar energy and subsequently transfers heat and moisture to the atmosphere, thereby fueling atmospheric circulation. Once in motion, the atmosphere further influences ocean circulation through the exchange of momentum at the air-sea interface, which generates waves and currents. The NP is influenced by several key ocean currents, including the warm Kuroshio Current, cold California, and Oyashio Currents, as well as the NP and Alaskan Currents, which together shape its climate, marine ecosystems, and weather patterns.

This research is based on physical oceanography and biological effects (lower right in [Fig. 2.2](#)) are not taken into account. Therefore, AF can be utilized as an external input to an ocean model, allowing us to observe how temperature responds to AF change. AF can be simplified as the sum of heat flux components, including downward shortwave radiation (SW), downward

longwave radiation (LW), sensible heat flux, and latent heat flux, along with wind-induced processes (e.g. advection, diffusion, convection), all incorporated within the numerical model.

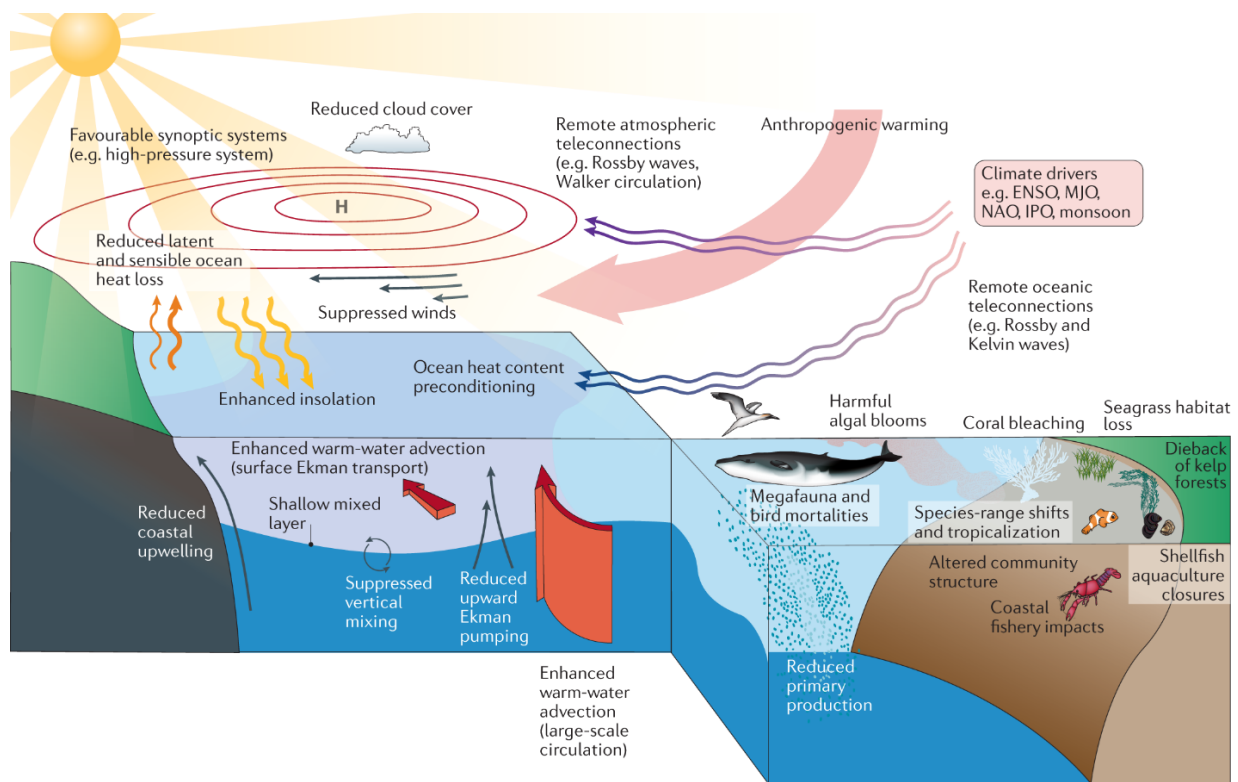


Fig. 2.2. A schematic illustration of various drivers and impacts of MHWs. The image is taken from Holbrook et al. (2020).

These processes can be calculated through mixed-layer heat budget analysis (Fig. 2.3, Moisan & Niiler, 1998; Oliver et al., 2021). The temporal variation of the vertically averaged potential temperature within the mixed layer, referred to as temperature tendency, results from a combination of several physical processes. These include air-sea exchanges, advection by both mean currents and eddies, as well as horizontal and vertical mixing. Additionally, the mixing of deeper water into the mixed layer through entrainment plays a less important role which is often considered as part of the residual term. Horizontal advection can influence local temperature changes by transporting horizontal flows that occur across a temperature gradient and mixing is commonly associated with diffusive flux. The net air-sea heat fluxes are the sum of the radiative heat flux (net downward SW + net upward LW) and turbulent heat flux (sensible heat flux + latent heat flux).

$$\begin{aligned}
\underbrace{\frac{\partial \bar{T}}{\partial t}}_{\text{Temperature tendency}} &= - \underbrace{\bar{\mathbf{u}} \cdot \nabla \bar{T}}_{\text{Horizontal advection}} + \underbrace{\overline{\nabla \cdot (\kappa_h \nabla T)}}_{\text{Horizontal mixing}} - \underbrace{\frac{1}{b} \kappa_z \frac{\partial T}{\partial z} \Big|_{-b}}_{\text{Vertical mixing}} \\
&\quad - \underbrace{\left( \frac{\bar{T} - T_{-b}}{b} \right) \left( \underbrace{\frac{\partial b}{\partial t}}_{\text{MLD tendency}} + \underbrace{\mathbf{u}_{-b} \cdot \nabla b}_{\text{Lateral induction}} + \underbrace{w_{-b}}_{\text{Vertical advection}} \right)}_{\text{Entrainment}} \\
&\quad + \underbrace{\frac{Q_{\text{SW}} - Q_{\text{SW}(-b)} + Q_{\text{LW}} + Q_{\text{sens}} + Q_{\text{lat}}}{\rho c_p b}}_{\text{Air-sea heat flux}},
\end{aligned}$$

Fig. 2.3. Mixed-layer heat budget analysis equation. The image is taken from Oliver et al. (2021).

## 2.3 Progress in MHW Research

The primary focus of MHW research encompasses both surface and subsurface MHWs (Li & Hu, 2024), with attention given to their effects, underlying drivers, teleconnections, and potential predictive possibility. Numerical ocean models and statistical models are commonly employed tools for the study of MHWs. The mixed-layer heat budget analysis is the most widely used method to describe the processes that contribute to MHW formation, evolution, and decay (Oliver et al., 2021). Additionally, SOMs are also commonly utilized as they effectively cluster between atmospheric patterns (e.g. air temperature) and oceanic patterns (e.g. MHW), which are distinct yet interconnected (Schlegel et al., 2017). WAF can be used to trace the movement of energy and interact with ocean currents to change heat distribution (Ha et al., 2022; Shi et al., 2024a). Few MHW studies have employed the adjoint method for analysis, which is a robust tool for tracing sensitivity within complex systems.

### *a. The impact of MHWs*

MHWs have attracted lots of attention owing to their huge impacts on society, the economy, ecosystems, and their overall functioning since the extreme event in Western Australia in 2011 ([Smale et al., 2019](#); [Welch et al., 2023](#); [Wernberg, 2021](#); [Wernberg et al., 2016](#)). [Holbrook et al. \(2020\)](#) offer a detailed overview of the impacts of MHWs on oceanic and coastal ecosystems ([Fig. 2.2](#)). Notable effects include coral bleaching, reduced primary production, habitat destruction, and loss of biodiversity, among others. The most substantial, prolonged, and intense MHW events were found to align with reduced chlorophyll-a concentrations at both low and mid-latitudes ([Sen Gupta et al., 2020](#)). Beyond that, the intensity of extreme weather events, including tropical storms ([Choi et al., 2024](#); [Radfar et al., 2024](#)), is rising as a consequence of MHWs. MHWs are also linked to severe droughts ([Rodrigues et al., 2019](#)), extreme sea levels and coastal flooding ([Zhou & Wang, 2024](#)). In addition to their impacts on ecosystems, fisheries, and climate, MHWs also affect human health ([Campbell et al., 2018](#)) and infrastructure ([Hartog et al., 2023](#); [Smith et al., 2021](#)).

### *b. The drivers of MHWs*

The mechanisms driving MHWs are highly dependent on timescale, geographical location, and background state ([Fig. 2.4](#), [Holbrook et al., 2019](#)). MHWs with a smaller spatial extent occur more often than those covering larger areas ([Scannell et al., 2016](#)). For instance, regional upper ocean heat content changes over short timescales are primarily influenced by local ocean circulation instead of surface heat flux ([Kerry et al., 2022](#)). [Oliver \(2019\)](#) suggests changes in mean SST rather than changes in variance are the dominant drivers influencing the duration of MHW across 2/3 of the ocean and the intensity of MHW across 1/3 of the ocean. However, NEP is not present in these regions. It has been established that an increase in the variance of SSTa in NEP may be contributing to the rising frequency of extreme events ([Xu et al., 2022](#)). Additionally, the study by [Li et al. \(2023\)](#) reinforces the idea that the NWP MHW in July 2021 was governed by the warming mean state. Consequently, MHWs are projected to become more frequent, intense, and prolonged in duration ([Athanas et al., 2024](#); [Frölicher & Laufkötter, 2018](#)).

The vast majority of MHWs in the NP are governed by an anomalous atmospheric pressure system ([Sen Gupta et al., 2020](#)), i.e. NPSH. For example, NEP MHWs ([Amaya et al., 2020](#); [Bond et al., 2015](#); [Chen et al., 2023](#); [Niu et al., 2023](#)); NWP MHWs ([Du et al., 2022](#); [Pak et al., 2022](#); [Song et al., 2023a](#); [Yao et al., 2023](#); [Yao & Wang, 2021](#)). Wind speed is influenced by the strength of the pressure gradient; a stronger pressure gradient results in higher wind speeds. The persistent NPSH is consistently associated with anomalously weak wind speeds, enhanced solar insolation, and decreased oceanic heat loss.

The high pressure acting on the sea surface restricts the escape of water molecules into the atmosphere as vapor, thereby reducing the efficiency of evaporative cooling processes and decreasing the air-sea turbulent heat flux. Increased solar insolation will lead to reduced cloud cover and higher air temperatures. Weak wind speeds will result in reduced horizontal advection and vertical mixing in the upper layer of the ocean, which consequently leads to a shallower mixed layer and enhanced surface stratification. A reduction in wind speed may result in negative wind stress curls, which are a driving force for ocean currents. These negative wind stress curls induce Ekman pumping, or downwelling, causing surface water to be pushed downward. This process allows warmer water to enter from the sides, leading to a convergence and deepening of the warm surface layer. Increasing wind speed can sometimes also cause negative wind stress curls, depending on how the wind varies across different areas. If the wind speed rises more quickly in one area than in another, it creates a gradient in wind stress, which can lead to a negative curl.

Both anomalously high and low wind speeds can play a role in the development of MHWs. The 2017/18 Tasman MHW was initiated by warm water advection and persisted due to the anomalous air-sea heat flux and a shallower mixed layer ([Kajtar et al., 2022](#)). Another explanation for the 2020 NEP MHW is that it was mainly driven by abnormal southerly winds that transported increased humidity to the NEP region. This influx of humid air reduced the ocean surface latent heat release ([Ge et al., 2023](#)).

Additionally, several other factors also contribute to MHW dynamics. [Bian et al. \(2023\)](#) employ a historical simulation from a global eddy-resolving climate model to illustrate that heat flux convergence associated with oceanic mesoscale eddies is a key driver of MHW life cycles across the majority of the global ocean, especially for the growth and decay period. MHWs in the Barents Sea are significantly influenced by SST-ice feedback, which is

predominantly driven by warm surface air and decreasing sea ice ([Mohamed et al., 2022](#)). When ice melts in the Arctic Ocean, it reduces the thickness of the upper ocean layer, resulting in a higher concentration of atmospheric heat within this layer. Consequently, this process contributes to the extension and intensification of MHW in the Arctic Ocean ([Richaud et al., 2024](#)). Recent years have seen that MHWs in the NP can also be linked to increasing atmospheric concentrations of greenhouse gases ([Barkhordarian et al., 2022](#)). In addition to the weakened NPSH, the preceding anomalous winter SST can persist into the subsequent spring or summer (also known as the ocean memory of winter warming) due to anomalous heat content present in the mixed layer of the ocean ([Du et al., 2022](#); [Liu et al., 2023](#)).

Recent studies have highlighted the significance of subsurface MHWs ([Capotondi et al., 2024](#)). A shallow MHW may be restricted within the mixed layer, which can be caused by increased surface heat fluxes, oceanic transportation, or reduced mixing induced by winds. Alternatively, they can reach a relatively deep layer beneath the mixed layer. MHWs may also be reintroduced into a thickening mixed layer, leading to a delay in surface warming. This phenomenon is referred to as re-emergence.

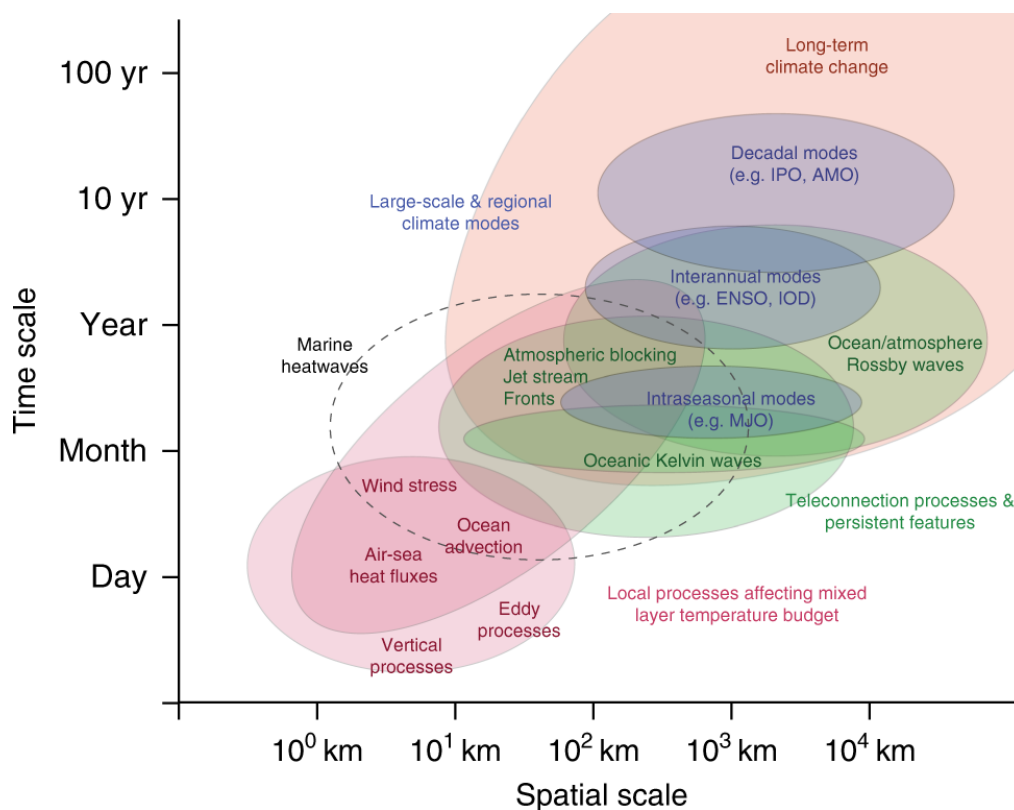


Fig. 2.4. A schematic illustration of MHW drivers and their relevant space and time scales. The image is taken from Holbrook et al. ([2019](#)).

### *c. The teleconnection of MHWs*

The key driving processes of MHW are the same as those driving the temperature changes, which are summarized in [Fig. 2.2 \(Holbrook et al., 2020\)](#). The enhancement or suppression of these physical mechanisms, whether independently or collectively, can promote or inhibit the development of MHWs. This is influenced by local air-sea interactions, feedback mechanisms, and large-scale climate variability acting both locally and remotely. Essentially, teleconnections describe how atmospheric and oceanic phenomena can influence weather patterns across large distances.

The intensity of MHWs can be influenced by local forcing factors, whereas their duration is affected by the timing of climate modes, as demonstrated by Capotondi et al. ([2022](#)). Additionally, Holbrook et al. ([2019](#), [2020](#)) summarized that the frequency, intensity, and duration of MHWs can be influenced by climate patterns and teleconnections ([Fig. 2.4](#)). For example, the intra-seasonal mode Madden–Julian Oscillation (e.g. [Liu et al., 2022](#)); the interannual mode ENSO ([Sen Gupta et al., 2020](#); [Xu et al., 2022](#)) and Indian Ocean Dipole (e.g. [Li et al., 2024](#)); the decadal mode PDO ([Ren et al., 2023](#)) and North Pacific Gyre Oscillation (NPGO; e.g. [Joh & Di Lorenzo, 2017](#)). Furthermore, the persistence of the NEP MHW can be linked to the development of a low-pressure structure occurring one year after wintertime variations in the KE ([Silva & Anderson, 2023](#)). The extratropic is highly linked to the tropics through atmospheric teleconnection ([Di Lorenzo et al., 2023](#)).

Many studies address that the westward-propagating Western Pacific Subtropical High influenced by ENSO plays a significant role in the development and persistence of the NWP MHWs (e.g. in the South China Sea, [Liu et al., 2022](#); [Tan et al., 2022](#); in the East China Sea, [Li et al., 2023](#)). Although, as previously stated, Oliver ([2019](#)) suggests that NEP is not directly influenced by mean warming, it is noted that the low-frequency NP Victoria mode, which is enhanced by the warming state, shows a strong correlation with NEP MHWs ([Ji et al., 2024](#)). Moreover, Arctic warming plays a significant role in increasing NEP MHW days. Strong Arctic warming has changed the atmospheric circulation patterns over the NEP and decreased the low-level cloud cover from late spring to early summer, leading to more MHW days ([Coumou et al., 2018](#); [Song et al., 2023b](#)). Although the mean warming is not a teleconnection, it has modified the teleconnection patterns.

WAF is also a widely used method to track the propagation of wave energy within the atmosphere and ocean ([Ha et al., 2022](#)). Shi et al. ([2024a](#)) employed WAF to illustrate that planetary wave trains, triggered by heightened rainfall and latent heat release over the Mediterranean Sea, along with decreased rainfall over the North Atlantic, can effectively transport wave energy to the NEP. Noh et al. ([2023](#)) introduced the Pacific–Japan atmospheric teleconnection pattern to explain the anomalous anticyclonic circulation and the corresponding northwestward extension of the NPSH over the NWP. Zhao & Yu ([2023](#)) emphasize the significance of cross-basin connections between the NP and North Atlantic in influencing the dynamics of NP MHWs, as inferred from WAF.

*d. The predictive skill of MHWs*

The ocean undergoes changes over months, years, and even decades, while the atmosphere changes much more quickly, within minutes, hours, or days. Consequently, the predictability of MHWs depends on the relative strength of atmospheric and oceanic contributions ([Holbrook et al., 2020](#)):

(i) Strong atmospheric and oceanic contributions: MHWs can be forecasted several months in advance by local and remote climate forcing;

(ii) Weak atmospheric and oceanic contributions: Predictability is limited to several days, often influenced by transient weather patterns or oceanic eddies;

(iii) Strong atmospheric and weak oceanic contributions: MHWs typically have a predictability lead time of one to two weeks or can be seasonal, due to atmospheric preconditioning or teleconnections;

(iv) Weak atmospheric and strong oceanic contributions: Predictability can range from months to years, facilitated by oceanic preconditioning or teleconnections.

MHWs are significantly influenced by atmospheric conditions that can be predicted, thus offering the potential for forecasting MHW events. To achieve a reliable forecast, it is essential to understand the relevant physical drivers and the interactions of processes over time ([Fig. 2.5, Holbrook et al., 2019](#)). MHWs then can be predicted through various methods in terms of timescales and types. For example, one approach involves modeling oceanic or atmospheric

dynamics to forecast atmospheric blocking patterns or ocean eddies. Another method utilizes simulations of coupled ocean-atmosphere dynamics to predict climate modes (e.g. ENSO). Additionally, predictions can be made by analyzing wave pathways resulting from wind-driven ocean perturbations.

The coupled NUIST-CFS1.0 (atmospheric component: the European Centre Hamburg Atmospheric Model version 4, [Roeckner et al., 1996](#); oceanic component: Ocean Parallélisé version 8.2, [Madec et al., 1998](#)) hindcasts can provide a forecast of both the spatial distribution and temporal changes of total MHW days with a lead time of as much as eight months. Using SOMs, Zhao et al. ([2022](#)) concluded that Sea Surface Height anomalies (SSHa) can serve as a predictive variable within a statistical modeling framework. Capotondi et al. ([2022](#)) and Li et al. ([2020](#)) also confirm that SSHa contributes significantly to the majority of MHW development in their target regions. Furthermore, the application of a mesoscale eddy-tracking method enables the prediction of individual daily MHWs in eastern Tasmania with an accuracy extending up to 7 days. While using North American Multimodel Ensemble models for predicting monthly NEP MHW in 2020, the predictive skill is limited to one month ([Ge et al., 2023](#)). The NOAA Physical Sciences Laboratory offers an experimental real-time global forecast of MHW on a monthly basis, with predictive capabilities extending up to 11.5 months in advance for research purposes ([Jacox et al., 2022](#)).

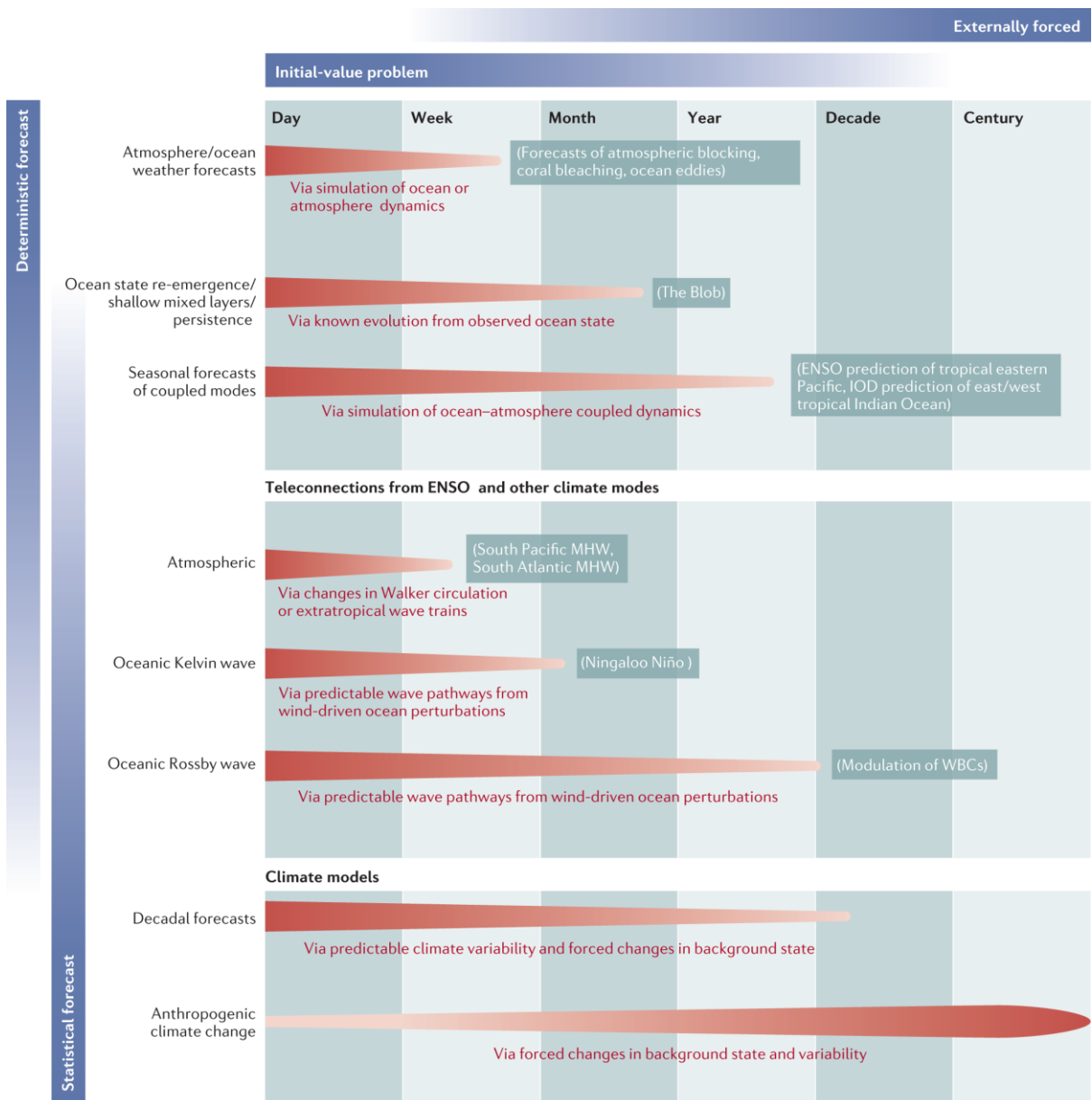


Fig. 2.5. A spectrum of MHW prediction timescales and types. The image is taken from Holbrook et al. (2020).

## 3 Data and methodology

### 3.1 Data Source

This study utilizes multiple monthly SST datasets (HadiSST v1.1, [Rayner et al., 2003](#); OISST v2.1, [Huang et al., 2021](#); ORAS5, [Zuo et al., 2019](#); MODIS-SST, [NASA Goddard Space Flight Center, 2024](#); EN4.2.2, [Good et al., 2013](#); details are in [Table. 1](#)) to represent various regions and to analyze MHWs of differing intensities. MHWs in the NWP exhibit higher intensity, necessitating the use of SST products with higher spatial resolution. In addition, as highlighted by Zhang et al. ([2024b](#)), there is a large spread in MHW assessments across various SST products in Asia and the Indo-Pacific region. Therefore, it is important to employ multiple datasets to comprehensively evaluate extreme events.

Both HadiSST and EN4 datasets are from the UK Met Office Hadley Centre. HadiSST combines historical ship-based observations and buoys, satellite-derived SST measurements, and sea ice concentration data. EN4 offers a three-dimensional perspective of ocean conditions by assimilating data from various sources, including Argo floats, conductivity-temperature-depth instruments, and other sensors, which can profile the water column. MODIS-derived SST is a widely used satellite dataset for monitoring global ocean temperatures with high spatial and temporal resolution. OISST has a higher resolution than HadiSST but is coarser than MODIS, which combines satellite observations, in-situ measurements, and ice data. The ORAS5 is a cutting-edge ocean reanalysis dataset including observational data assimilation (satellite SST, sea level anomaly, and in-situ profiles).

AF datasets are derived from the NCEP-NCAR Reanalysis 1 (NCEP-RA1; [Kalnay et al., 1996](#); [Kistler et al., 2001](#)) from 1948 to 2022 and ERA5 hourly averaged data ([Hersbach et al., 2020](#)) from 2008 to 2022 (details are provided in [Table. 2](#)). All AF datasets were averaged to a monthly resolution, aligning with the timescale of sensitivities derived from the adjoint model. This enables the direct calculation of contributions from each forcing and generates perturbations in subsequent experiments based on sensitivity solutions that are consistent with the timescales of the original forcing fields. Both datasets are utilized to drive the model and evaluate its performance. The results presented in this study are based on model runs forced with the ERA5 reanalysis. Notably, very similar results were obtained using the NCEP

reanalysis, indicating that the findings are robust and not dependent on the specific forcing fields employed. ERA5 outperforms NCEP in some cases, likely due to its use of advanced assimilation methods (Four-dimensional variational assimilation), while NCEP employs older methodologies (3D-Optimum Interpolation).

Dataset	Resolution	Access
HadiSST v1.1	1° x 1° at sea surface	<a href="https://www.metoffice.gov.uk/hadobs/hadisst/">https://www.metoffice.gov.uk/hadobs/hadisst/</a>
OISST v2.1	0.25° x 0.25° at sea surface	<a href="https://www.ncei.noaa.gov/products/optimum-interpolation-sst">https://www.ncei.noaa.gov/products/optimum-interpolation-sst</a>
ORAS5	0.25° x 0.25° with 75 levels	<a href="https://www.ecmwf.int/en/forecasts/dataset/ocean-reanalysis-system-5">https://www.ecmwf.int/en/forecasts/dataset/ocean-reanalysis-system-5</a>
MODIS-SST	4.6 km x 4.6 km at sea surface	<a href="https://www.cen.uni-hamburg.de/en/icdc/data/ocean/sst-modis.html">https://www.cen.uni-hamburg.de/en/icdc/data/ocean/sst-modis.html</a>
EN4.2.2	1° x 1° with 42 levels	<a href="https://www.metoffice.gov.uk/hadobs/en4/download.html">https://www.metoffice.gov.uk/hadobs/en4/download.html</a>

Table 1. Monthly SST and SSST datasets used for MHW detection and model evaluation.

Dataset	Horizontal Resolution	Time Resolution	Access
NCEP-RA1	1.875° x 1.875°	6-hour	<a href="https://psl.noaa.gov/data/gridded/data.ncep.reanalysis.html">https://psl.noaa.gov/data/gridded/data.ncep.reanalysis.html</a>
ERA5	0.25° x 0.25°	6-hour	<a href="https://www.ecmwf.int/en/forecasts/dataset/ecmwf-reanalysis-v5">https://www.ecmwf.int/en/forecasts/dataset/ecmwf-reanalysis-v5</a>

Table 2. AF datasets used to drive the ocean model and reconstruct ocean temperature anomalies based on the adjoint sensitivities.

## 3.2 MITgcm

### *a. Model configuration*

In this study, the Estimating the Circulation and Climate of the Ocean (ECCO) technology (see online at <https://www.ecco-group.org/>), consisting of the Massachusetts Institute of Technology General Circulation Model (MITgcm) and its adjoint model is applied to study the sensitivity of anomalous high temperature to AF and ocean states. The MITgcm is an advanced finite volume model that simulates general ocean circulation and includes a model for sea-ice dynamics. The model setup employs the Bulk Formula Package to compute the heat and freshwater flux instead of utilizing heat and freshwater data to force the model. Details about the model are described by Marshall et al. (1997a; b) as well as Adcroft et al. (2004); more information can be found online at <https://mitgcm.readthedocs.io/>. The MITgcm was created to enable the automatic generation of tangent linear and adjoint code by using automatic differentiation of its source code through the Transformation of Algorithms in Fortran (TAF; Giering & Kaminski, 1998; Heimbach et al., 2005).

All model runs were performed over a quasi-global domain between 80°S and 80°N and with a realistic bottom topography based on the Earth Topography 5-arc-min grid (ETOPO5) dataset ([National Geophysical Data Center, 1993](#)). The ocean resolution in meridional and zonal directions is uniformly 2°. In the vertical, the resolution consists of 23 levels that are unevenly spaced, with depth ranging from the near-surface (5 m) down to several hundred meters in the deep ocean (the top six layers are located within the upper 100 m of the ocean). The model setup incorporates components for sea ice dynamics by employing Ice and Sea Ice Packages ([Heimbach et al., 2010](#); [Hibler, 1980](#); [Losch et al., 2010](#)). Vertical mixing is represented by the K-Profile Parameterization scheme (KPP; [Large et al., 1994](#)), and the Gent–McWilliams (GM) eddy parameterization scheme ([Gent & McWilliams, 1990](#)) was employed in the forward model. Due to stability reasons, it had to be excluded from the adjoint code of the mixed layer parameterization. The values of key model parameters are summarized in [Table 3](#).

Parameter	Symbol	Value
Vertical Laplacian viscosity	$\nu_v$	$10^{-3} \text{ m}^2\text{s}^{-1}$
Horizontal Laplacian viscosity	$\nu_h$	$5 \times 10^4 \text{ m}^2\text{s}^{-1}$
Vertical diffusivity	$\kappa_v$	$10^{-5} \text{ m}^2\text{s}^{-1}$
Horizontal diffusivity	$\kappa_h$	$10^2 \text{ m}^2\text{s}^{-1}$
Momentum time step	$\Delta t_{u,v}$	3600 s

Table 3. Model parameters.

Instead of forcing the model with heat and freshwater flux, an atmospheric boundary layer scheme is employed. This approach enables the calculation of flux terms using AF based on bulk formulas ([Bryan et al., 1996](#); [Hunke & Lipscomb, 2010](#)):

$$Q_S = \rho_a C_p C_s U_{10} (t_s - t_a), \quad (3.1a)$$

$$Q_L = \rho_a L_E C_L U_{10} (q_s - q_a), \quad (3.1b)$$

$$Q_{lw} = \epsilon \sigma t_s^4. \quad (3.1c)$$

$Q_S$  is sensible heat flux,  $Q_L$  is latent heat flux and  $Q_{lw}$  is up longwave radiation [ $W/m^2$ ],  $\rho_a$  is the density of air [ $kg/m^3$ ],  $U_{10}$  is 10 m wind speed [m/s],  $C_p$  is the specific heat capacity of air [J/kg/K],  $C_s$  and  $C_L$  are sensible/latent heat transfer coefficients,  $L_E$  is the latent heat of evaporation [J/kg],  $t_s$  is air temperature measured from space and  $t_a$  is air temperature measured from ships,  $q_s$  is specific humidity of air at the sea surface and  $q_a$  is 10 m specific humidity of the air.  $\sigma$  is the Stefan–Boltzmann constant, and  $\epsilon$  is the emissivity. Emissivity is a value ranging from zero to one that shows how much less radiation is emitted compared to a perfect blackbody.

Forward simulations were initiated from January-mean monthly climatological temperature and salinity fields available from Levitus and Boyer ([1994](#)). The initial phase of the simulations spanned a 60-year period from 1948 to 2007 forced by AF ([Table. 2](#)), establishing a baseline for subsequent simulation. The model supports restarts from specific points via the use of pickup files. Following the baseline period, the ocean model was forced by realistic

monthly mean AF including zonal (U) and meridional wind velocity (V), precipitation (PRE), air temperature (T2M), specific humidity (SH), and radiation terms (SW and LW) diagnosed from two reanalysis datasets (Fig. 3.1). During this phase, the model was restarted from 2008 and extended to 2022 by using the corresponding pickup file from 2008.

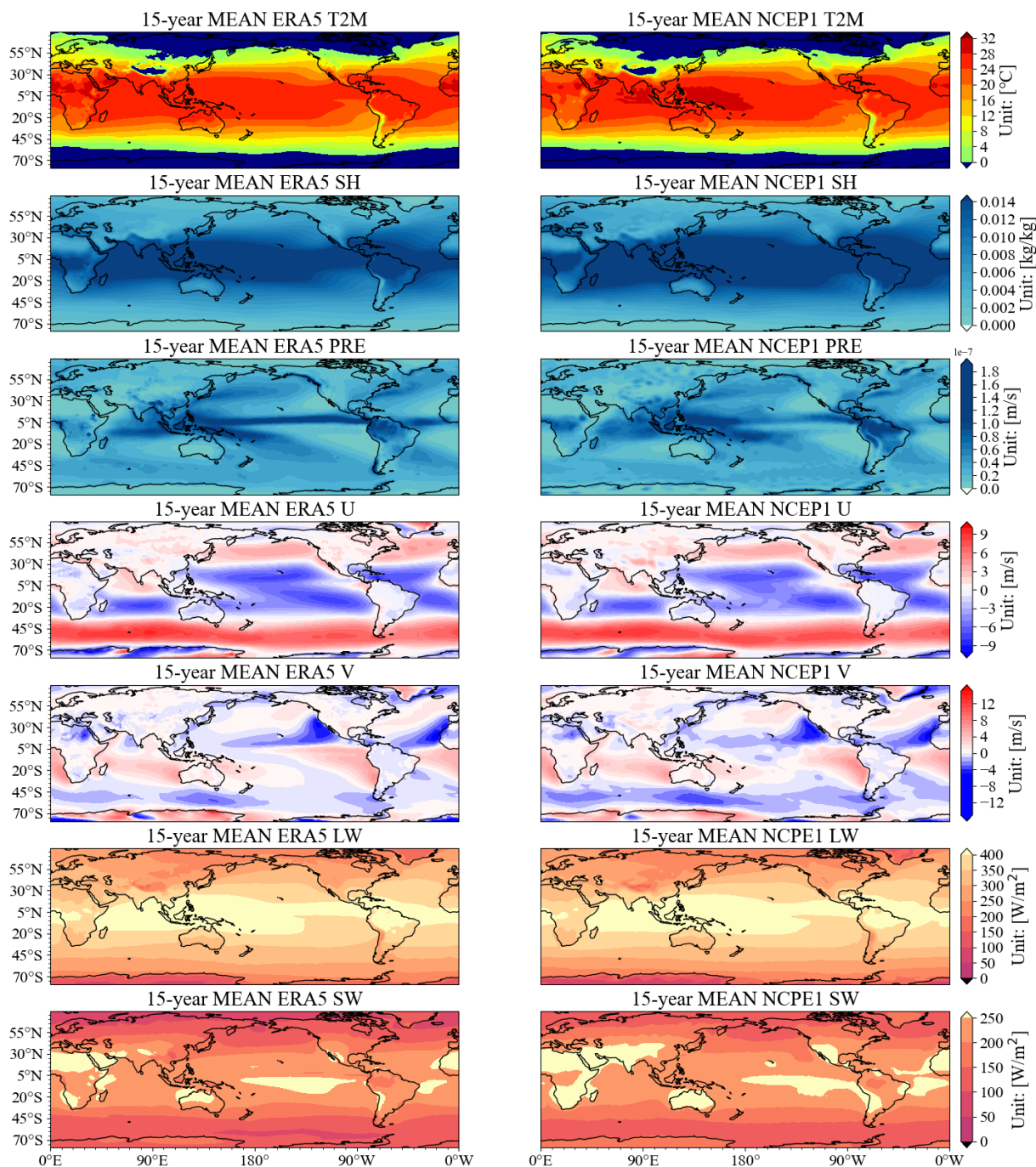


Fig. 3.1. The 15-year mean (from 2008 to 2022) external forcing fields (from top to bottom: T2M; SH; PRE; U; V; LW; SW) based on two datasets. Left: ERA5; right: NCEP-RA1.

*b. Model evaluation*

During a 15-year period, the mean SST state of the two datasets exhibits significant agreement, even though the datasets differ in spatial resolution (Fig. 3.2). The model shows overall strong performance, effectively capturing both the warmest center and the decreasing trend along latitude. However, in the equatorial western Pacific, the model exhibited overestimation, particularly in the simulations forced by NCEP-RA1. This may be related to the excessive T2M as shown in Fig. 3.1. The mean potential temperature changes with depth further supports this observation (Fig. 3.3). Potential temperature in the deeper ocean correlates well with ORAS5 reanalysis data; however, SST is overestimated, especially for scenario forced by NCEP-RA1. Fortunately, this equatorial region is not the primary focus of this study.

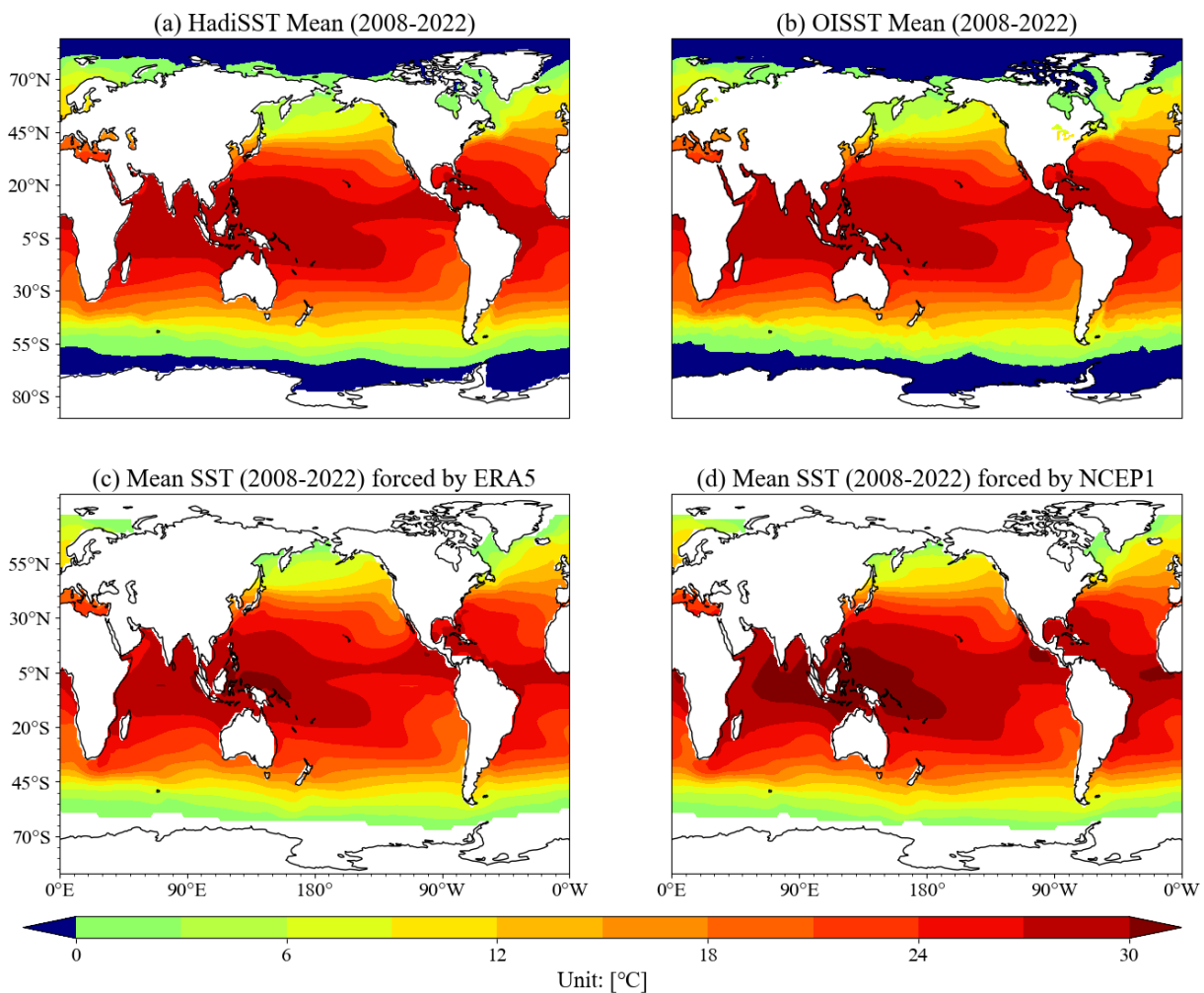


Fig. 3.2. The 15-year mean SST from 2008 to 2022 derived from various datasets. (a) HadiSST; (b) OISST; (c) ERA5 forced model outputs; (d) NCEP-RA1 forced model outputs.

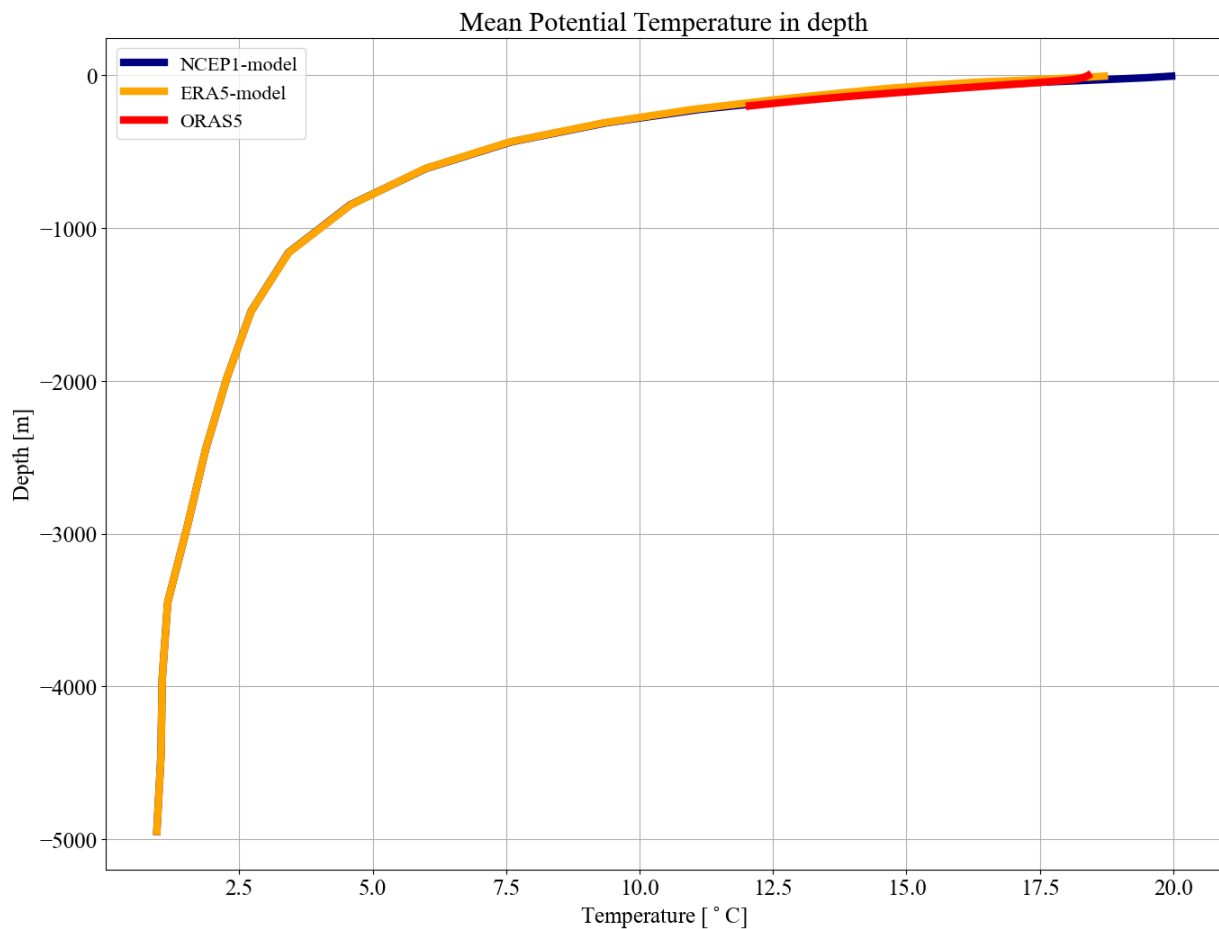


Fig. 3.3. The global mean potential temperature changes with depth based on three datasets (Red: ORAS5; Navy: NCEP-RA1 forced model; Orange: ERA5 forced model).

Taking 2022 and 2014 as examples, these two years are significant MHW years that this study focuses on, with the corresponding SSTa displayed in Figs. 3.4 & 3.5. The intensity of the SSTa in 2014 is relatively modest, and the results are consistent across various resolutions and forcing scenarios. In contrast, the intensity of SSTa in 2022 is notably higher, and low-resolution products demonstrate inadequate performance. Additionally, both forced models are limited in their capacity to simulate extreme events. In comparison, in the NWP region, models driven by ERA5 data outperform those driven by NCEP-RA1 data. While in the NEP region, the performance is reversed.

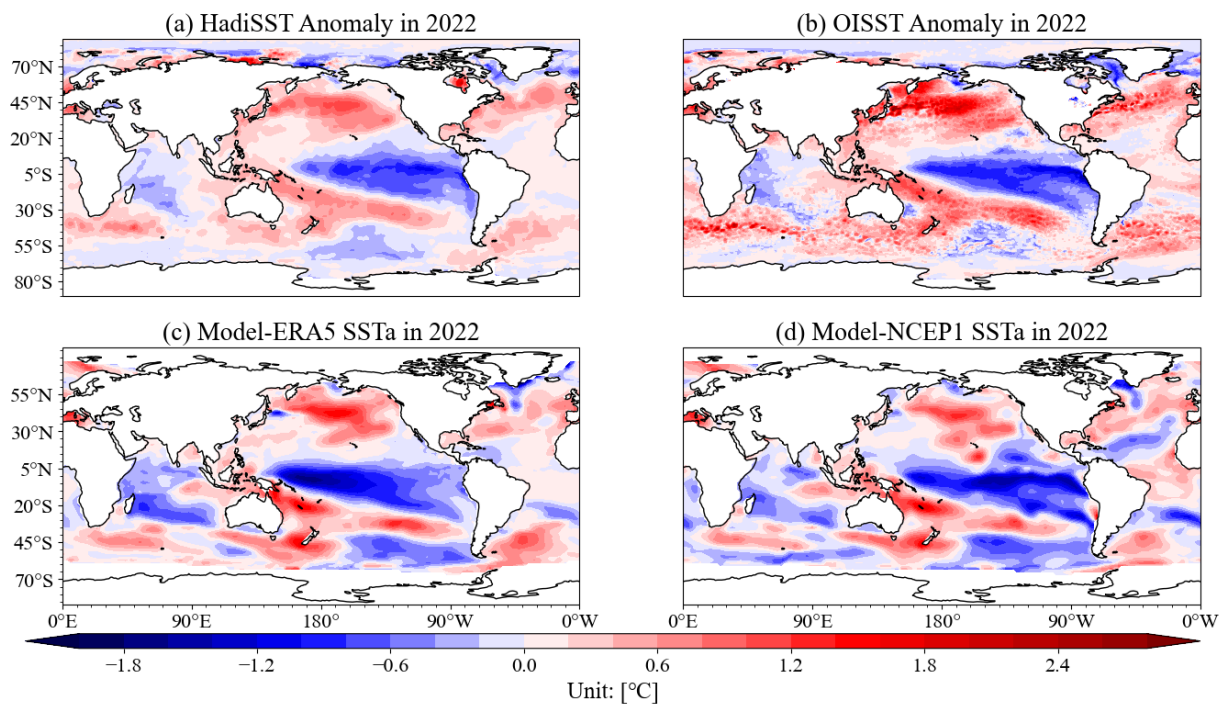


Fig. 3.4. Annual mean SSTa for 2022, calculated relative to the 15-year mean (2008-2022) and derived from various datasets. (a) HadiSST; (b) OISST; (c) ERA5 forced model outputs; (d) NCEP-RA1 forced model outputs.

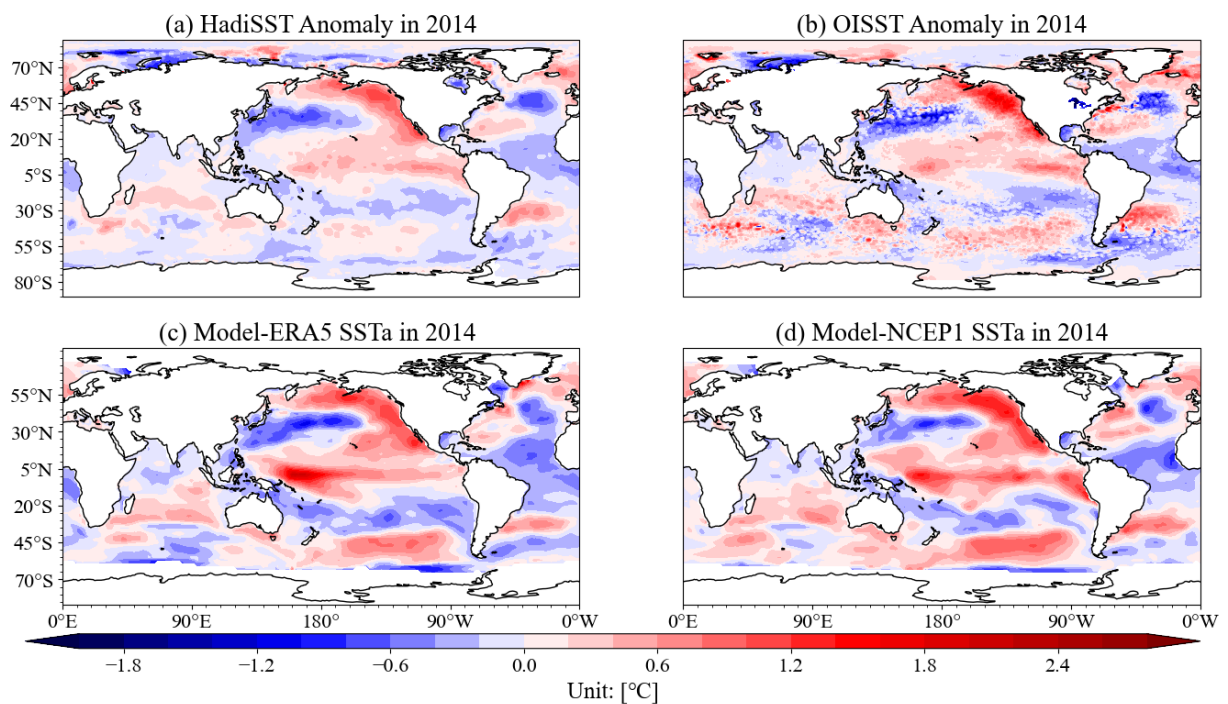


Fig. 3.5. As Fig. 3.4, but for 2014.

### 3.3 Adjoint Method

The Adjoint method is widely used in meteorology ([Demirdjian et al., 2020](#); [Doyle et al., 2014](#); [Reynolds et al., 2019](#); [Wilson et al., 2013](#)) and dynamical oceanography due to its direct and efficient estimation of sensitivity of model output with respect to input ([Errico, 1997](#); [Köhl et al., 2007](#); [Köhl & Stammer, 2004](#); [Stammer et al., 2018](#)). The core principle of the adjoint method is to calculate the gradient of the objective function. Compared to the mixed-layer heat budget analysis, adjoint sensitivity analysis has a clear advantage in that it can illustrate the pathways of sensitivity concerning the cost function. In contrast, the mixed-layer heat budget analysis is limited to the target region and primarily highlights the local factors driving potential temperature changes. Holbrook et al. ([2020](#)) suggested the use of the adjoint method to explain the fundamental dynamics underlying back-trajectory teleconnections.

Previous sensitivity studies have employed objective functions such as heat transport ([Marotzke et al., 1999](#)), freshwater flux ([Heimbach & Losch, 2012](#)), stream function ([Bugnion et al., 2006](#)), surface vorticity (the curl of horizontal velocity, e.g. [Zhan et al., 2018](#)), volume transport ([Czeschel et al., 2012](#); [Losch & Heimbach, 2007](#); [Mazloff, 2012](#); [Wang et al., 2022a](#); [Zhang et al., 2012](#)), heat content ([Jones et al., 2019](#)) and SSH or SST ([Frederikse et al., 2022](#); [Gopalakrishnan et al., 2013](#); [Köhl & Vlasenko, 2019](#); [Verdy et al., 2014](#); [Yang et al., 2023](#); [Zhang et al., 2011](#)) to quantify the importance of model inputs (e.g. bottom topography; initial conditions; boundary conditions; AF) and to estimate the ocean state ([Stammer et al., 2002](#); [Wang et al., 2022d](#)). It is also commonly used to quantify the contributions from local and remote forcing ([Boland et al., 2021](#); [Jones et al., 2018](#); [Veneziani et al., 2009](#); [Wang et al., 2022b](#)). In addition, an adjoint tracer can be used to identify the sources and the pathways of the water mass ([Fukumori et al., 2004](#)).

This approach is primarily utilized to conduct sensitivity analysis in this study. A schematic representation of the model-adjoint method for estimating sensitivities is presented in [Fig. 3.6](#) ([Hill et al., 2004](#)).

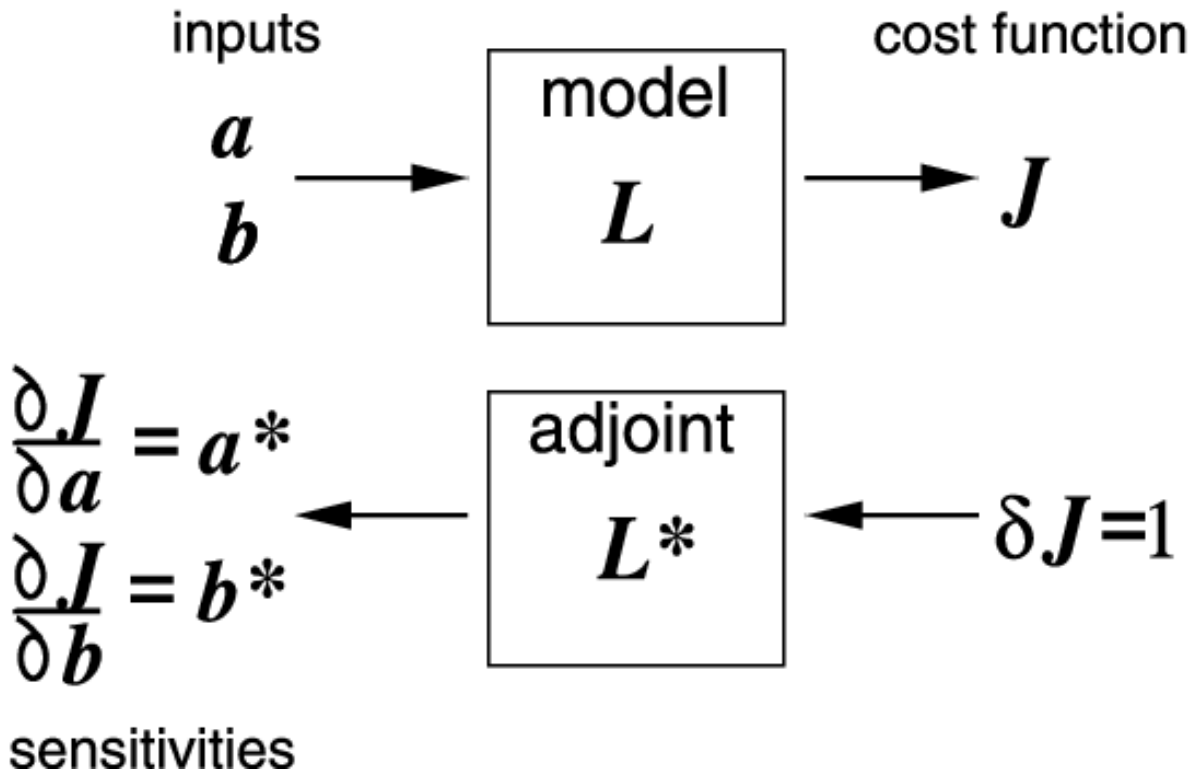


Fig. 3.6. A schematic representation of the model-adjoint method for estimating sensitivities. The image is taken from Hill et al. (2004). The cost function  $J$  is a function of the state of the forward model  $L$ , which is dependent on the input parameters  $a$  and  $b$ . The adjoint model  $L^*$  runs backward from changes in the cost function  $\delta J$  to numerically evaluate its sensitivities to the input parameters ( $\frac{\partial J}{\partial a}$  and  $\frac{\partial J}{\partial b}$ ).  $a^*$  and  $b^*$  represent the outputs of the adjoint model.

Consider a traditional nonlinear ocean model  $L$ , the model equations can be simplistically represented as (Wang et al., 2022a):

$$y = L(x_0), t \in [0, T] \quad (3.2)$$

where  $L$  represents the nonlinear forward operator applied to the state vector  $x$  at the initial time ( $t=0$ ). For a small perturbation  $\delta_{x_0}$  at the initial time, its evolution at the final time ( $t=T$ ) in a nonlinear system can be expressed as:

$$\delta_y = L(x_0 + \delta_{x_0}) - L(x_0) = L^* \delta_{x_0} \quad (3.3)$$

where  $L^*$  represents the linearized dynamical operator. Given a function  $f(x)$  that is infinitely differentiable at a point  $s$ , the Taylor series is defined as:

$$f(x) = f(s) + (x - s) \frac{f'(s)}{1!} + (x - s)^2 \frac{f''(s)}{2!} + (x - s)^3 \frac{f'''(s)}{3!} + \dots, \quad (3.4)$$

Then [Eq. 3.3](#) can be treated as a first-order Taylor series expansion, which acts as a linear approximation of the system. The coefficients of this linear model  $L^*$  are derived from the slopes of the tangents to the trajectories of the state variables within the forward model  $L$ . Consequently, this approach is often referred to as a tangent linear model.

The cost function  $J$  is computed as a function of the state of the forward model  $L$ , which is contingent upon not only the initial state vector  $x_0$  but also the input parameters  $a$  and  $b$ . These parameters may represent bottom topography, initial conditions, boundary conditions, and AF. The adjoint method operates in a reverse manner on a perturbation of the cost function, enabling the numerical evaluation of the sensitivities of the cost function (also known as the objective function) with respect to the input parameters. Then the adjoint model yields the sensitivities, for example:

$$a^*(\mathbf{r}, t) = \frac{\partial J}{\partial a}(\mathbf{r}, t) \quad (3.5)$$

at each point ( $\mathbf{r}$  is the position vector) in the model at time  $t$ . The dynamics of the model are expressed through the chain rule of partial derivatives.

In this study, the aim is to investigate the sensitivity of anomalous temperature variation to different AF, including U, V, PRE, T2M, SH, and radiation terms (SW, LW). The cost function is defined as the volume-mean potential temperature in the selected depth (e.g. upper 100 m) of selected study regions in terms of different years, averaged over a certain period (e.g. one-year period as annual mean SSST):

$$J = \frac{1}{V\Delta t} \int_V \int_{\Delta t} \theta(\mathbf{r}, t) dt d\mathbf{r} \quad (3.6)$$

where  $V$  is the control volume (e.g. the upper 100 m of the study region),  $t$  is the time and  $\Delta t$  is the integration period,  $\theta$  is the potential temperature,  $\mathbf{r}$  is the position vector. The sensitivity fields are three-dimensional for AF, as they vary with time, longitude, and latitude. For the clarity of the results, only sensitivities higher than a certain threshold are considered to avoid noise ([Veneziani et al., 2009](#)).

In the following sensitivity analysis, various time periods are used. For clarification, the target year will be denoted as ‘Year 0’ or ‘0yr’, and one year before the target year will be denoted as ‘Year -1’ or ‘-1yr’. The last month of Year 0 will be denoted as 0mon, while the last month of -1yr will be denoted as -12mon (or lead 12month).

### 3.4 Contribution Analysis

The sensitivity fields associated with different AF exhibit varying units due to the disparate nature of the forcing involved. Therefore, the contribution analysis is applied to scale the contribution of different AF to the total variation of SSSTa. The linear change in  $J$  expected from an actual AF anomaly (e.g. [Fig. 3.7](#)), also known as the contribution (the scaled sensitivity), is calculated ([Jones et al., 2019](#); [Verdy et al., 2014](#); [Wang et al., 2022b](#)):

$$\Delta J_i(x, y, \Delta t) = \frac{\partial J}{\partial F_i(x, y, \Delta t)} \Delta F_i(x, y, \Delta t) \quad (3.7)$$

where  $\frac{\partial J}{\partial F_i(x, y, \Delta t)}$  is the adjoint sensitivity of SSST with respect to different AF ( $F_i$ ) at lead time  $\Delta t$  ( $\Delta t = -1\text{mon}, -2\text{mon}, \dots, -48\text{mon}, \dots, -3\text{yr}, -4\text{yr}, \dots$ ) and location  $(x, y)$  represents a point on the grid;  $\Delta F_i(x, y, \Delta t)$  is the corresponding monthly anomaly of forcing  $F_i$  at lead time  $\Delta t$  and location  $(x, y)$  which is calculated relative to the 60-year (1948-2008) mean state including a seasonal cycle. The sign of the contribution  $\Delta J$  is determined by multiplying the sign of the sensitivity field with the sign of the AF anomalies. Both positive and negative anomalies can produce a positive contribution, depending on the characteristics of the sensitivity fields. Therefore, the contribution pattern can still highlight the regions of the largest sensitivity with respect to the cost function, as no contributions are expected when the sensitivity is zero. However, the scaled sensitivity fields may not capture the detailed sensitivities, as low AF anomalies may result in reduced contribution fields, even when sensitivity is high.

Building on [Eq. 3.7](#), the cumulative temporal contribution for one forcing in a spatial map can be then expressed as:

$$\Delta J_i(x, y) = \sum_{\Delta t} \frac{\partial J}{\partial F_i(x, y, \Delta t)} \Delta F_i(x, y, \Delta t) \quad (3.8)$$

The cumulative spatial contribution at each time step for one forcing in a temporal map can be expressed as:

$$\Delta J_i(\Delta t) = \sum_{x, y} \frac{\partial J}{\partial F_i(x, y, \Delta t)} \Delta F_i(x, y, \Delta t) \quad (3.9)$$

The total temporal contribution of all grids for all AF can be expressed as:

$$\Delta J(x, y) = \sum_i \sum_{\Delta t} \frac{\partial J}{\partial F_i(x, y, \Delta t)} \Delta F_i(x, y, \Delta t) \quad (3.10)$$

The total contribution of all grids at all timesteps for each AF can be expressed as:

$$\Delta J(i) = \sum_{x,y} \sum_{\Delta t} \frac{\partial J}{\partial F_i(x,y,\Delta t)} \Delta F_i(x,y,\Delta t) \quad (3.11)$$

At this stage, the contributions from different AF can be compared. Then the total contribution by aggregating the cumulative contribution of all AF at all timesteps and all grids can be compared to the cost function except for some non-linear processes:

$$J \approx \sum_i \sum_{x,y} \sum_{\Delta t} \Delta J_i(x,y,\Delta t) \quad (3.12)$$

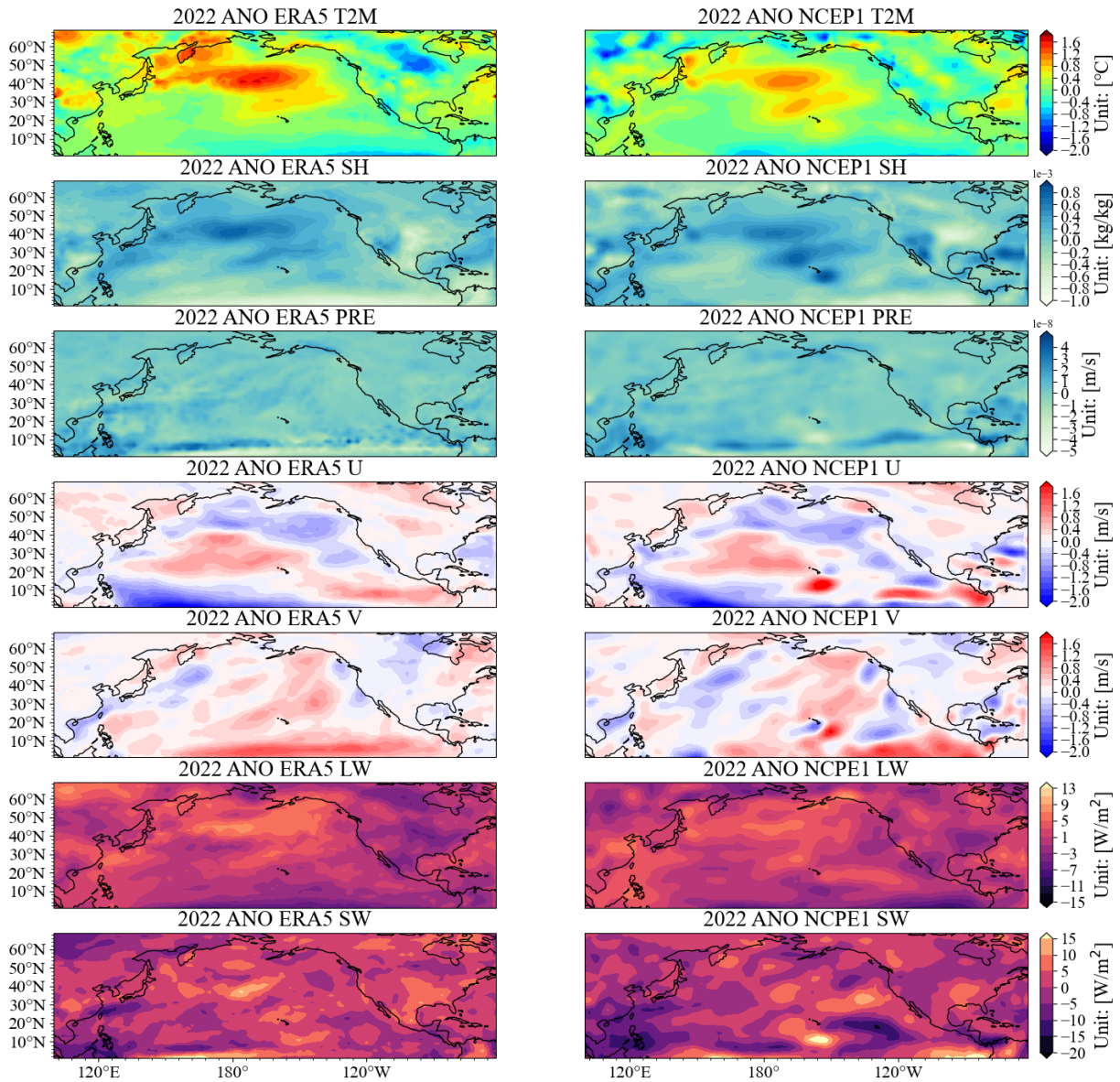


Fig. 3.7. The 2022 annual anomalies of AF in the NP, calculated relative to the 15-year mean from 2008-2022 (from top to bottom: T2M; SH; PRE; U; V; LW; SW) based on two datasets. Left: ERA5; right: NCEP-RA1.

### 3.5 Perturbation Experiments

The sensitivities derived from the adjoint model provide a linear approximation of nonlinear equations, which works best for small changes and short time periods. To ensure this linear assumption is valid, nonlinear forward perturbation experiments are conducted. In these experiments, results from simulations with slight changes are compared to those from a control simulation, helping to identify the physical processes affected by those perturbations. Adjoint sensitivities detect the locations and timing in the model's input AF leading to specific responses in the system. In contrast, a forward perturbation experiment reveals the areas and timing of the system's response to a defined perturbation, a process also referred to as response analysis.

Perturbations were computed based on the standard deviation of the AF, following the methodologies (Eq. 3.13) outlined by Yang et al. (2023) and Wang et al. (2022a). These perturbations were then incorporated into the corresponding original forcing fields. The model was subsequently integrated forward in time, and the results were analyzed as anomalies in relation to the control run.

$$\Delta F_i(x, y, \Delta t) = \frac{\partial J / \partial F_i |_{(x, y, \Delta t)}}{\max(|\partial J / \partial F_i|)} \cdot \delta F_{i\_std} \quad (3.13)$$

where  $i$  represents different AF,  $x$  and  $y$  represent the longitude and the latitude of the model grid, respectively;  $\Delta t$  represents the corresponding month.  $F_{i\_std}$  is the standard deviation of annual mean AF (Fig. 3.8). To bound the upper magnitude of the perturbation, the adjoint sensitivities to different AF were first normalized by their maximum absolute values  $\frac{\partial J / \partial F_i |_{(x, y, \Delta t)}}{\max(|\partial J / \partial F_i|)}$  and then set it to be proportional to the standard deviation of each field multiplied by a factor of  $\delta$ . The choice of  $\delta$  is a scaling factor that was set to 1.5 for all perturbation experiments to yield a sufficiently large but not too large response such that neither the assumptions of the underlying tangent linearized equation is violated (Yang et al., 2023) nor the noise generated by nonlinear parameterizations such as KPP and GM dominate the signal. The perturbations added to the forward model represent an alternative form of scaled sensitivity compared to contribution analysis (Eq. 3.7), achieved by multiplying the standard deviation rather than utilizing the actual forcing anomalies. However, the perturbations added

to different AF cannot be directly compared with one another; instead, they can be compared to the original forcing.

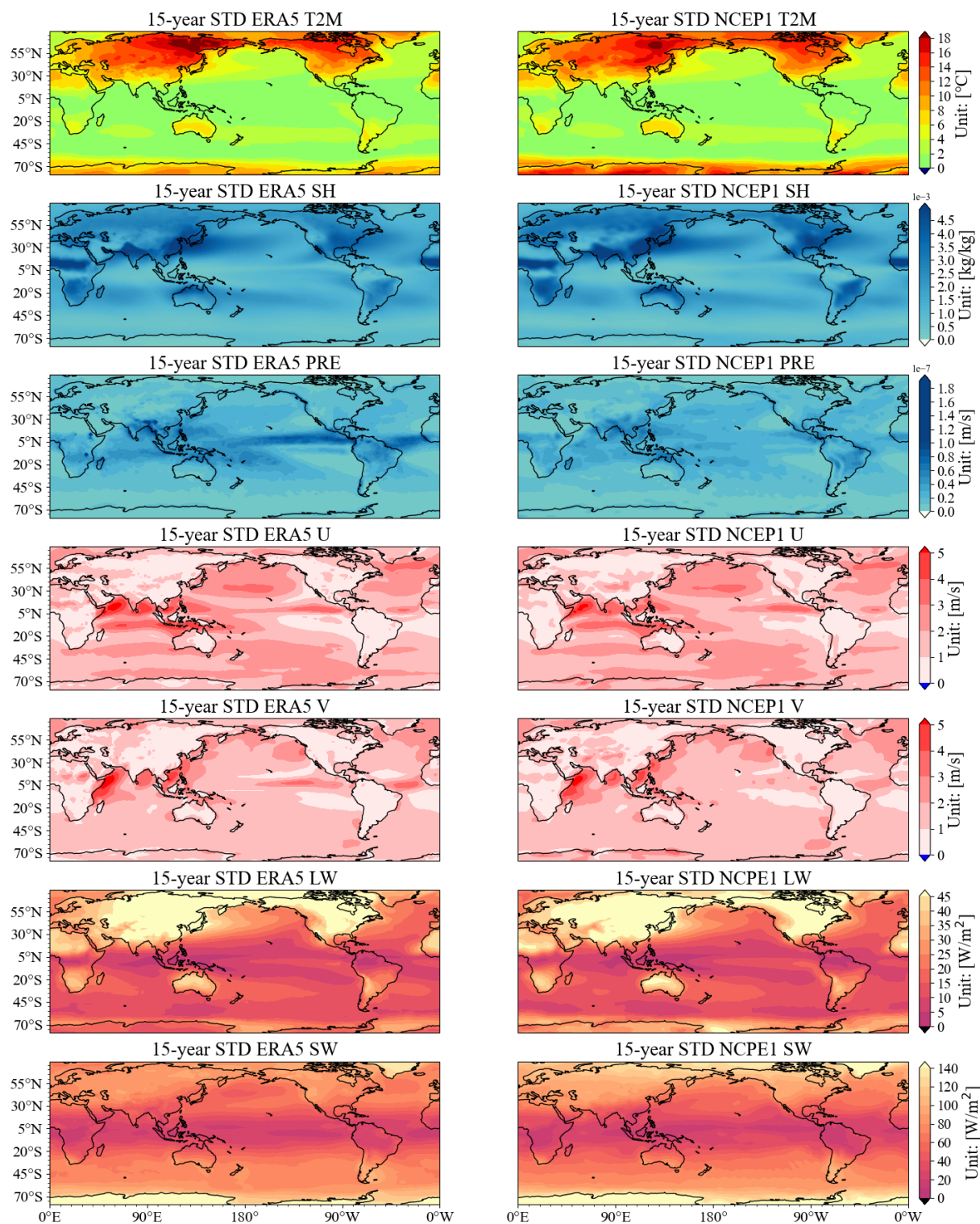


Fig. 3.8. The standard deviation of AF between 2008 and 2022 (from top to bottom: T2M; SH; PRE; U; V; LW; SW) based on two datasets. Left: ERA5; right: NCEP-RA1.

### 3.6 Adjoint Validation

Perturbation experiments utilizing identical positive and negative perturbations can be employed to evaluate the validity of the adjoint linearity assumption ([Jones et al., 2018](#); [Verdy et al., 2014](#); [Zhan et al., 2018](#)). When applying a perturbation  $\Delta J$ , the response of the cost function can be approximated by Taylor series expansion ([Eq. 3.4](#)) as:

$$\Delta J = J - J_0 = \frac{\partial J}{\partial F}(F - F_0) + \frac{1}{2} \frac{\partial^2 J}{\partial F^2}(F - F_0)^2 + \dots, \quad (3.14)$$

where  $J_0$  and  $F_0$  represents reference values from the control run. If a sensitivity-like perturbation is introduced, the response can be denoted as  $\Delta J_+$ . Conversely, if a reverse-sensitivity-like perturbation is introduced, the response can be denoted as  $\Delta J_-$ . The linear response or the first derivative then can be estimated by:

$$\Delta_1 = \frac{1}{2}(\Delta J_+ - \Delta J_-) \approx \frac{\partial J}{\partial F}(F - F_0) \quad (3.15)$$

and the non-linear response or the second derivative can be estimated by:

$$\Delta_2 = \frac{1}{2}(\Delta J_+ + \Delta J_-) \approx \frac{1}{2} \frac{\partial^2 J}{\partial F^2}(F - F_0)^2 \quad (3.16)$$

Only when  $\Delta_1 \gg \Delta_2$ ,  $\Delta_1$  can be an adequate approximation of the linear response. If the two responses are comparable in magnitude, a more detailed examination of the higher-order terms should be considered. The linearity assumption of the MITgcm for bottom topography sensitivity analysis has been validated, with inaccuracies remaining within 30% over a 100-year timescale and within 5% on an annual scale ([Losch & Heimbach, 2007](#)).

[Fig. 3.9](#) and [Fig. 3.10](#) present an example of a perturbation experiment designed for model validation purposes. In this test experiment, a specific grid point situated at 53°N, 164°E is focused on for convenience. The standard deviation of the SW at this grid point is approximately 80  $W/m^2$  ([Fig. 3.8](#)). To investigate the effects of perturbations, a relatively modest but sufficient perturbation magnitude is selected. The SW is perturbed uniformly by +10  $W/m^2$  (the top panel in [Fig. 3.9](#)) and -10  $W/m^2$  (the bottom panel in [Fig. 3.9](#)) for a duration of 1 month within a 2° x 2° grid box centered at 53°N, 164°E. After the application of the perturbations, the forward model is executed for the period spanning from 2008 to 2009. The annual mean SST in 2009, relative to the 15-year mean at this target point, is selected as the objective function for the comparison.

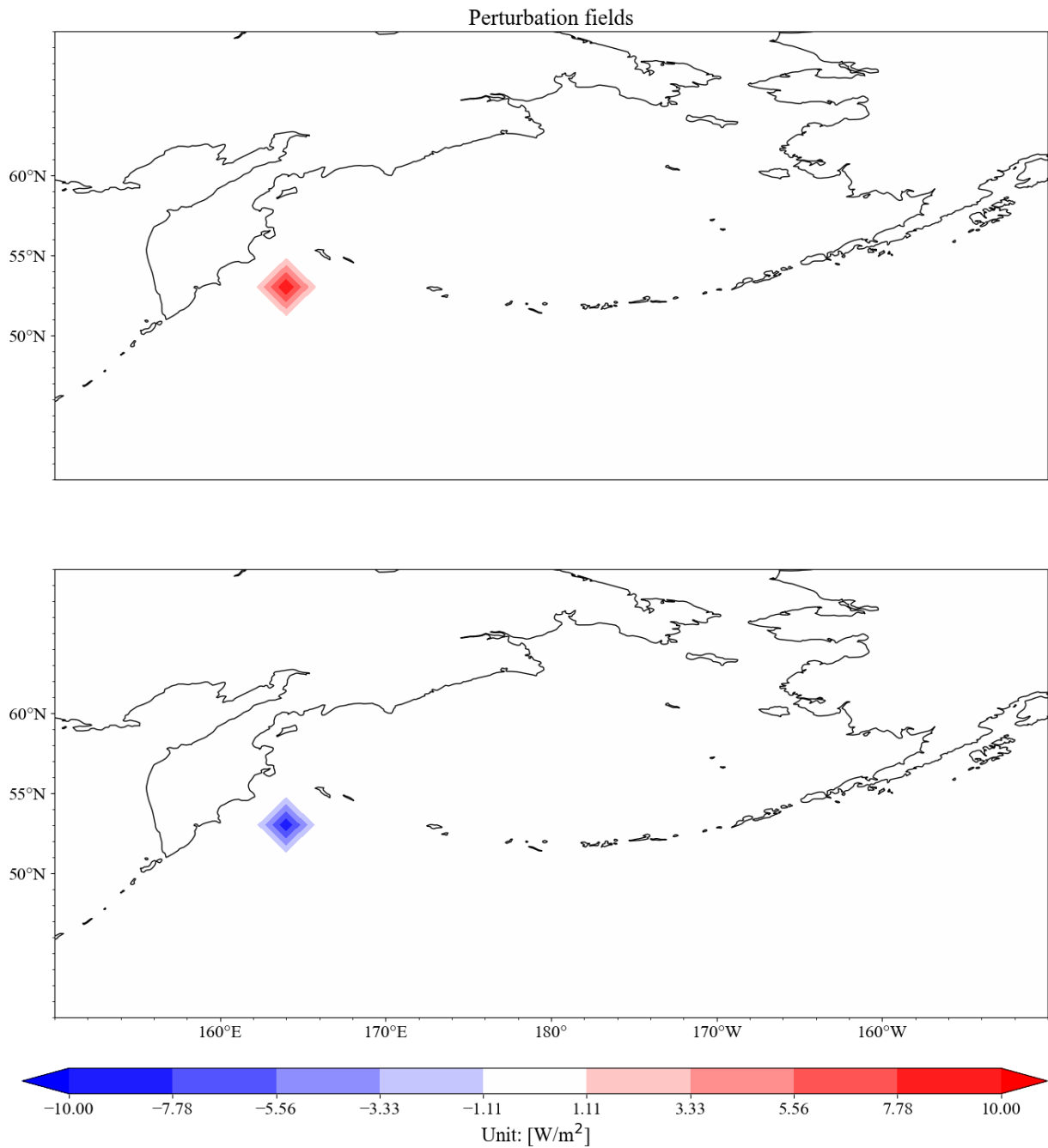


Fig. 3.9. The positive (top,  $+10 W/m^2$ ) and negative (bottom,  $-10 W/m^2$ ) SW perturbation added to the forward control run for model validation.

The only difference between the perturbed run and the control run lies in the application of a SW perturbation for one month at the selected grid point. The sensitivity, defined as the partial derivative of SST with respect to SW, can be approximated by the ratio of the change in the annual mean SST at this point for the year 2009 to the magnitude of the SW perturbation applied. For example, it is evident that applying perturbations in January or February of 2008 does not result in changes to the objective function (crosses before -15mon in [Fig. 3.10](#)). This observation indicates that the SST at the selected grid point is not sensitive to the SW variations occurring in the early months of 2008; rather it is primarily sensitive to the conditions within the target year or several months before the target year.

For comparison, an adjoint run is conducted with the annual mean SST of 2009 designed as the cost function. The sensitivity solutions obtained from the adjoint run closely align with those derived from the forward perturbation-based approach. Moreover, the adjoint run facilitates the identification of the most sensitive period by executing the adjoint model only once, which would otherwise require multiple runs of perturbation experiments. This comparison is demonstrated within a simplified scenario focusing on a single grid point. To generate a broader spatial sensitivity map, it is necessary to repeat the perturbation experiment for each grid box within the model domain. Clearly, this forward perturbation-based sensitivity experimentation is computationally intensive and expensive.

To evaluate the linearity assumption, a negative perturbation was applied to the forward forcing field (the bottom panel in [Fig. 3.9](#)). The resulting response is depicted in [Fig. 3.10](#) (the navy line), illustrating a reverse effect in comparison to the positive perturbation (crosses). Subsequently, both the linear and nonlinear responses are calculated ([Eq. 3.15](#) & [Eq. 3.16](#)), as shown in the figure (the red and orange lines). As anticipated, the SST response to the imposed SW is nearly linear throughout the experimental period (the red line). The nonlinear response is minimal (the orange line), with only a very small fraction of non-linearity observed in January 2009 (Lead Month -11).

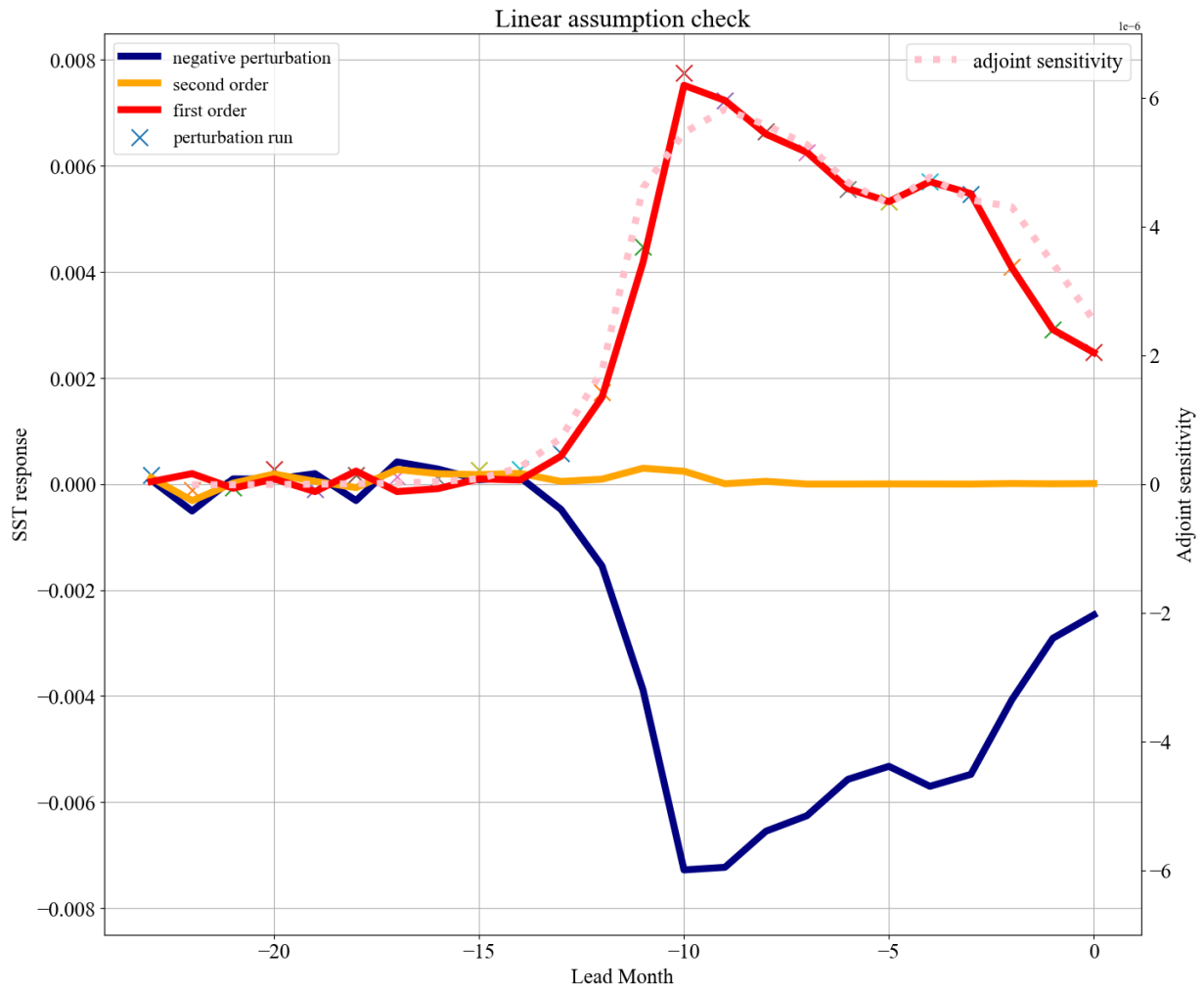


Fig. 3.10. Comparison of adjoint sensitivity (pink dots; unit:  $^{\circ}\text{C}/\text{W}/\text{m}^2$ ) and SST response ( $^{\circ}\text{C}$ ) calculated from forward perturbation experiments (solid lines and crosses; unit:  $^{\circ}\text{C}$ ) at  $53^{\circ}\text{N}$ ,  $164^{\circ}\text{E}$  with respect to monthly SW. Crosses show the response of positive perturbation and the navy line shows the response of negative perturbation. The red line shows a linear response and the orange line shows a non-linear response.

## 4 Results

### 4.1 Northeast Pacific Marine Heatwaves Mechanism

This section is designed to answer the first research question:

*What is the main atmospheric driver for the NEP MHWs?*

*Are the results comparable to those obtained through heat budget analysis or other methods?*

This section has been accepted for publication as:

*Xiaoxue Wang, Armin Köhl, Detlef Stammer. Northeast Pacific Marine Heatwaves Mechanism Inferred from Adjoint Sensitivities. Journal of Climate. (accepted and in production)*

The format and contents have been slightly adjusted to suit this thesis.

All relevant references and additional information are compiled at the end of this thesis.

### 4.1.1. NEP MHW Research Region

By now a classic example of an MHW is the 2014 – 2016 warm event that spread across the NEP Ocean—a warm event that researchers coined “the blob” of warm water ([Bond et al., 2015](#); [Chen et al., 2023](#), [Fig. 1](#)). Such anomalously warm surface water frequently returns to the NEP region, e.g. during July and August 2019 as shown in [Figs. 4.1.1a, b](#). Although extreme events may occur in various locations during certain months, a yearly analysis shows that similar locations in the NEP were consistently influenced by MHW during the years 2014 and 2019 ([Figs. 4.1.1c, d](#)). This consistent pattern highlights the persistent impact of MHWs in specific regions over time. Therefore, two specific regions within this area (region 1: 145° ~ 160°W, 48° ~ 56°N; region 2: 130° ~ 145°W, 40° ~ 48°N, white boxes) have been selected as the main research focus in the NEP to understand the mechanisms leading to long-lasting extreme temperatures there.

Shown in the lower two panels of [Fig. 4.1.1](#) are time series of annual mean HadiSST ([Rayner et al., 2003](#)) temperature anomalies for regions 1 and 2, respectively. Using the statistics between 1948 and 2022, MHW years detected are 1997, 2005, 2014-16, 2019-20 for region 1 and 1958, 1991-92, 2014-16, and 2019-20 for region 2. MHWs were identified in the figure using the 90th percentile of annual mean SST as a threshold. In accordance with previous findings, the last decade has witnessed a concurrent escalation in both the intensity and the frequency of MHWs within the designated study region. The warming trend is not removed, as the detected AF inherently includes this warming trend. The effect of global warming on AF is not considered separately.

Also shown in the figure are time series of the PDO index based on NOAA's extended reconstruction of SSTs (ERSST, Version 5, [Huang et al., 2017](#)), and of the NPGO index based on AVISO satellite products ([Di Lorenzo et al., 2008](#)). In both regions, curves are highly correlated with SST variations in that all identified MHW events occur during high/low PDO/NPGO conditions. While the correlation with the PDO is not surprising as it is related to a warming of the NEP region and defined by the leading pattern of SSTa, it is especially the agreement with NPGO that to some degree suggests an impact of changes in the ocean circulation on MHW in this region. The low-frequency behavior of these climate modes implies their importance for SST anomalies reaching across a threshold value ([Ren et al.,](#)

[2023](#)). The detailed cause for SST spikes to occur in the study regions remains unclear; however, they may primarily result from stochastic forcing ([Capotondi et al., 2022](#)).

Several studies have investigated the driving mechanism behind monthly or daily MHWs by using either heat budget analysis or composite and statistical analysis ([Kajtar et al., 2022](#); [Li et al., 2020](#); [Oliver, 2019](#); [Zschenderlein et al., 2019](#)). Of those, many show that the extreme temperature anomalies are highly related to atmospheric circulation variations such as atmospheric blocking events or North Atlantic Oscillation (NAO; [Pfahl & Wernli, 2012](#); [Scannell et al., 2016](#); [Schaller et al., 2018](#); [Yoon et al., 2020](#)). According to Amaya et al. ([2020](#)), the 2019 MHW event shown in [Fig. 4.1.1a](#) was caused by an unusual and persistent weather pattern resulting from a prolonged weakening of the NPSH. Bond et al. ([2015](#)) reported that the 2014 MHW was caused by reduced heat loss from the ocean to the atmosphere and weaker-than-normal cold advection in the upper layer of the ocean, both attributed again to an unusually strong and persistent weather pattern featuring higher-than-normal sea level pressure and involving heat and momentum flux anomalies. Few studies investigate NEP MHWs over extended time scales, particularly regarding the anomalously warm SST observed in 2014, which persisted for more than 2 years ([Schmeisser et al., 2019](#)).

[Fig. 4.1.1](#) demonstrates that similar locations in the NEP are consistently affected by MHW across different years on an annual scale. Accordingly, MHWs also influence annual mean temperatures suggesting that the definition of MHWs provided above can also be applied to annually averaged temperatures. They appear not only at the surface but also extend to the upper 100 m of the ocean. In this section, the aim is to investigate the mechanisms that drive these persistent annual MHWs marked in [Fig. 4.1.1](#) and compare them with the existing results from other methods.

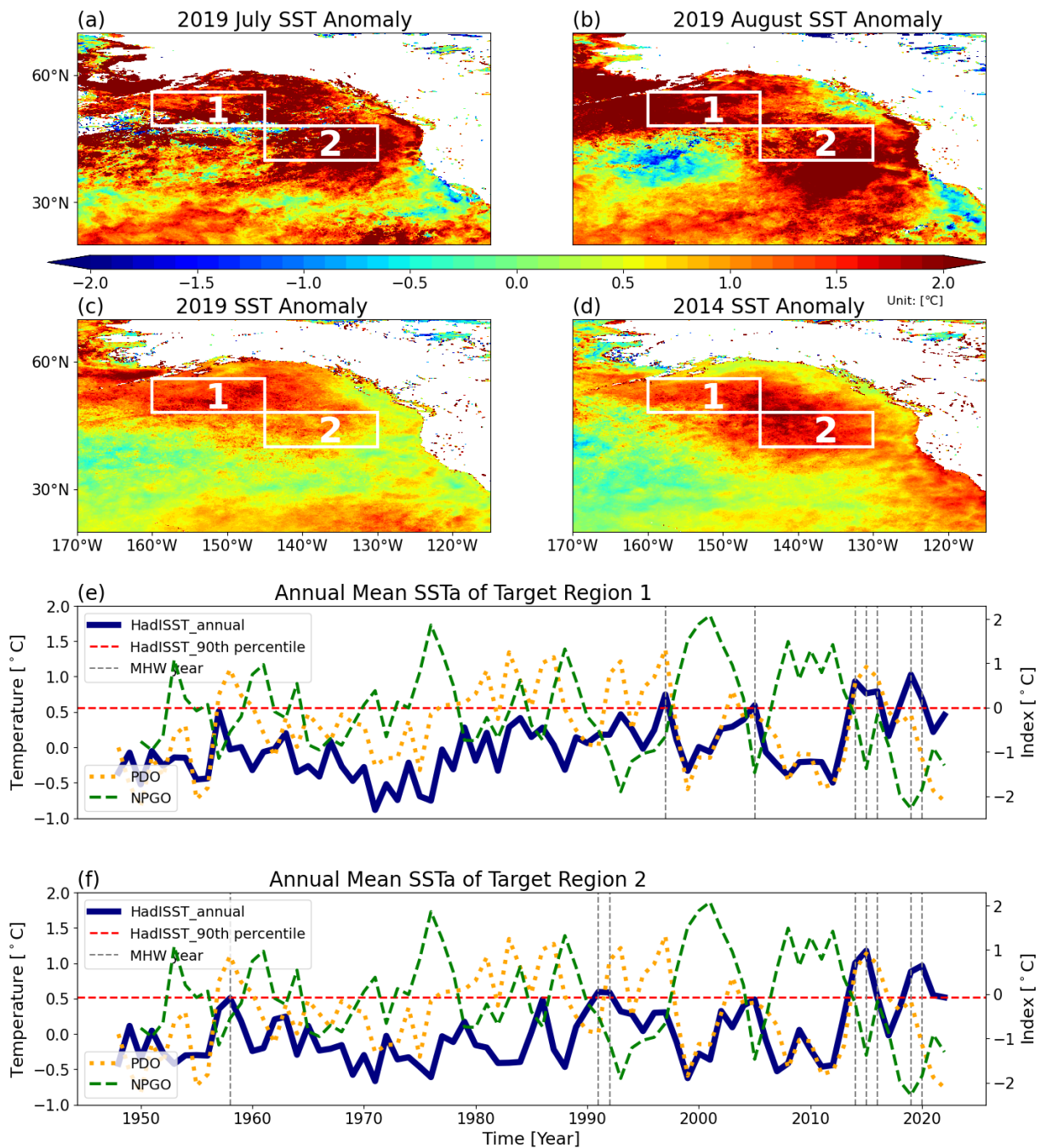


Fig. 4.1.1. MODIS SSTa of 2019 (a) July, (b) August relative to a climatological seasonal SST cycle from the period 2002-2021 and annual anomaly of 2019 (c) and 2014 (d) relative to the 20-year mean. White boxes show two study areas (region 1: 145° ~ 160°W, 48° ~ 56°N; region 2: 130° ~ 145°W, 40° ~ 48°N). (e) and (f) Time series of HadISST annual anomalies (Rayner et al., 2003) from 1948 to 2022 averaged over regions 1 and 2, respectively (blue lines). Superimposed are the PDO (orange dots) and NPGO (green dashed line) time series. Red dashed lines show the 90th percentile MHW index; vertical grey lines mark seven MHW events. Correlations between SST and PDO are 0.53 and 0.31 for regions 1 and 2, and SST and NPGO are correlated at 0.52 and -0.64 levels, respectively.

### 4.1.2. NEP MHW Model Set-up

Before conducting the adjoint experiment, the model's performance in the selected regions of the NEP is further validated. [Fig. 4.1.2](#) depicts the simulated temporal evolution of area mean potential temperature within the two target regions from 1948 to 2017 to provide a climatology baseline for comparison. Despite an apparent 0.25 °C temperature bias, the model effectively captures the amplitude of observed interannual variability and demonstrates a robust alignment with the trend of mean temperature evolution. The 70-year model time series displays a remarkable agreement with observations which demonstrates the model's ability to reproduce the observed MHW events. The correlation coefficients of two time series between the model and reanalysis are around 0.95 and two-tailed p-values are far less than 0.05 (the degrees of freedom number is 68), i.e., a statistically significant correlation exists between the model and observations.

Employing the annual MHW index definition, both the model and observations identify the same MHW years during the 70 years (1948-2017), specifically 1957, 1984, 1993, 1997, 2004-05 and 2014-16 for study region 1 and 1958, 1986, 1991-92, 2005 and 2014-16 for study region 2. Notably, the results are slightly different from [Fig. 4.1.1](#) because the model time period is different, and therefore the heatwave index (90th percentile of data) also differs.

After validation, a set of adjoint sensitivity experiments to examine the sensitivity of anomalous warming of NEP to AF anomalies was performed. The cost function is defined as the temperature field in the upper 100 m, of region 1 and region 2, respectively, averaged over a one-year period ([Eq. 3.6](#)).

Restarting from the specific years of the forward run illustrated in [Fig. 4.1.2](#), respective sensitivity runs were performed for all warm years and several normal years during 1988-2017. In each case, four-year-long forward and backward runs were conducted. Two primary adjoint experiments are targeting the year 2014 as the MHW year for region 1 (EXP1) and region 2 (EXP2). To examine how the evolution of sensitivity depends on the oceanic background state, several supplementary experiments are carried out based on the MHW index of each target region (vertical lines shown in [Fig. 4.1.2](#); e.g. setting the normal year 2007/2013 as the target year; setting MHW year 1997/2005/2015 as the target year). The adjoint model was run backward to calculate the adjoint sensitivities of the annual mean and volume-mean potential temperature to a set of independent parameters, including ocean temperature and salinity as

well as wind velocity, PRE, T2M, SH, and radiation. The analysis reveals that the sensitivity before -4yr is notably weak.

Upon analyzing the adjoint sensitivity outcomes, it was observed that the results of all experiments exhibited substantial similarity. Sensitive areas do not change much with the different target years. Results set the normal year 2007 as the target year (Fig. 4.1.3) which shows a similar pattern with setting MHW year 2014 (Fig. 4.1.4). The slight differences in the distribution patterns are due to the different maximum values of the normalization. Additionally, the sensitivity with respect to T2M and SH in 2007 exhibits a similar distribution. Consequently, only the sensitivity fields derived from the adjoint experiment targeting the MHW year 2014 are presented for the following analysis.

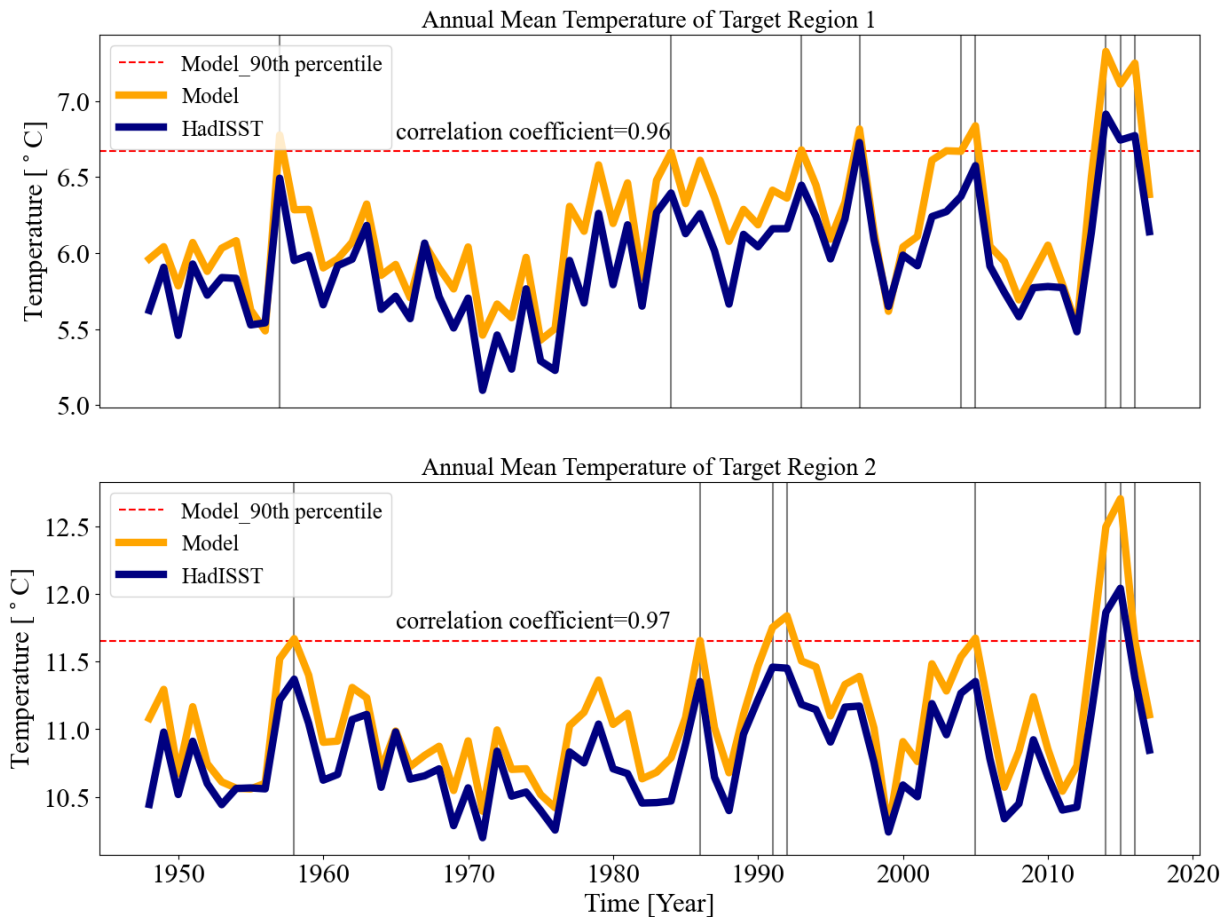


Fig. 4.1.2. Time series of mean potential temperature in (top) regions 1 and (bottom) region 2 from 1948 to 2017. The orange and blue lines represent the annual mean model and HadISST fields, respectively. Red dashed lines show the MHW index for the forward model; the grey vertical line shows the resulting MHW events.

Adjoint Sensitivity of T2M/SH

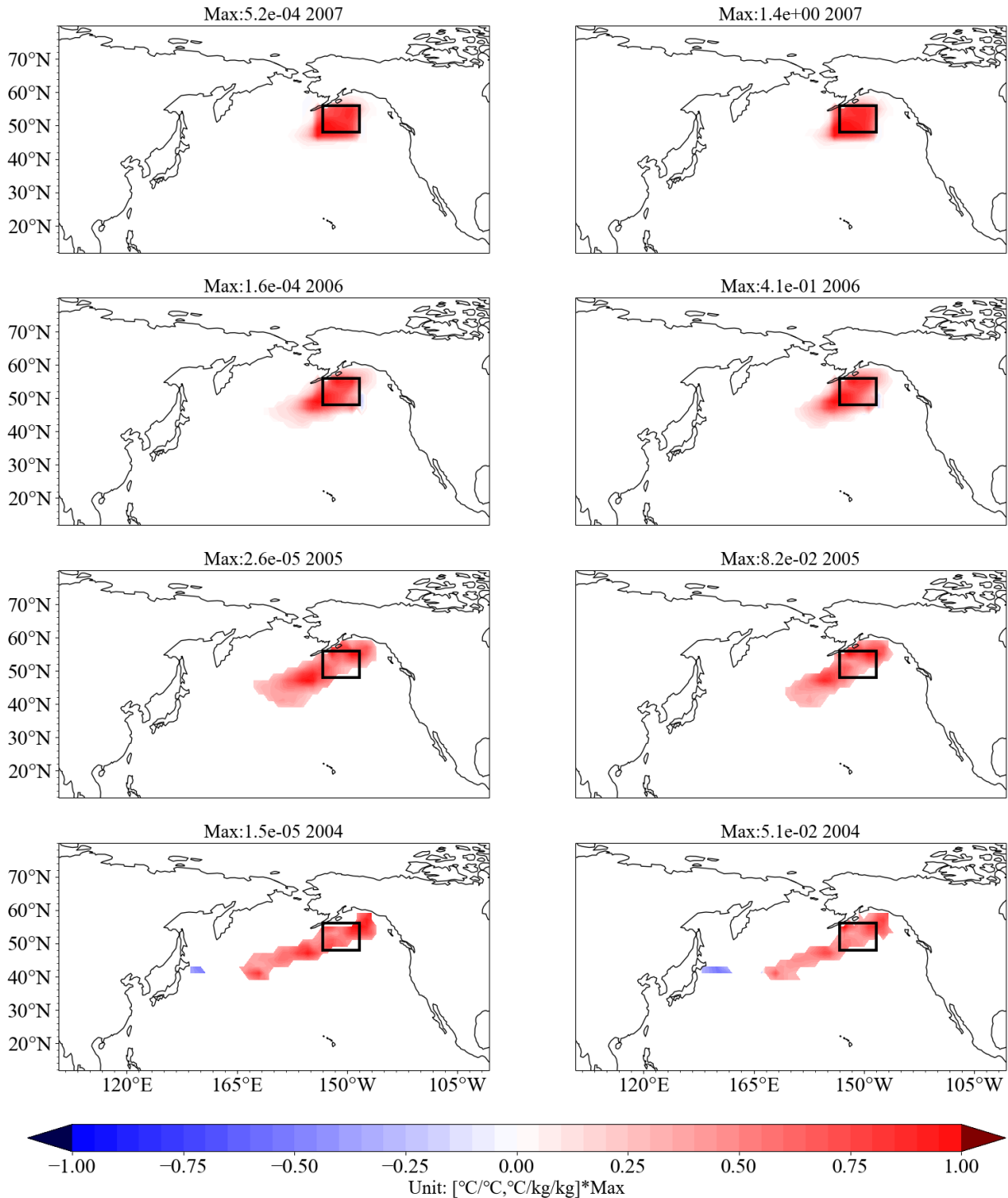


Fig. 4.1.3. Evolution of the adjoint sensitivity (from top to bottom, backward in time) with respect to T2M (left) and SH (right) based on the experiment setting 2007 (non-MHW year) as the target year. In each panel, sensitivities are normalized by their approximately maximum magnitude, as labeled in the titles of each panel. The black box indicates the respective target research region.

### 4.1.3. NEP MHW Sensitivities

#### *a. Adjoint Sensitivity Pattern*

Based on the sensitivity fields of EXP1 for region 1 and EXP2 for region 2, [Figs. 4.1.4 - 4.1.10](#) showcase the adjoint sensitivities of the cost function ([Eq. 3.6](#)) with respect to five different parameters (potential temperature, salinity, PRE, U, and V) at various time lags during the 4-year period. In each case, a positive (negative) sensitivity implies that positive perturbations at that location and at the shown time will induce a positive (negative) change in heat content in the NEP target region during the target year.

[Fig. 4.1.4](#) shows adjoint sensitivity fields of the cost function with respect to the initial condition of potential temperature at the surface, separately for region 1 and region 2. The displayed pattern represents also those obtained for individual heat flux components (T2M, SH, LW, and SW). Any positive perturbation will enhance the annual mean upper ocean heat content through changes in the sensible heat flux and latent heat flux (together called turbulent surface heat fluxes) as specified by bulk formula package ([Eq. 3.1a, b](#)) in MITgcm. Near-surface heat content changes can be driven locally through local surface forcing; they can also be driven remotely by heating the water that later gets advected into the target region. Changes in the heat content in the target region can also be driven dynamically by altering the heat advection through flow field changes and its heat convergence.

The propagation of heat content sensitivities of regions 1 and 2 ([Fig. 4.1.4](#)) are mainly confined to midlatitudes north of 40°N of the NP as one would expect given the pattern of the NP circulation. Sensitivities from both regions consistently show positive values within the target region across most time lags, confirming that a persistent local surface heat flux forcing distributed over four years will lead to enhanced temperatures in the target region during the target year. Along these lines, during the target year, the sensitivities are confined locally to the target region, indicating the predominant importance of local warming. However, toward earlier years, the sensitivities shift horizontally, spreading across a broader region with maximum values occurring more toward the west – upstream – of the target area, highlighting the increasing importance of regional/remote influences (preconditioning) from those earlier times. As an example, during -2yr (2012) and -3yr (2011), sensitivity fields of both target regions expand towards the middle of the NP and display a banded distribution. In that sense,

the far-field sensitivity of both regions is comparable and indicates that the heat content of both regions is sensitive to surface heating anomalies of the central Pacific but with opposite signs in certain areas (also in certain months, examples can be seen from [Fig. 4.1.3](#)) leading to density gradients and associated thermal wind flow field changes.

Marotzke et al. ([1999](#)) split the sensitivity into dynamic velocity-related (density-related) and kinematic (advected temperature-related) components:

$$\left(\frac{\partial Q}{\partial T}\right)_\rho = \left(\frac{\partial Q}{\partial T}\right)_S + \alpha\rho \left(\frac{\partial Q}{\partial \rho}\right)_T = \left(\frac{\partial Q}{\partial T}\right)_S + \frac{\alpha}{\beta} \left(\frac{\partial Q}{\partial S}\right)_T \quad (4.1.1)$$

In this equation [Eq. 4.1.1](#),  $Q$  denotes heat transport, while  $T$  and  $S$  represent the initial temperature and salinity, respectively.  $\rho$  represents density; and  $\alpha$  and  $\beta$  are the thermal and haline expansion coefficients, respectively. If the sensitivity fields of temperature and salinity are of opposite signs (and correct magnitude), the effect is purely dynamical, otherwise it is a combination of dynamical and kinematic. More details can be found in Marotzke et al. ([1999](#)). Along these lines, the sensitivity to SST changes ([Fig. 4.1.4](#)) is a mix of kinematic and dynamic signals. The dynamic part is basically illustrated by the salinity sensitivity ([Fig. 4.1.5](#)) showing a dipolar, i.e., density gradient-related distribution, which promotes anomalous northward advection into the target region during the target year. During the years before the pattern shifts to a northeastward advection towards a region that is increasingly shifted westward of the target region. That means in the years before anomalous advection will heat a region of water that will get advected into the target region. It is notable that the salinity sensitivity pattern mirrors those of precipitation ([Fig. 4.1.6](#)). In the same vein, in the deeper ocean, the pattern of sensitivities from temperature ([Fig. 4.1.7](#)) and salinity ([Fig. 4.1.8](#)) match nearly perfectly with opposite sign, which indicates that the mechanism is purely dynamical, that is, only density and consequently velocity is to be changed to influence the heat transport.

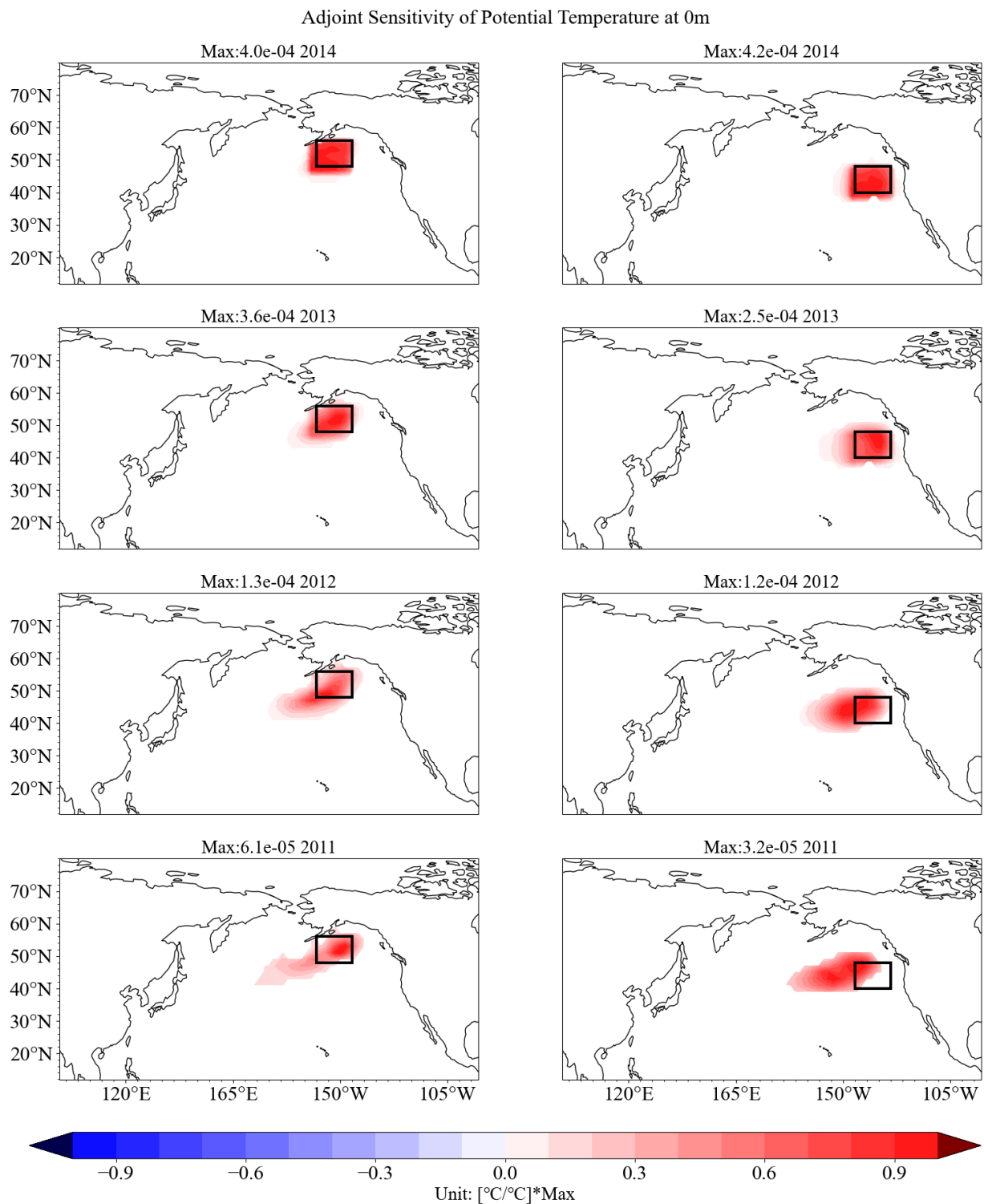


Fig. 4.1.4. Evolution of the adjoint sensitivity (from top to bottom, backward in time) with respect to the initial condition of potential temperature at the surface based on EXP1 (left column; for region 1) and EXP2 (right column; for region 2). In each panel, sensitivities are normalized by their approximately maximum magnitude, as labeled in the titles of each panel. The black box indicates the respective target research region.

Adjoint Sensitivity of Salinity at 0m

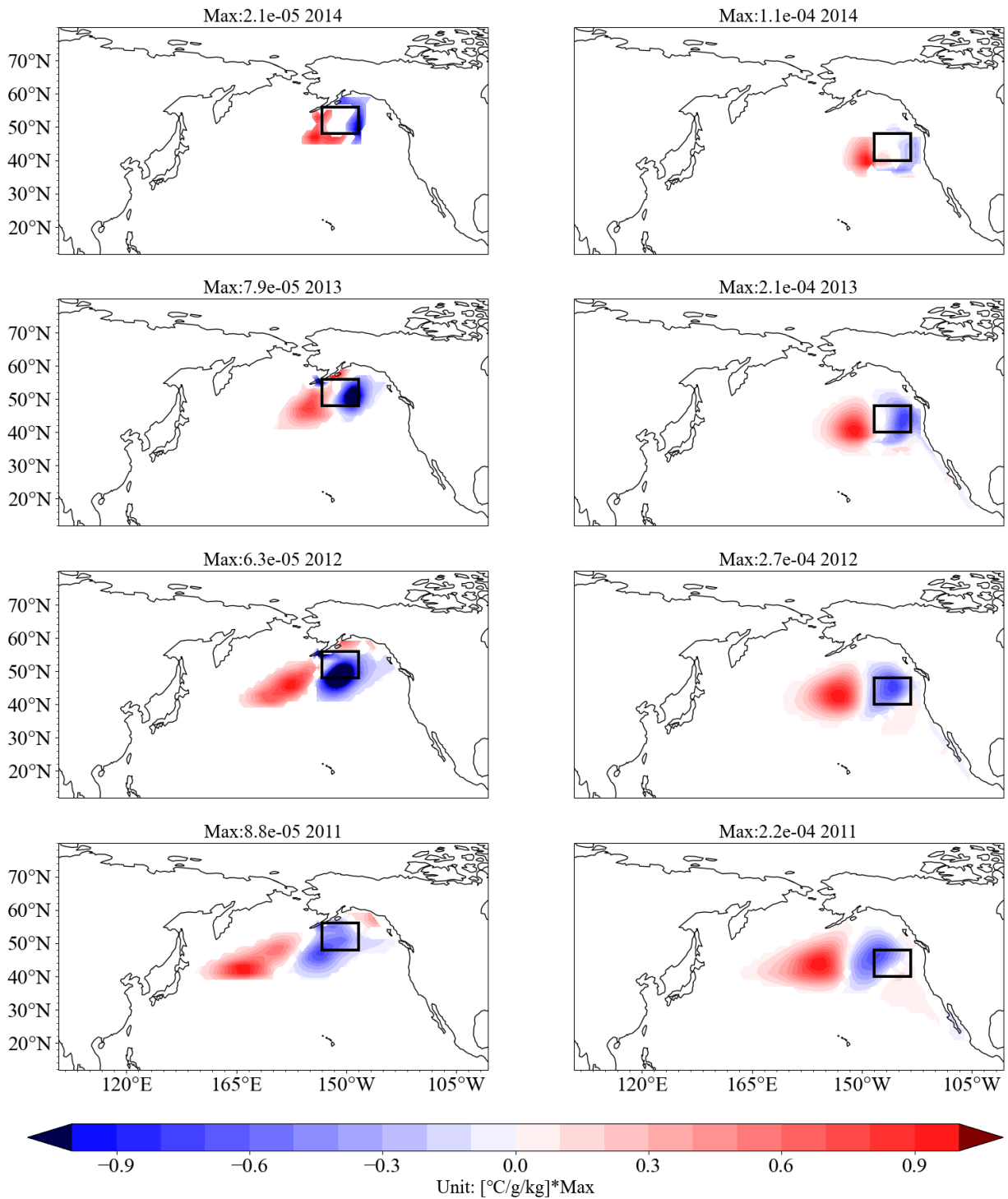


Fig. 4.1.5. As Fig. 4.1.4, but with respect to the initial condition of salinity at the surface.

Adjoint Sensitivity of PRE

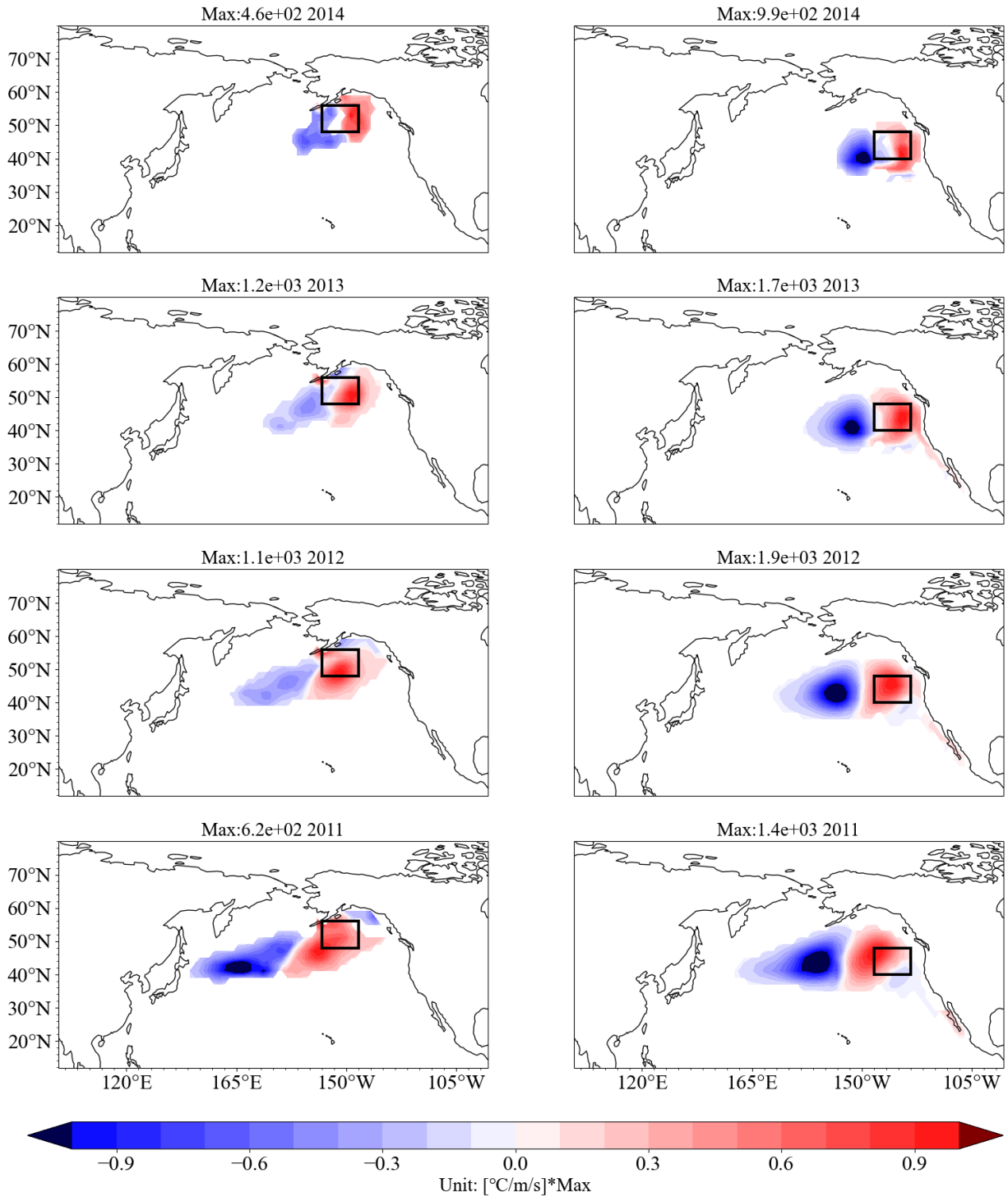


Fig. 4.1.6. As Fig. 4.1.4, but with respect to precipitation.

Adjoint Sensitivity of Potential Temperature at 1335m

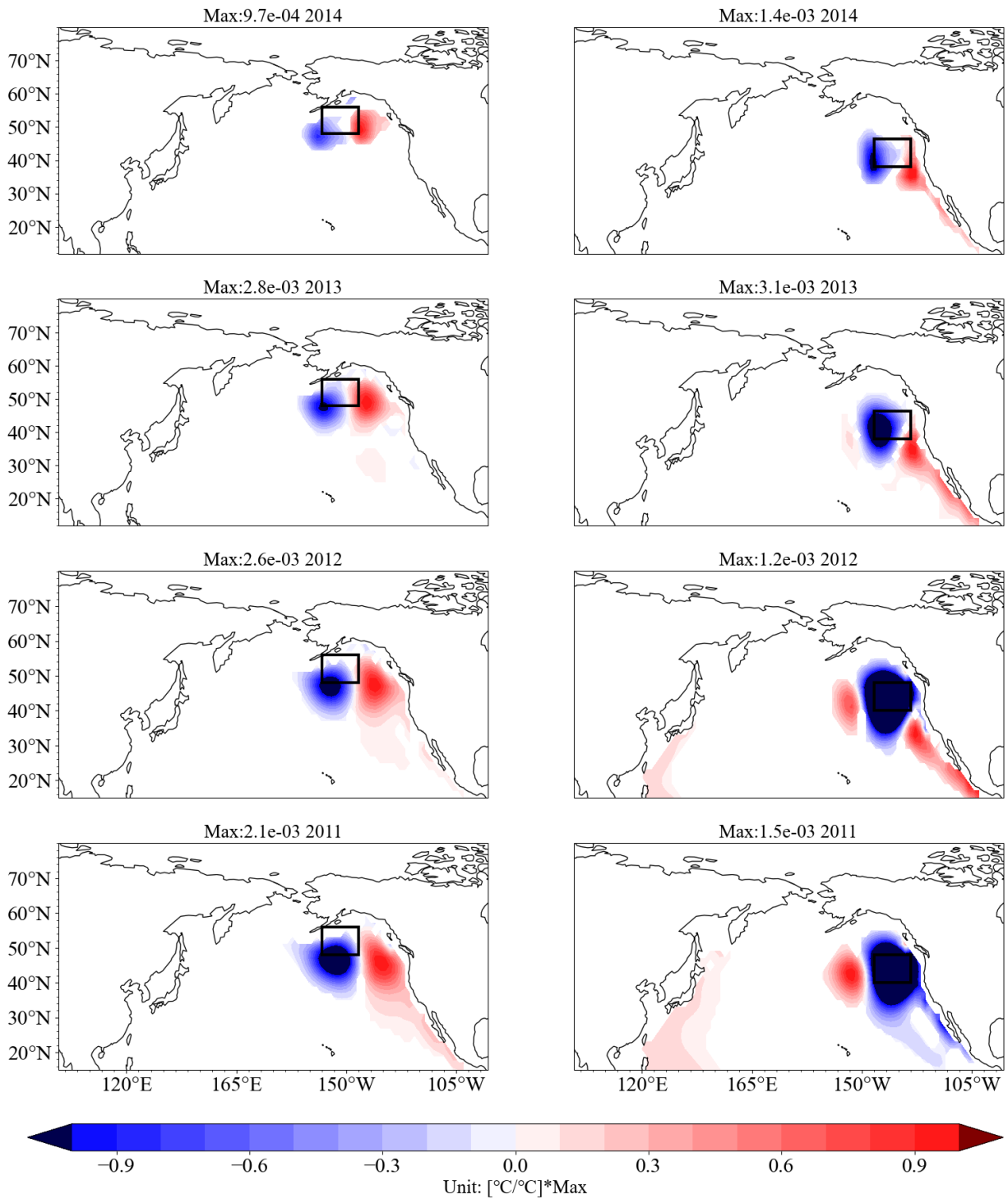


Fig. 4.1.7. As Fig. 4.1.4 but at a depth of 1335 m.

Adjoint Sensitivity of Salinity at 1335m

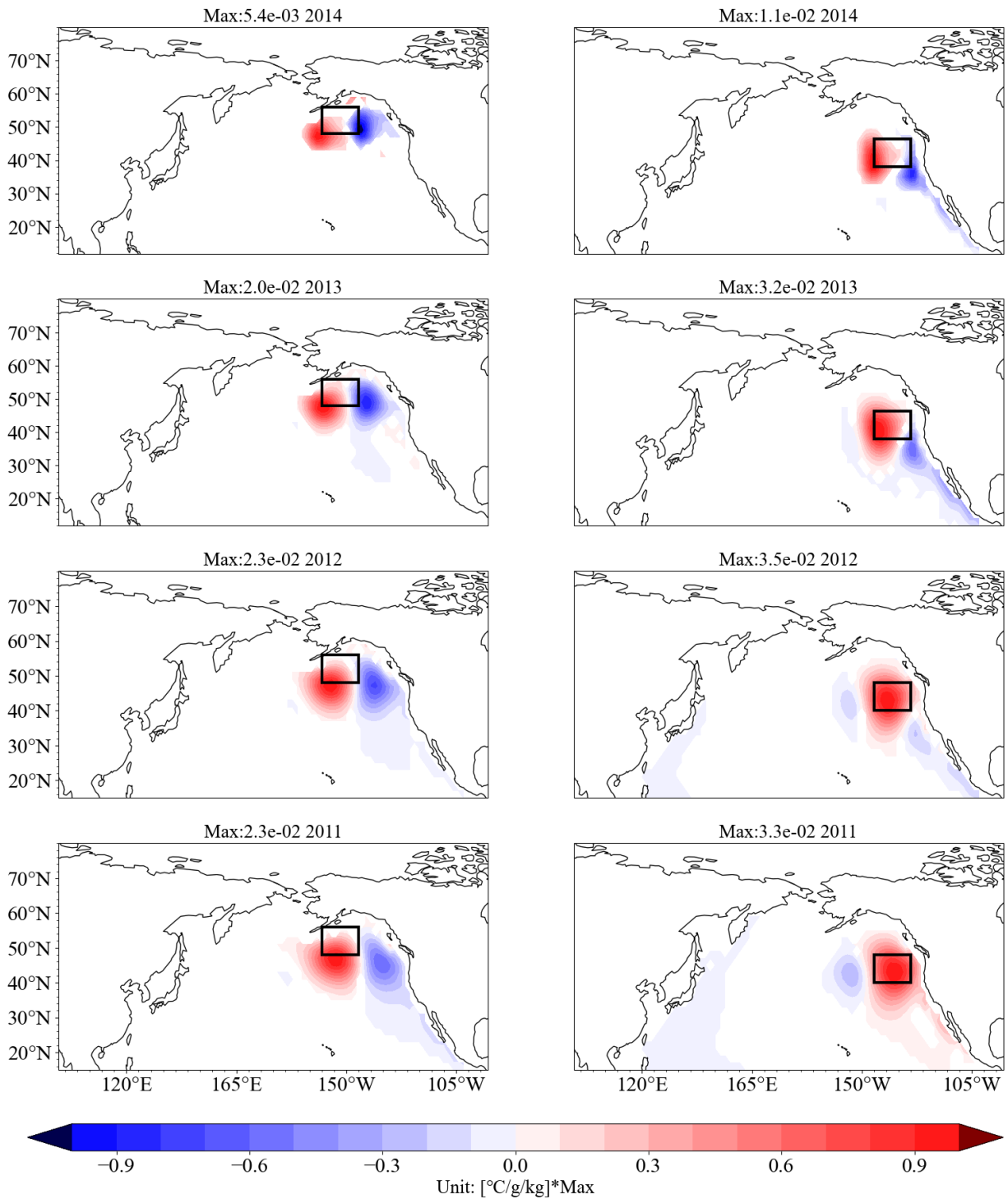


Fig. 4.1.8. As [Fig. 4.1.5](#) but at a depth of 1335 m.

As discussed before, the sensitivity of SH is quite similar to that of both T2M and potential temperature ([Fig. 4.1.4](#)), as well as to that observed in 2007 ([Fig. 4.1.3](#)). This results in a comparable level of contribution from both the latent heat flux ([Eq. 3.1b](#)) and the sensible heat flux ([Eq. 3.1a](#)). At high latitudes, anomalies in the latent heat flux and sensible heat flux are of similar magnitude since cold air holds less moisture and small changes in temperature can only lead to small changes in specific humidity. Also, at middle to high latitudes, the sensible heat flux and latent heat flux are more dependent on temperature and humidity anomalies, while in the tropics and subtropics, they are primarily associated with wind speed anomalies ([Alexander, 2010](#)).

[Fig. 4.1.9](#) shows the adjoint sensitivities of the cost function with respect to zonal wind velocity ( $\partial J/\partial u$ ) at various time lags during the 4-year period. The figure reveals pronounced sensitivities of the heat content in region 1 to U. Similarly, large sensitivities to V ([Fig. 4.1.10](#)) are found which together would change the wind stress curl. Among horizontal winds, V exerts less influence compared to U. However, the sensitivity fields indicate that the NEP is sensitive to the region along the western coast of the Americas to a certain degree.

But in more general terms impacts from wind velocity on the heat content of the target regions can come through several pathways: horizontally one expects an impact on surface momentum fluxes and respective dynamical responses of the flow field, primarily Ekman currents, involving changing currents and advective pattern. Typically, this is driven by the wind stress curl altering the Ekman transports and the large-scale Sverdrup-type circulation. Although, there are potentially also implicit influences acting in the vertical, involving changes of the vertical mixing, entrainment or detrainment and associated mixed layer depth changes, those are not part of the sensitivity calculation since the adjoint code of the mixed layer parameterization had to be excluded for stability reasons. Changes in the wind speed will also impact surface turbulent heat fluxes ([Eq. 3.1](#)), which are being changed by a combination of the sensitivities of the T2M, SH, and wind sensitivities.

Adjoint Sensitivity of U

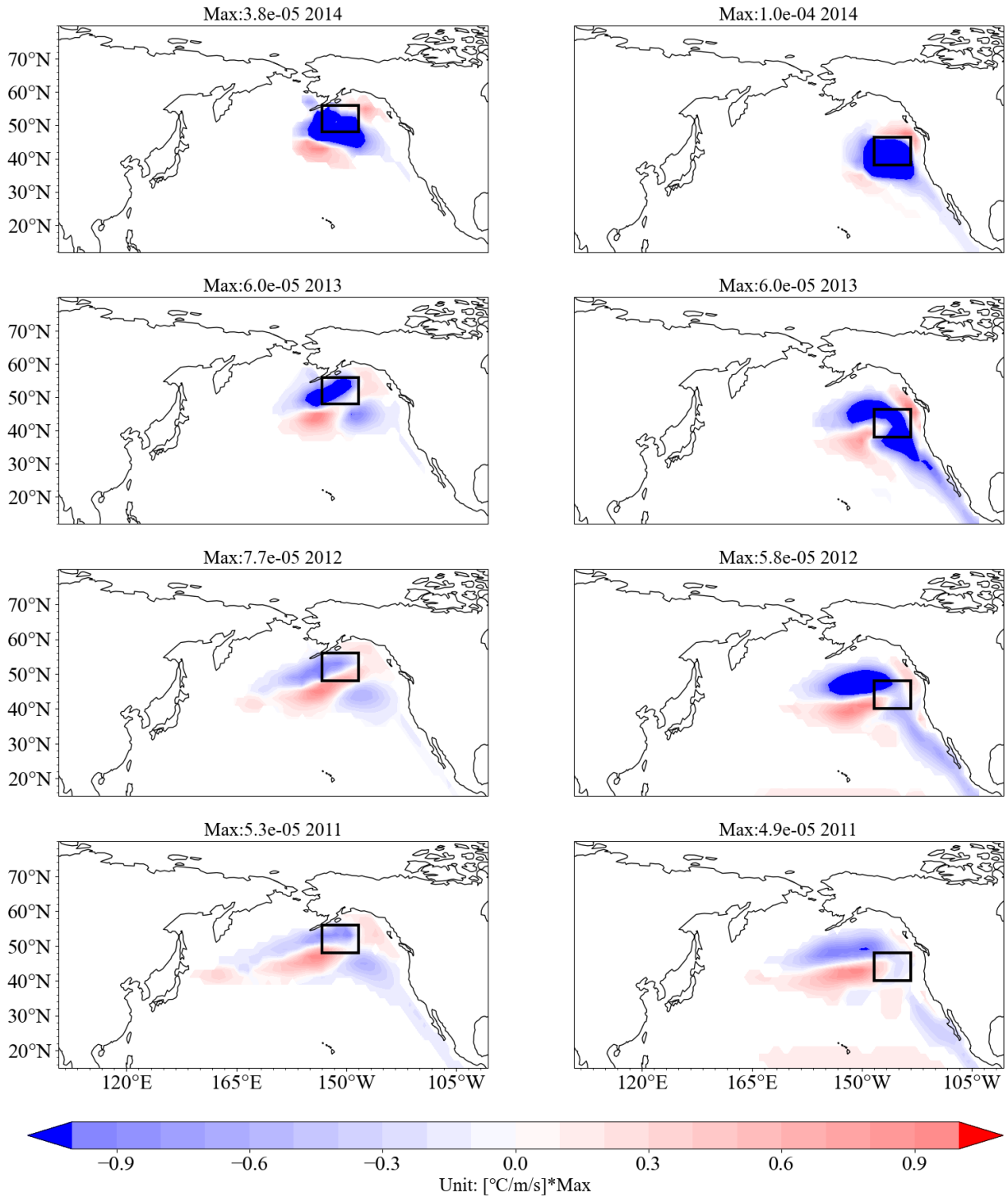


Fig. 4.1.9. As [Fig. 4.1.4](#) but with respect to U.

Adjoint Sensitivity of V

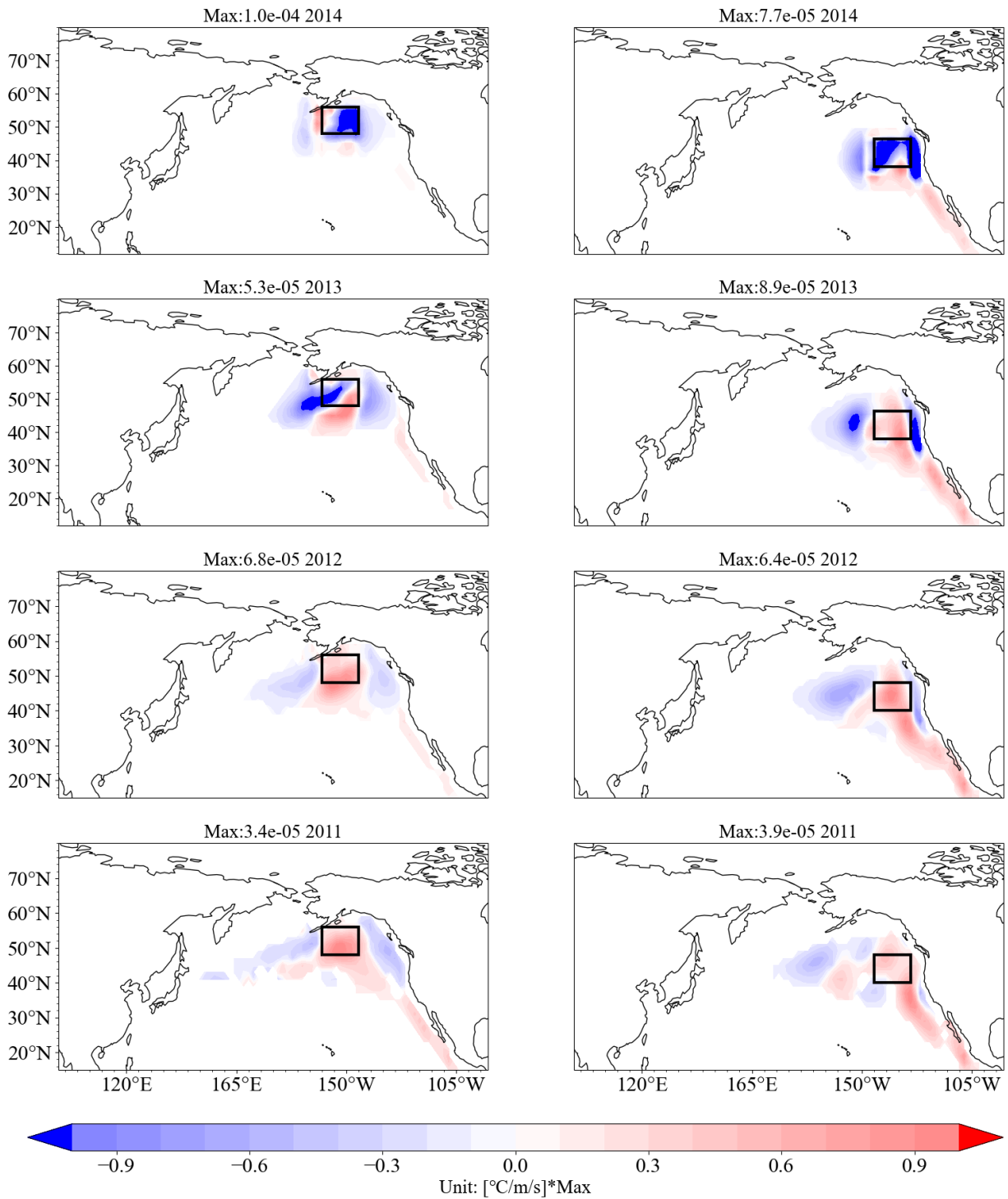


Fig. 4.1.10. As [Fig. 4.1.4](#), but with respect to V.

### *b. NEP Sensitivity Mechanism*

Adjoint sensitivity patterns such as those shown above illustrate optimal perturbation patterns of control parameters that – in this case - lead to heat content changes in the NEP. However, how these sensitivities accomplish the changes in the heat content in the target regions is not immediately obvious but needs further investigation.

Previous studies suggested that an important preconditioning for MHW to occur is the existence of atmospheric circulation anomalies that induce warm air advection which in turn drives temperature anomalies in the ocean ([Pfahl & Wernli, 2012](#)). Persistent high-pressure systems usually also bring calm winds that are not nearly strong enough to stir the ocean and cause the rise of the mixed layer interface and slow down wind-driven currents. According to Bond et al. ([2015](#)), the mechanisms contributing to specifically the 2014-2016 MHW in the NEP were reduced heat loss from the ocean, reduced advection of cold water into the region through reduced Ekman transports, and finally lowered mixed layer depth. All these mechanisms were linked to an unusually strong and lasting weather pattern characterized by above-normal sea-level pressure. Similar mechanisms were invoked to cause the 2019 MHW in approximately the same region involving an unusual and persistent weather pattern that resulted from a prolonged weakening of the NPSH ([Amaya et al., 2020](#)) and an MHW that was close in magnitude to the 2014-2016 event.

#### 1) CONTRIBUTION ANALYSIS

The adjoint sensitivities show how different AF can lead in principle to the heat content changes in the target region. To quantify how different AF affects in practice the total variation of SST and find out the dominant drivers, the linear change in  $J$  expected from an actual AF anomaly is calculated ([Eq. 3.7](#)). In this study lead time  $\Delta t$  is chosen to be 4-year because the sensitivity observed in the period before this time is notably weak. As the adjoint sensitivities appear to be independent of the actual ocean state, they can be shifted in time by full years. This is consistent with previous findings from Wang et al. ([2022b](#)).

By omitting the summation over space in [Eq. 3.8](#), one can visualize in one spatial map how at each location all AF contributes to the cost function response (top row in [Fig. 4.1.11](#)). While changing the summation over time into a cumulative sum and omitting the summation over forcing type yields in one temporal map the contribution of each month (in a cumulative sense)

and forcing type to the response (bottom row in [Fig. 4.1.11](#)), and in turn, estimate the linear contribution of actual AF anomalies. As sensitivity fields appear to be similar in all adjoint experiments, independent of the actual target year. The sensitivities of 2014 are used for the following analysis.

A contribution analysis can verify the usefulness of the sensitivity fields: the cost function change is reconstructed reasonably well. The reconstructed response in target region 1 is stronger and that of target region 2 weaker than the actual response (compare the actual response displayed as a blue bar with the final total response in the bottom row of [Fig. 4.1.11](#)). The deviation in the range 0.1-0.2 °C, in principle, can result from the linearization employed by reconstructing the response via [Eq. 3.12](#). The contributions from all AF anomalies are from rather local areas within the target area as the top row shows. On the other hand, it confirms that T2M and SH play important roles as atmospheric drivers of NEP MHWs through contribution analysis (bottom row in [Fig. 4.1.11](#)): the drivers of MHWs with different intensities are not different in the two target regions. In most experiments, LW emerges as the third most significant AF for warming which is significantly influenced by clouds and greenhouse gases, including water vapor. Horizontal winds and downward SW act essentially as a dampening factor for the upper 100 m warming; PRE, on the other hand, can be disregarded. The rapid growth period is from lead 15month to lead 10month (EXP1) and from lead 15month to lead 8month (EXP2). The total contribution peaks at lead 11month for both, contributed by SH, T2M, and downward LW (middle and bottom rows in [Fig. 4.1.11](#)). From this contribution analysis, it can be concluded that for the annual mean MHW observed in 2014, the most sensitive period occurred from October 2013, which is three months prior to the target year.

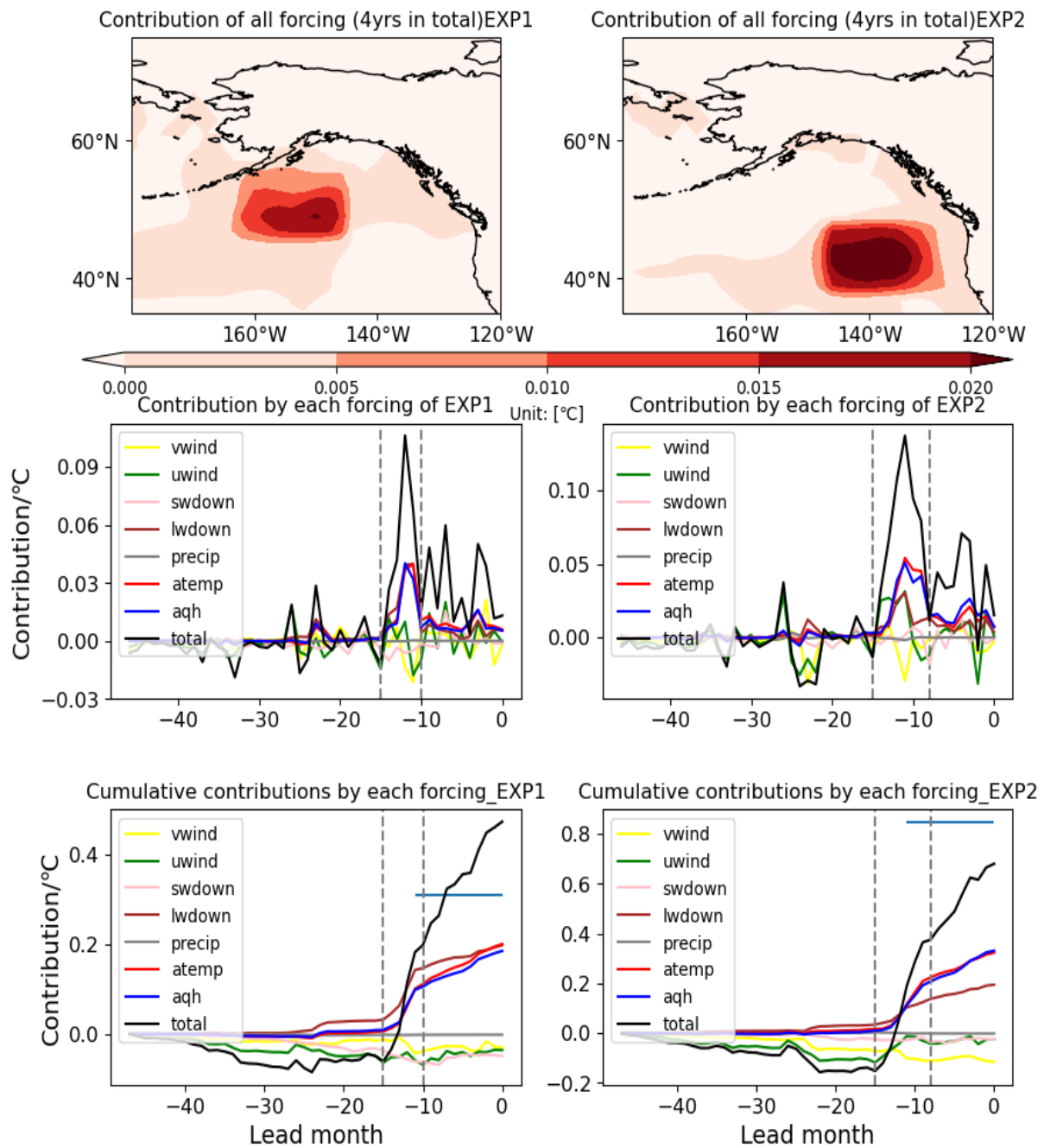


Fig. 4.1.11. (Top row) Total contributions of all AF anomalies by region to the cost function response ( $J(x, y)$ ). Note, that the distribution indicates in which region the forcing anomaly contributes but not where the response will take place. (Middle row) The contribution to the response by each AF in regions 1 and 2. The black line shows how all AF anomalies build up the total response, and the other different colors indicate the contributions of individual AF anomalies. The Gray dashed line shows the period of rapid growth. (Bottom row) Time evolution of the cumulative contributions to cost function response in regions 1 and 2 by the different actual AF anomalies ( $\delta F_i(\Delta t)$ ). The blue bars show the 2014 observed annual mean potential temperature anomalies of the upper 100 m in the target region.

## 2) PERTURBATION EXPERIMENTS

To explore the mechanisms that can lead to heat content changes based on both the sensitivities shown above and the dominant drivers from the contribution analysis, several perturbation experiments have been conducted by adding sensitivity-based perturbations to AF fields during various lead months and at different locations targeting responses in region 1. Since T2M and SH are the two dominant factors, and since the sensitivities and the contribution to both are very similar, only T2M is shown as an example. The sensitivity-based perturbation fields for T2M and horizontal wind are added to the original forcing of the forward model, which are calculated according to [Eq. 3.13](#):

$$\Delta T2M(x, y, t) = \frac{\partial J / \partial atemp|_{(x,y,t)}}{\max(|\partial J / \partial atemp|)} \cdot \delta \cdot T2M_{std}(x, y) \quad (4.1.2a)$$

$$(\Delta u(x, y, t), \Delta v(x, y, t)) = \left( \frac{\partial J / \partial u|_{(x,y,t)}}{\max(|\partial J / \partial u|)} \cdot \delta \cdot u_{std}(x, y), \frac{\partial J / \partial v|_{(x,y,t)}}{\max(|\partial J / \partial v|)} \cdot \delta \cdot v_{std}(x, y) \right) \quad (4.1.2b)$$

The resulting perturbations are added to the respective forcing fields over a 4-year period and the model is integrated forward; results are analyzed as anomalies with respect to the control run.

[Fig. 4.1.12](#) shows the annual mean potential temperature anomalies resulting from perturbations of the T2M and the horizontal wind (U and V) in the top 160 m. In both cases, the impact of perturbation before -3yr is very small and almost neglectable. Thus, only results after -2yr are presented. Both the T2M perturbation experiment and the horizontal wind perturbation experiment show the expected local heating in the upper 100 m in the target region after a 4-year run, even though there is some noise in the western Pacific which may be due to chaos. The temperature signal during the target year at the sea surface caused by T2M perturbation ( $\sim 0.44^\circ\text{C}$ ) is almost 2 times the signal caused by the horizontal wind velocity ( $\sim 0.27^\circ\text{C}$ ). Unlike the T2M perturbation experiment, for which the heating in the target region is local and constrained to the top 100 m (consistent with the cost function definition), the horizontal wind perturbation experiment shows an upward vertical propagation from regions further south (around  $30^\circ\text{N}$  at -2yr) of the deeper ocean.

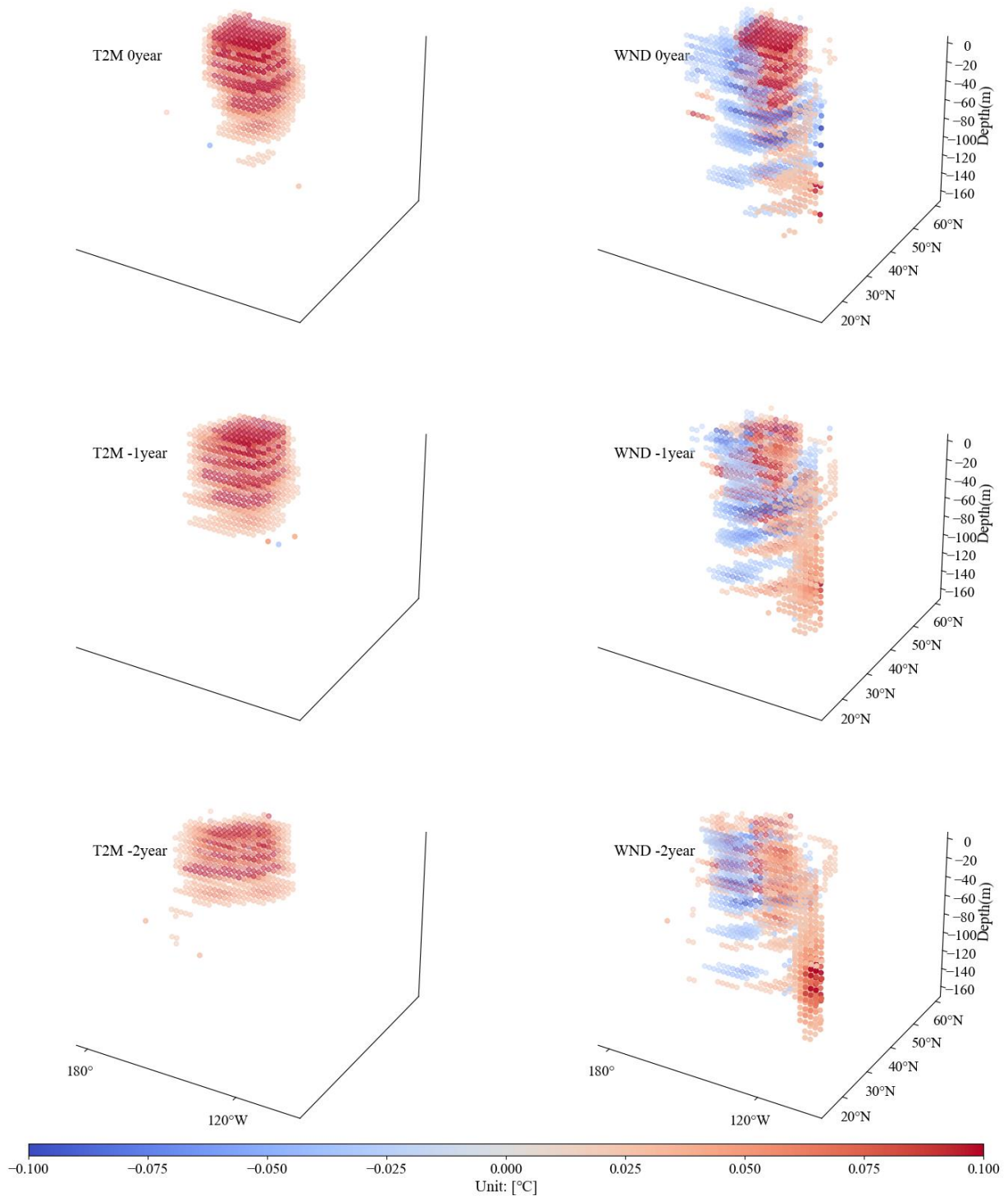


Fig. 4.1.12. 3-D temporal evolution of annually averaged potential temperature anomalies (perturbation run – control run) for experiment perturbed by T2M (left) and horizontal wind velocity (right), respectively (from bottom to top, forward in time). Absolute values less than 0.02 in magnitude are not shown.

Associated changes in SSH are shown in [Fig. 4.1.13](#). Adding perturbations to T2M didn't significantly change SSH of target region 1; only during -1yr and the target year (Year 0) notable positive steric SSHa are confirming that in this case, the essential heat uptake takes place locally in the target year through altered air-sea fluxes (SSHa in the far-field of the Kuroshio are likely to be a result of chaos). In contrast, adding perturbation by horizontal wind velocity leads to substantial changes in the near-surface geostrophic flow field reflected in the SSH gradients reaching across the basin, and revealing a mid-latitude gyre scale pattern. During the target Year 0 positive SSHa are dominated by the warming in the target region and negative anomalies in the regions that have provided the heat. There is some alignment with the subpolar and subtropical gyres suggesting a weakening of the gyres associated with the MHW event. Years prior to this are dominated by the spinup of the gyre-like anomalies and revealing also a northward current anomaly near 150°W that could contribute to the heating in the target region. The figure confirms that the horizontal wind can be a driver to the heating of the target region through the advection of heat, although it is not a main driving factor for the 2014 upper 100 m MHW.

[Figs. 4.1.12](#) & [4.1.13](#) show the responses to adding either T2M perturbations or horizontal wind perturbations. To analyze the complete mechanisms involved in the warming and to compare them to literature results, a final run was performed in which all forcing perturbations according to [Eq. 3.13](#) were added simultaneously to the respective forcing fields over a 4-year period prior to 2014. From the results, after subtracting the trajectory of the control run, various terms driving the heat content budget in the target regions are analyzed. [Fig. 4.1.14](#) shows the resulting net surface heat flux anomalies, wind stress curl anomalies, and advective flux anomalies by subtracting the control run from the perturbation run. Positive values indicate heat flux entering the ocean. The downward SW acts as a damping term to the NEP MHW from the contribution analysis for the year 2014 ([Fig. 4.1.11](#)). The net surface heat flux behaves positively in Year 0 after the addition of the perturbation. In other words, the turbulent heat flux plays a crucial role in heating the target region for MHW year 2014. Negative wind stress curl pushes water downward (Ekman pumping) so that warm surface water enters from the side leading to a deepening of the warm surface layer. The total advective flux anomaly in the target region is positive in the target year, with positive horizontal advective flux propagating from west to east. Additionally, the presence of negative vertical advective flux indicates downward movement within the target region. This finding is consistent with the

work of Bond et al. (2015), which suggests that the anomalous advection can drive interannual temperature anomalies.

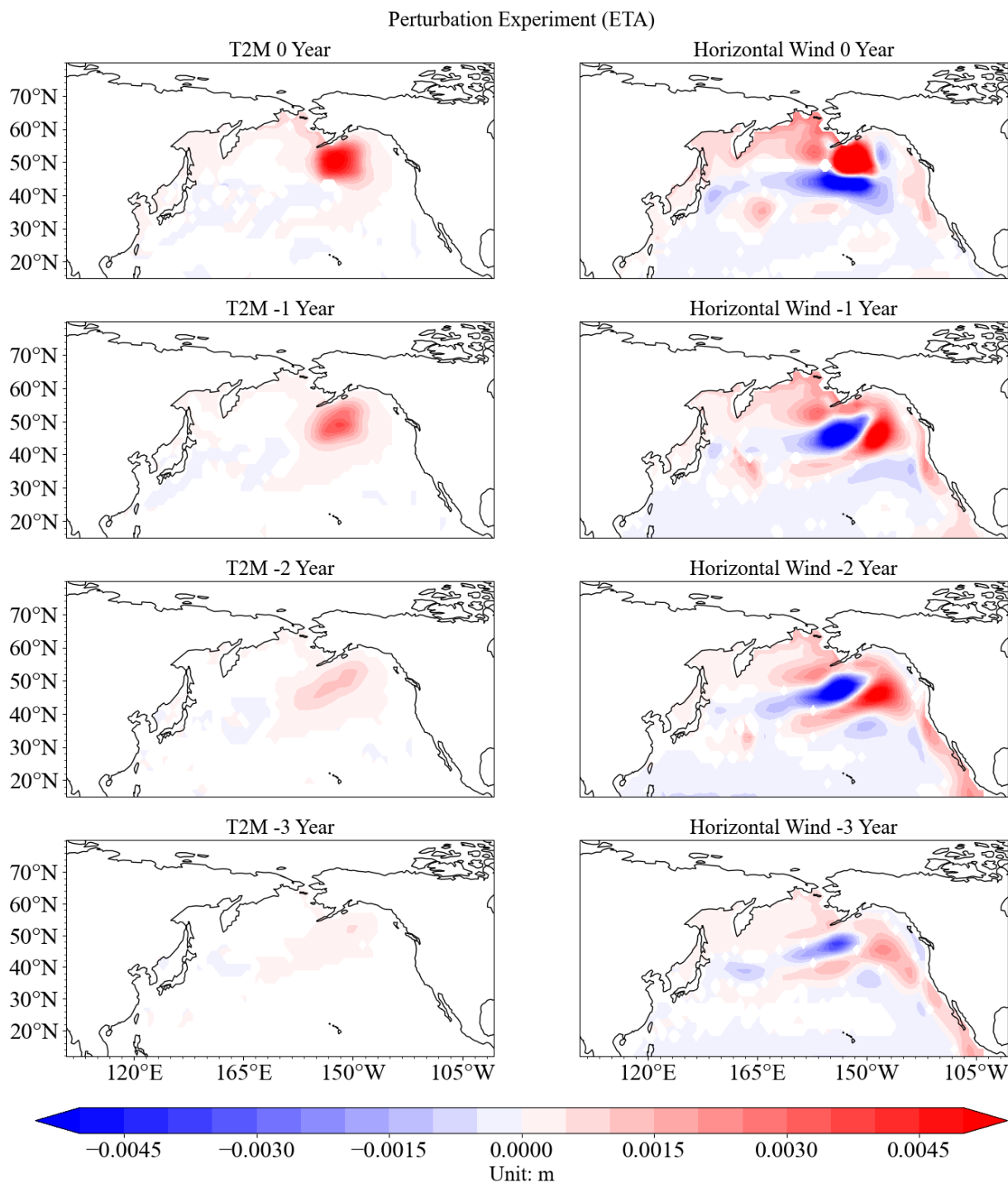


Fig. 4.1.13. Temporal evolution of annually averaged SSHa (perturbation run – control run) for experiment perturbed by T2M (left) and horizontal wind (right), respectively (from bottom to upper, forward in time).

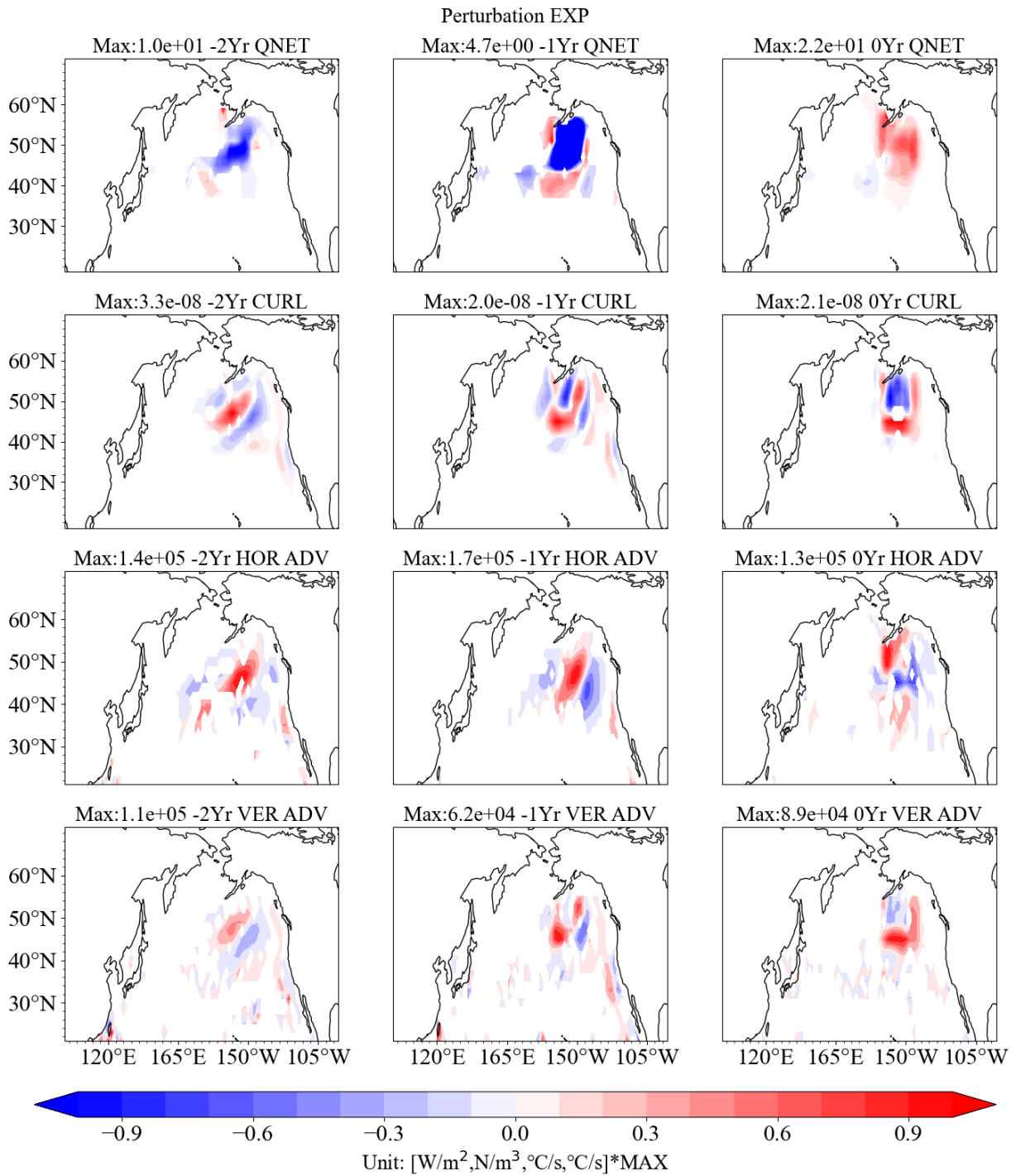


Fig. 4.1.14. Temporal evolution of annually averaged (first row) net surface heat flux, (second row) wind stress curl, (third row) horizontal advective flux ( $u \frac{\partial \theta}{\partial x} + v \frac{\partial \theta}{\partial y}$ ) and (fourth row) vertical advective flux anomalies ( $\omega \frac{\partial \theta}{\partial z}$ ) of potential temperature at the surface (perturbation run – control run) for the experiment perturbed by all AF (from left to right, forward in time).

#### 4.1.4. NEP MHW Reconstruction

To validate the adjoint sensitivity results, SST anomalies were reconstructed (hind-cast) for the entire period 1990 through 2022, following the approach used above by defining the cost function as 2014 SST and rerunning the sensitivity experiment, again using the resulting sensitivities from 2014 and incorporating all actual AF anomalies. The results ([Fig. 4.1.15](#)) effectively produce a hindcast that captures a substantial portion of the variability of SSTa. The correlation coefficient between the reconstruction and reanalysis for the whole period is 0.87 for region 1 and 0.93 for region 2 and the two-tailed p-value is also far less than 0.05 indicating the correlation is statistically significant (the year 2014 was excluded to conduct an out-of-sample test; the results for 2014 can be seen in [Fig. 4.1.11](#)). The dashed yellow line represents the HadiSST anomalies for the respective region, while the orange line depicts the reconstruction of mean temperature anomalies using the sensitivity pattern derived from the 4-year periods. The reconstruction is successful not only for the recent decades but also for the entire period, with the exception of some cooling years around the 1970s, where underestimation is observed. Although the reconstruction tends to slightly underestimate the cooling in the NEP for certain years, it performs well during years of extreme heating.

Bars in [Fig. 4.1.15](#) depict the contributions from different AF to the respective SSTa and confirm that in the majority of warming events SH and T2M are the main drivers, contributing almost the same amount to the final response. In other words, latent heat flux ([Eq. 3.1b](#)) and sensible heat flux ([Eq. 3.1a](#)) are the most important drivers of NEP MHWs, especially the latent heat flux which at the end is being changed by a combination of the sensitivities of the T2M, SH, as well as wind sensitivities. LW is also the third important driver of SSTa. In contrast, horizontal wind velocity contributes relatively more to cooling events. Precipitation can be ignored due to the negligible contribution on a longer time scale.

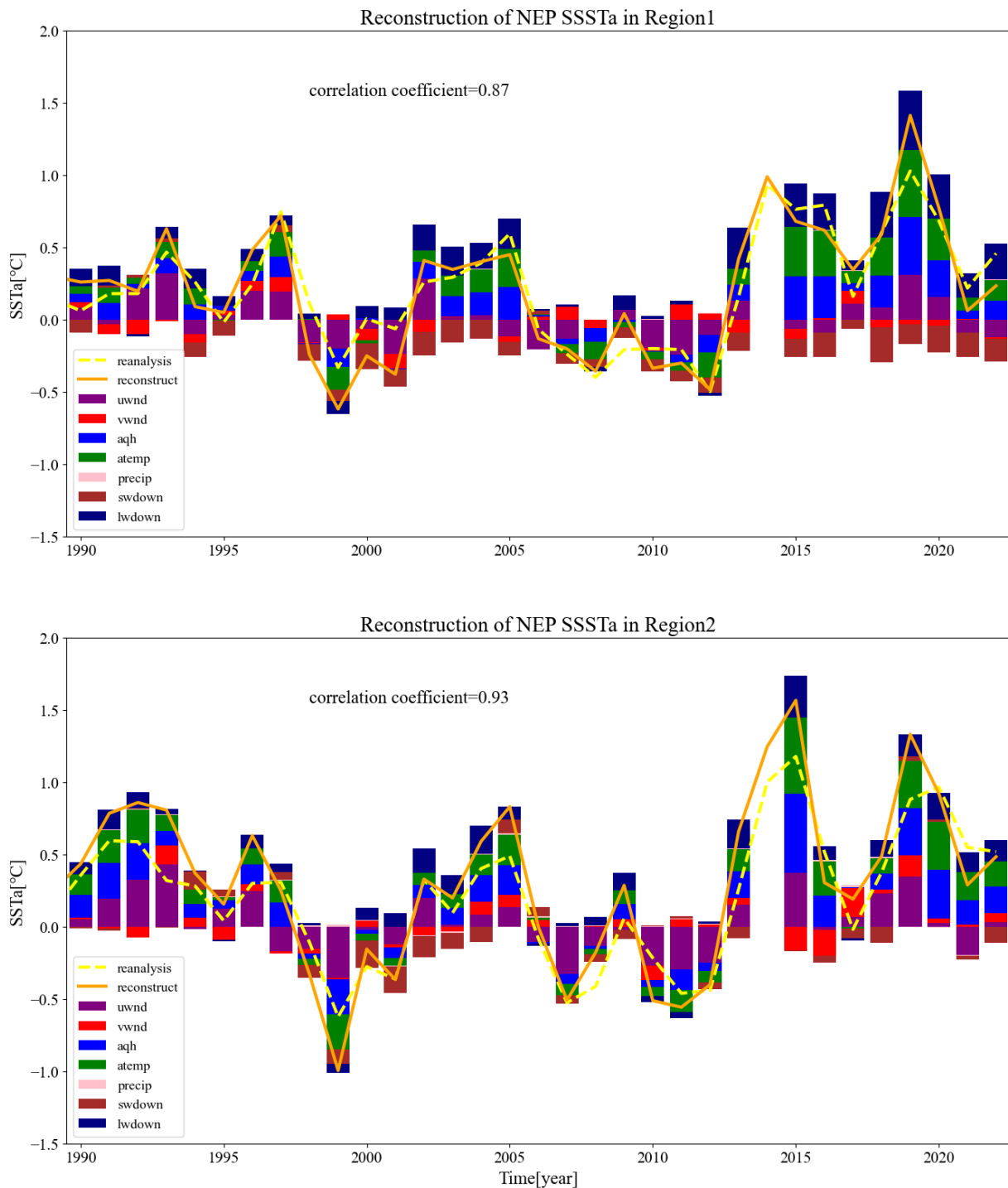


Fig. 4.1.15. Reconstruction of SSTa at NEP from 1990 to 2022 (top: region 1; bottom: region 2). Dashed yellow lines show the HadiSST reanalysis; orange lines represent the reconstructions using the first 4-yr mean sensitivity patterns of all adjoint experiments and all AF. Color bars show different contributions from AF (blue: SH; green: T2M; purple: U; red: V; brown: SW; navy: LW; pink: PRE). During the correlation analysis, the year 2014 was excluded to conduct an out-of-sample test.

To compare the relative importance of different AF contributions between MHW and non-MHW years, the percentage contributions of T2M, SH, LW, and U and their probability distribution function ([Fig. 4.1.16](#)) are calculated based on their absolute values from [Fig. 4.1.15](#). For MHW years, T2M, SH, and LW are undoubtedly the most important contributors to enhanced temperatures (always 20%-35% of total contribution), which push them into the upper 60th percentile, while U shows lower contributions mostly (except for one case) in the lower 40th percentile. For other years, T2M, SH, and LW contribute 10%-20% in general. Together with U, these four factors impact the temperature in the NEP region by more than 50%. During MHW years, they typically account for up to 80%-90% of the warming.

For some non-MHW years, T2M and SH sometimes only contribute 10% (e.g. 1995, 2001). At the same time U contributes more, i.e., enhanced wind stress plays a more important role when the turbulent heat flux contributes less. Apart from that, U dominates the cooling event in some cases. Between 2006 and 2012, the target region experienced a period of cooling ([Fig. 4.1.15](#)) which U takes up around 40%-60% of total cooling (up to 80% in 2006). And when the target region is relatively warm, U always contributes only nearly 10%-20%. The contribution of SH is slightly larger than that of T2M. As a result, it can be inferred that air-sea heat flux plays the dominant role in driving MHWs, surpassing the temperature advection effects.

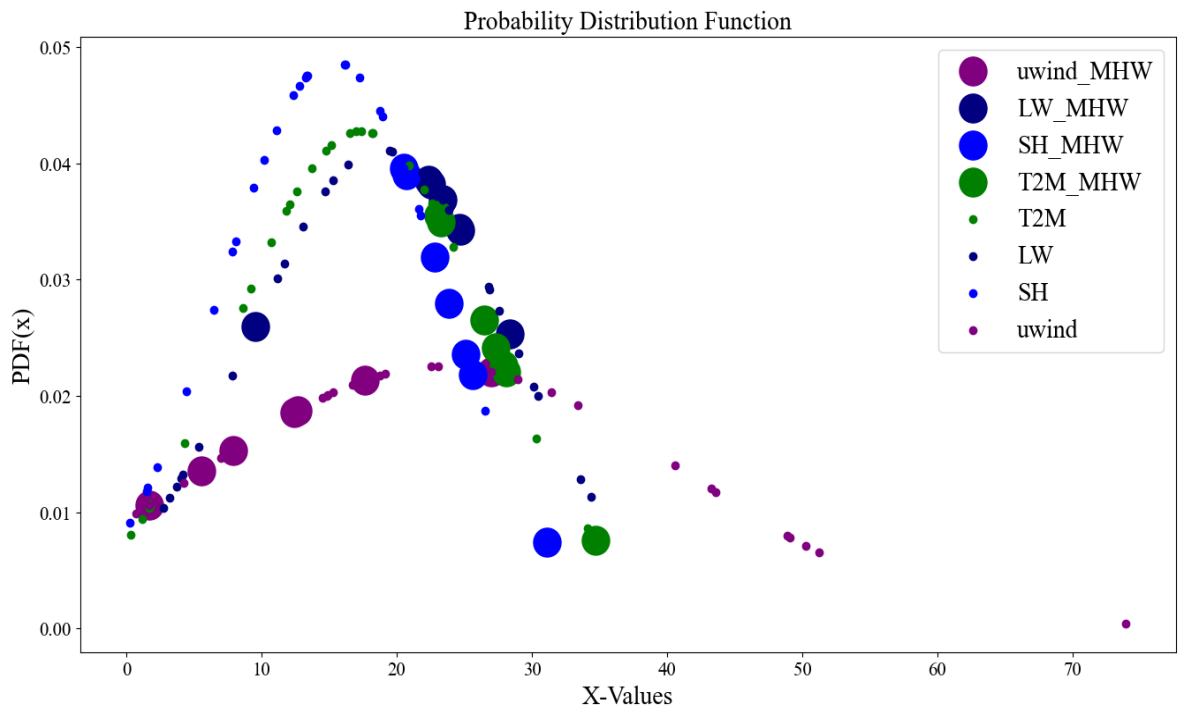
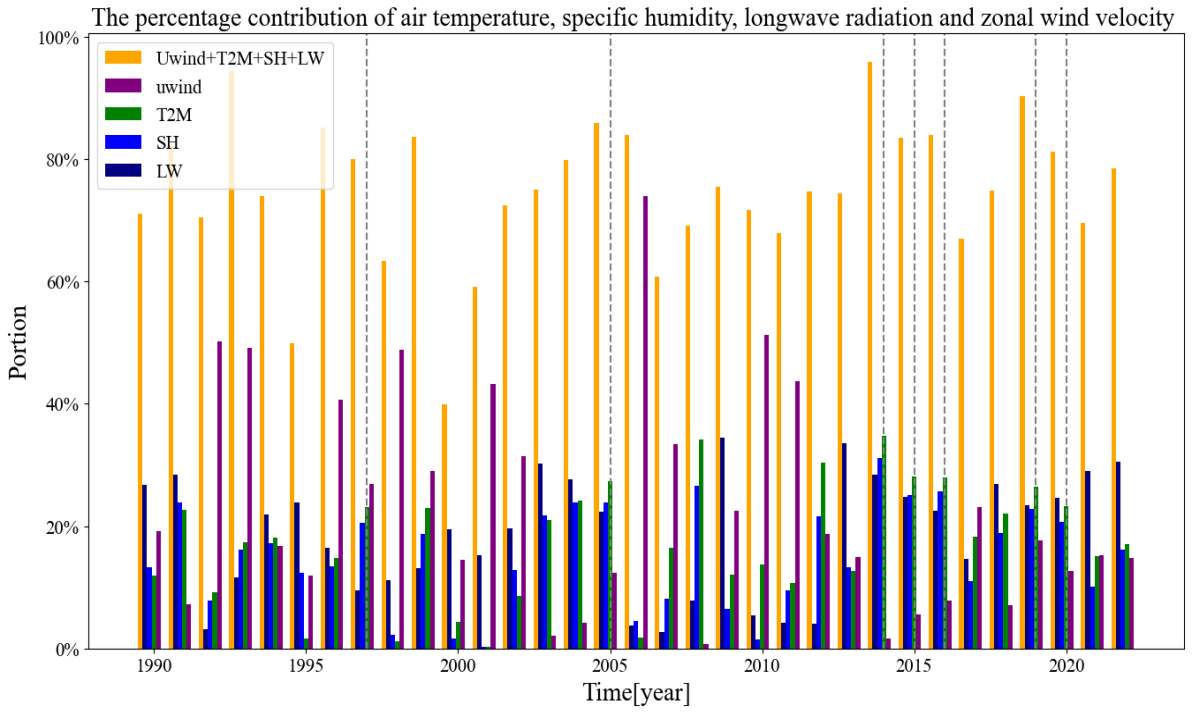


Fig. 4.1.16. (Top) The percentage contribution of T2M (green), SH (blue), LW (navy), U (purple), and the sum of them (orange) to temperature changes in region 1. The grey vertical dashed line shows MHW years. (Bottom) The probability distribution function of the percentage contribution (x-axis) of T2M, SH, LW, and U. Bigger dots indicate the MHW years.

### 4.1.5. NEP MHW Forecast Potential

Several studies have attempted to forecast MHWs using a variety of methods, including climate modeling (Jacox et al., 2022), machine learning (Giamalaki et al., 2022), and potentially the winter SST persistence. To explore the forecast potential of NEP MHWs using adjoint sensitivities, Fig. 4.1.17 shows the correlation coefficient between the reconstructions using different sensitivity periods and the HadiSST reanalysis data. All reconstructions using AF that start from lead 18month and ending after lead 15month successfully capture most heatwaves, with correlation coefficients exceeding 0.5. Sensitivity intervals spanning from -18mon (6-month prior to the target year) to -12mon (1-month prior to the target year) allow predicting the NEP MHW before the beginning of the MHW year with the skill level of 0.65.

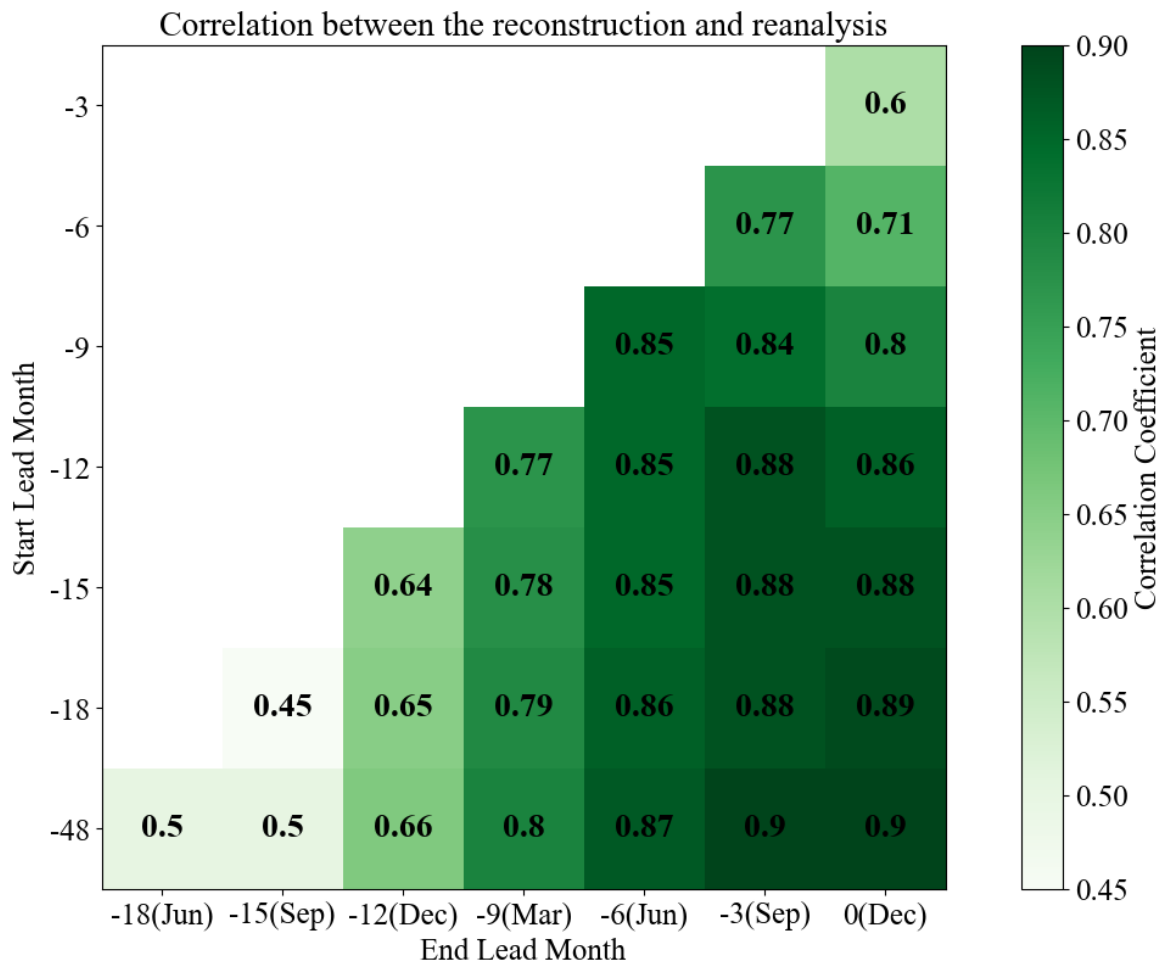


Fig. 4.1.17. The correlation coefficient between the reconstructions using different sensitivity periods and the HadiSST reanalysis data for all combinations of start (y-axis) and end month (x-axis). Numbers in boxes indicate those correlation coefficients that are significantly different from 0 ( $p \leq 0.05$ ).

To compare the adjoint method with statistical methods, further regression and correlation analysis are conducted. Using the modeled monthly mean SST in region 1, a regression analysis is performed with the lagged monthly mean AF (ranging from lag 0month to lag 36month). Results related to lag 0month are shown in [Fig. 4.1.18](#). Similar conclusions can be drawn from the regression analysis indicating that T2M, SH, LW, and horizontal winds exhibit high correlations with the cost function. For instance, when examining T2M, a relatively high correlation can be observed extending back up to -12mon or even longer, suggesting a strong relationship between region 1 and the equatorial ENSO region. However, the region exhibiting high correlation is substantially broader than the sensitive region identified by the adjoint method, suggesting it is challenging to identify the precise timing and location of sensitivity contributing to the target warming based solely on this kind of regression analysis. Utilizing perturbation experiments together with regression analysis may help identify the most sensitive areas and periods corresponding to the cost function; however, this approach appears to be less efficient than adjoint studies. Additionally, it is important to note that statistical methods, while useful for identifying correlations, may still lack physical explanations.

SST persistence is considered more effective for making predictions, as the primary conclusion suggests that local effects predominantly influence target warming. [Table. 4.1.1](#) presents a comparison of the correlations between the annual mean SST and the seasonal mean SST occurring in different time lags, which can be used to predict or reconstruct the annual mean SST in region 1. Utilizing December SST to predict the mean SST of the next year is a more straightforward approach, and the predictive skill (0.62) is relatively high, nearly matching that of the adjoint method shown in [Fig. 4.1.17](#) (-48mon ~ -12mon: 0.66). The advantage of forecasts based on the adjoint sensitivity is that their skill and lead time are likely to improve when applying the prediction of the AF. Moreover, extending the period of data does not enhance the skill of persistence methods; the highest correlation observed (0.69) occurs when using the mean temperature from the last three months of the previous year and the first three months of the target year. However, extending the period of data can improve the skill of the adjoint method (e.g. 0.8 from -48mon to -9mon, [Fig. 4.1.17](#)).

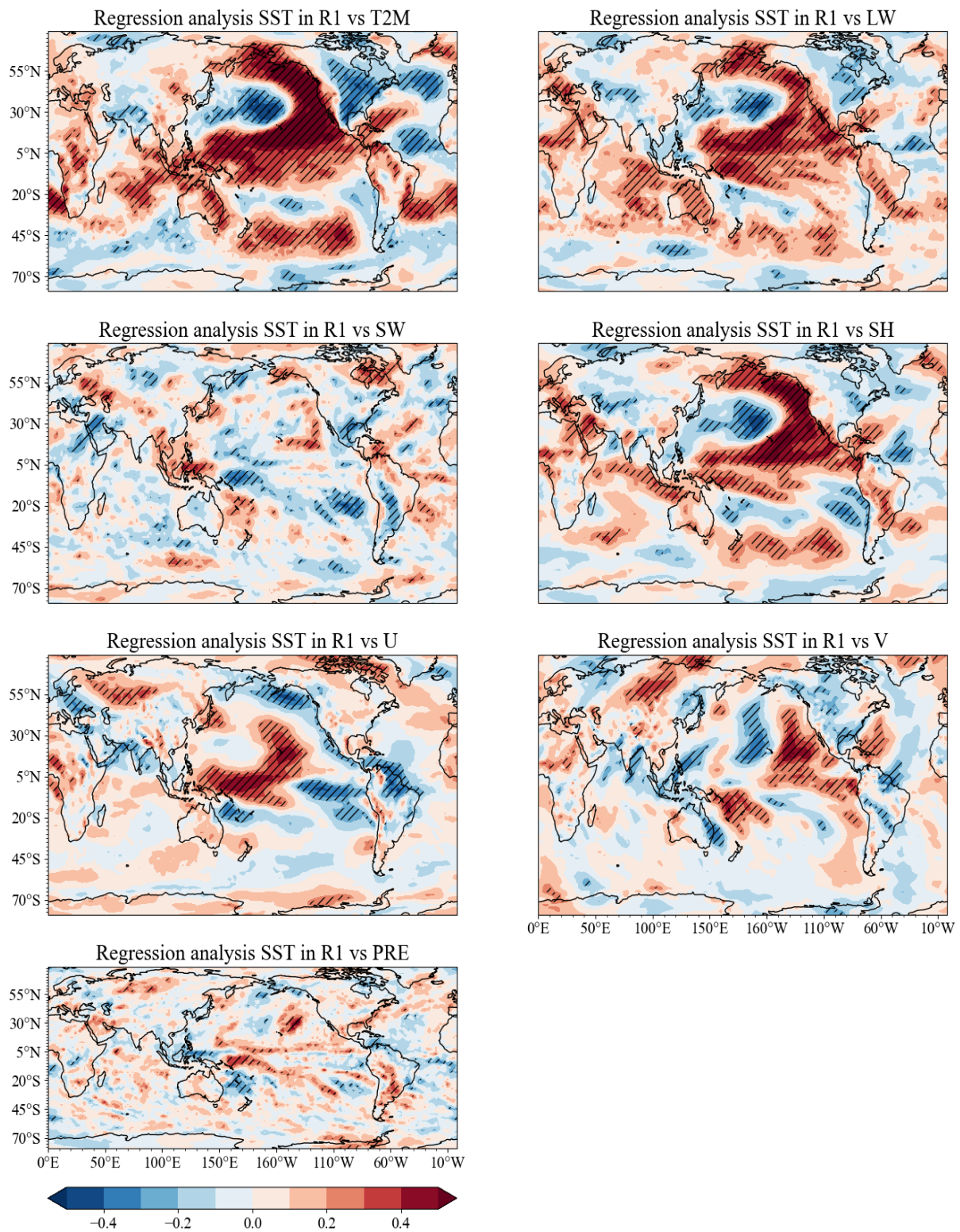


Fig. 4.1.18. Regression analysis between modeled monthly mean SST in region 1 and the monthly mean ERA5 AF data (From left to right, from top to bottom: T2M; LW; SW; SH; U, V, and PRE). The red areas indicate a positive correlation between the cost function and the respective AF, while the blue areas indicate a negative correlation. Darker shades represent stronger correlations. ‘/’ marks statistical significance.

Data period	Correlation with HadiSST
Annual mean SST from the previous year	0.56
Monthly mean SST from the previous year December	0.62
Seasonal mean SST from the previous year (OND)	0.52
Seasonal mean SST from the previous year (JAS)	0.44
Seasonal mean SST from the previous year (AMJ)	0.52
Seasonal mean SST from the previous year (JFM)	0.47
Seasonal mean SST from the previous year (OND) and the current year (JFM)	0.69

Table 4.1.1. Comparisons of the correlation between the annual mean SST and the monthly mean or seasonal mean SST occurring in different time lags in target region 1. SST data are based on HadiSST datasets from 1948 to 2022. The numbers shown in the table are correlation coefficients. OND represents October, November, and December; JAS represents July, August, and September; AMJ represents April, May, and June; JFM represents January, February, and March.

#### 4.1.6. NEP Monthly MHWs

Several studies have specifically analyzed the drivers of MHWs that occurred in February 2014 ([Bond et al., 2015](#); [Chen et al., 2023](#)). To compare the results obtained through the adjoint method with existing findings, additional adjoint experiments were conducted. In these experiments, the February monthly mean potential temperature in the upper 100 m for the year 2014 was set as the cost function. This approach allowed us to investigate the drivers of monthly MHWs more effectively. The same contribution analysis was also conducted to compare the contributions from the different AF ([Fig. 4.1.19](#)).

The contributions made by various AF to the 2014 February MHW yield findings consistent with those of Chen et al. ([2023](#)). Anomalous warm T2M plays a more significant role. While prior research, such as that by Bond et al. ([2015](#)), attributes the formation primarily to anomalous air-sea heat flux and horizontal advection resulting from reduced wind conditions, our study indicates that turbulent heat flux has a more pronounced impact on its formation. U may play a preconditioning role, as remote contributions were observed starting in September 2012. This phenomenon primarily influences subsurface warming (top panel in [Fig. 4.1.19](#)). The effect of horizontal winds on the surface MHW is negative (bottom panel in [Fig. 4.1.19](#)).

Overall, AF has a larger impact on surface warming than on subsurface warming due to the direct heat exchange. LW, T2M, and SH are the three dominant AF, which aligns with the annual MHW analysis above. The turbulent heat flux, in conjunction with SH and T2M, is the primary driver of both monthly and annual MHW in the NEP. The influence of LW can be attributed to cloud effects, according to the findings of Schmeisser et al. ([2019](#)). Additionally, the most sensitive period also aligns with the annual MHW analysis, indicating that atmospheric conditions began to influence the cost function starting in the winter of 2013.

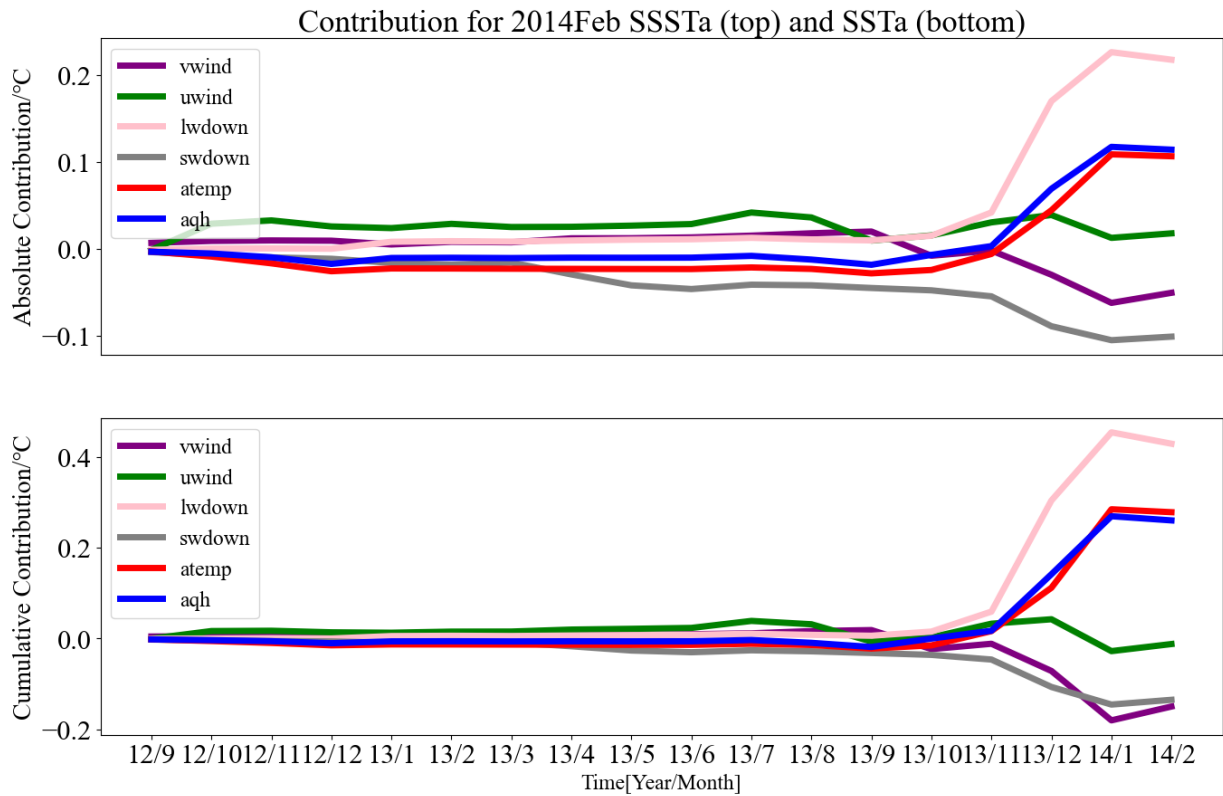


Fig. 4.1.19. Time evolution of the cumulative contributions to February SSTa (bottom) and February SSSTa (in the upper 100 m, top panel) in 2014 in region 1 by the different actual AF anomalies (purple: V; green: U; pink: LW; grey: SW; red: T2M; blue: SH).

In addition to focusing on interannual and monthly scales, the entire reconstruction (Fig. 4.1.15) can also be broken down for analysis at the seasonal scale, as illustrated in Fig. 4.1.20. This figure corresponds to contributions which were separated over eight seasons leading up to the target year. The results are consistent with the previous findings, indicating that the winter preceding the target year is critical for the initiation of an MHW event, especially when the mixed layer is typically deeper but becomes shallower under certain atmospheric conditions (e.g. high-pressure system). When examining contributions in the seasonal context, an unusual contribution from V was observed in the spring of 2019 (yellow lines). Typically, V contributes negatively in this region when turbulent heat flux contributions are significant, and its role in spring varies between the two target regions. This discrepancy warrants further investigation. In addition to contribution analysis, the seasonal mean potential temperature can be set as the cost function in future adjoint studies. Further refinement of the model setup will be necessary for conducting seasonal studies.

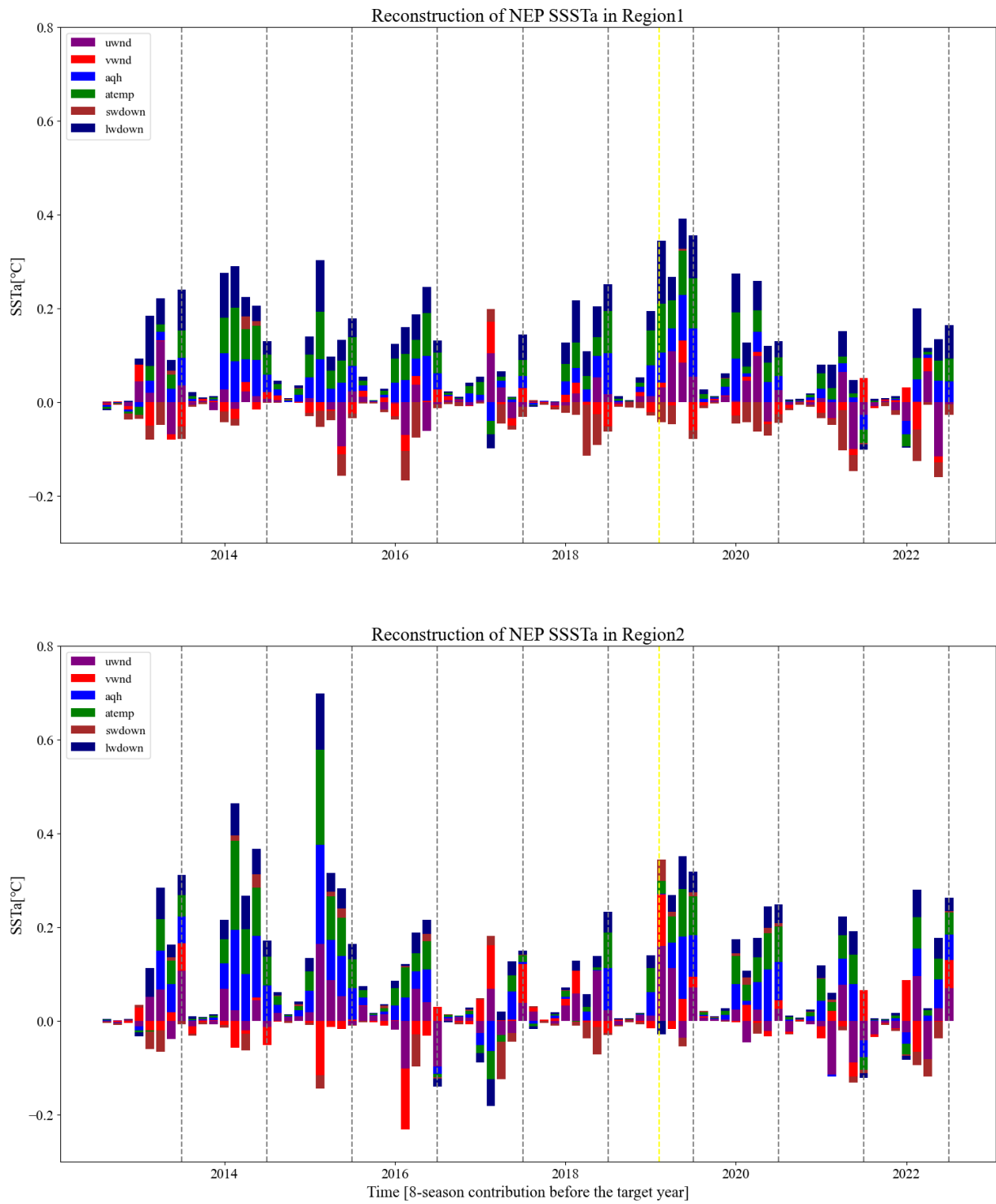


Fig. 4.1.20. Same as Fig. 4.1.15 but separating contributions over eight seasons prior to the target year. Vertical yellow lines show the spring of 2019.

#### 4.1.7. NEP MHW Discussion

For a complex nonlinear and coupled oceanic and atmospheric dynamical system, predicting when and where forcing anomalies might produce an extreme response poses a challenge in climate science. Acquiring improved insight into the temporal and spatial distributions of the systems' sensitivity to internal or external forcing anomalies or internal feedback mechanisms is therefore key to understanding the physical processes of the system required for improving and providing reliable forecasts.

This section showcased adjoint sensitivity computations as a tool for identifying physical pathways connecting NEP MHW within a target region to AF anomalies. Using the adjoint sensitivities identified AF as the main cause for MHW to occur, offering predictive potential 6-month in advance for annual MHW to occur. Utilizing atmospheric conditions from the total of 36 months preceding the target year demonstrates marginally improved predictive skill compared to persistence theory. Employing a 2-degree resolution model, 4 years of AF preceding the MHW proved to be reasonable for skillful reconstructing hindcasts of MHW occurrences, even in instances where nonlinear processes cannot be explicitly accounted for ([Zhang et al., 2009](#)). Furthermore, the implementation of real-time forecasting, utilizing optimal sensitivity fields and AF predictions (e.g. sourced from the European Center for Medium-Range Weather Forecasts) to do prediction of the next year, is deemed to be feasible and straightforward. The lead time can be further enhanced by applying more advanced AF forecasts.

In conclusion, T2M and SH are the dominant AF for NEP MHWs in the adjoint model setup. These findings are in agreement with prior studies that underscore the pivotal role of anomalous T2M and SH or air-sea heat flux in the formation of NEP MHWs ([Bond et al., 2015](#); [Chen et al., 2023](#); [Chen et al., 2021](#); [Ge et al., 2023](#); [Holbrook et al., 2019](#); [Zschenderlein et al., 2019](#)). Also, the sensitivity distribution confirms that the NEP MHWs are sensitive to atmospheric variability at the tail end of the Kuroshio Extension region ([Silva & Anderson, 2023](#)). Local anomalous air-sea heat flux is found to be the dominant driver for NEP MHW events to occur, induced by increased T2M and anomalous atmospheric moisture content. U is found to be not a dominant driver for extreme warming of the target region. Although it may contribute to warming in principle by altering surface turbulent heat fluxes, it appears to be more important during cooling events as it leads to a deepening of the surface

mixed layer. Furthermore, LW plays a significant role in this study, ranking as the third most important factor. This finding supports previous studies ([Kuroda & Setou, 2021](#); [Schmeisser et al., 2019](#); [Zhao & Yu, 2023](#)) that may challenge conventional beliefs.

It is notable that while results presented in this study are based on model runs forced with the ERA5 reanalysis, very similar results were obtained using the NCEP/NCAR reanalysis, making results independent of the specific reanalysis used.

As discussed by those previous authors ([Bond et al., 2015](#)), a potential mechanism for generating MHWs is that an anomalous high-pressure system resulting from the reduced Aleutian Low weakened the intensity of surface winds and increased the T2M. Therefore, heat losses were minimized, and the horizontal movement of cold water along with wind-driven vertical mixing in the ocean was weakened in the NEP region ([Chen et al., 2023](#)). The increased T2M is linked to an anomalous high-pressure system. Thereby it comes to another question: what are the drivers of the high-pressure system itself? This can be explored using a fully coupled atmosphere-ocean model in the future. Specifically, the strong MHW that occurred in 2020 was caused by below-normal latent heat release at the ocean surface ([Ge et al., 2023](#)). The findings in this study are consistent with these hypotheses, albeit the fact that mixed layer mixing and deepening processes are not considered explicitly.

A few investigations have proposed that tropical teleconnections may have a part in driving persistent MHW occurrences within the NEP region ([Capotondi et al., 2022](#); [Di Lorenzo & Mantua, 2016](#); [Xu et al., 2022](#)). In particular, Capotondi et al. (2022) find a strong connection between the NEP MHW development and evolution and a mode of variability at the decadal timescale (named North Pacific – Central Pacific mode), which may be related to the NPGO. Yang and Oh (2020) discussed the impact of ENSO and PDO on the SST variability of the NEP. While ENSO indeed exerts an impact on the NEP region, including heightened temperatures that surpass the norm ([Lin & Qian, 2019](#)), it does not appear to be the dominant driver for an extreme MHW event. This discrepancy may stem from the limitation of the ocean-only model or potential mismatches in temporal scales. Most of these studies emphasize that NEP MHWs tend to develop before El Niño events, and can help with the MHW persistence after the development. However, the exact role of ENSO, whether causal or just coincidental, is still under discussion. This study found that NPGO may be a more relevant index to NEP MHWs than other modes. The SSH fields, altered by wind-induced perturbations

similar to sensitivity variations, exhibit a response resembling the NPGO-like pattern to some extent. Overall, ocean circulation is less important compared to AF as during MHW years the ocean mostly acts by locally accumulating the heat entering through the surface.

A comprehensive exploration of all these mechanisms could be studied within a more complex atmosphere-ocean coupled system. Furthermore, the application of the T2M-based heatwave index within the adjoint methodology holds promise for conducting analyses of land heatwaves, potentially yielding enhanced insights into the underlying dynamics of all kinds of heatwave phenomena. It is notable, however, that the adjoint method has its own limitations. The adjoint model, based on a linear approximation of a forward model trajectory, is restricted to a time window where this linearity is valid. Some non-linear processes are neglected when conducting adjoint analysis. Therefore, it is of importance to check that linearity holds well for the research question of interest and test the validation of the adjoint model before any compelling conclusions can be confidently drawn.

#### **4.1.8. NEP MHW Summary**

In this section, to explore the potential mechanisms of the classic example of the MHW that occurred from 2014 to 2016, which spread across the NEP Ocean, the mean top 100 m potential temperature during different target years was set as the objective function, separately for the two target regions ( $145^{\circ} \sim 160^{\circ}\text{W}$ ,  $48^{\circ} \sim 56^{\circ}\text{N}$ ) and ( $130^{\circ} \sim 145^{\circ}\text{W}$ ,  $40^{\circ} \sim 48^{\circ}\text{N}$ ). Resulting adjoint sensitivities show that during MHW years, local turbulent surface heat flux is the dominant driver, with T2M, SH, and LW leading to up to 80% of the temperature anomaly of the NEP; during normal years this is only about 60%. In contrast, increased wind typically does not lead to an MHW occurrence as it is connected with the mixed layer deepening. This study finds the horizontal temperature advection, i.e., the impact of the basin-wide ocean circulation, to be less important during a MHW year; but it could act as a preconditioning of MHW through its role in climate oscillations. Contribution analysis shows that AF anomalies occurring within 3 months (from October to December) prior to an MHW year play a critical role in driving the MHW. The reconstruction using various sensitivity periods suggests that the leading 6-month atmospheric conditions should have potential predictive skills for the next year. Reconstruction that includes leading 36-month atmospheric conditions performs better than persistence.

## 4.2 Northwest Pacific Marine Heatwaves Mechanism

This section is designed to answer the second research question:

*Are MHW mechanisms in the NWP different from those in the NEP?*

*Can the results explain the unresolved residual terms in the previous study?*

This section has been prepared for publication after the submission of this thesis as:

*Xiaoxue Wang, Armin Köhl and Detlef Stammer. Potential Drivers of Northwest Pacific Marine Heatwaves Inferred from Adjoint Sensitivities.*

The format and contents have been slightly adjusted to suit this thesis.

All relevant references and additional information are compiled at the end of this thesis.

### 4.2.1. NWP MHW Research Region

While MHWs in the NEP have drawn significant attention due to their severe ecological consequences, the NWP exhibits MHWs of notably higher intensity, with SSTa reaching up to 5 ~ 6 °C ([Sen Gupta et al., 2020](#)). A striking example of an NWP MHW occurred during the summer of 2022 when extreme ocean surface temperature anomalies of approximately 5 ~ 6 °C above normal were recorded near the Kamchatka Peninsula (KP). According to the National Centers for Environmental Information ([NCEI, 2022b](#)), July 2022 was recorded as the sixth warmest July within the 143-year record (1880-2022). Under this warming condition, the record-breaking MHW around the KP persisted over the whole year with annual mean SST anomalies of 1.5 to 2 °C ([Fig. 4.2.1a](#)). Even after detrending to remove long-term warming influences, summer MHWs retained unprecedented duration and intensity. Typically, MHWs in this area last less than one month. However, in 2022, the MHW persisted for 12 months, with a particular instance reaching 14 months, making the longest duration since 1990 ([NOAA Physical Sciences Laboratory, 2024](#)). The extreme warming was not only confined to the surface but extended also the subsurface to depth levels of at least 100 m ([Figs. 4.2.1b - d](#)). The associated subsurface warming anomalies of about 0.9 °C were found to be nearly twice the magnitude of historical extremes ([Fig. 4.2.1c](#)). Subsurface MHWs have attracted increasing focus because of their ecological and climatic impacts ([Guo et al., 2024](#); [McAdam et al., 2023](#); [Sun et al., 2023](#)) but remain fewer studies in terms of physical drivers than surface MHWs. In this study, the term SSSTa actually refers to the near-surface temperature anomaly in the upper 100 m, including both surface and subsurface temperatures.

A heat budget analysis by Song et al. ([2024](#)) suggests that increased SW was the primary driver behind the July 2022 MHW in the NWP. This contrasts previous findings for NEP MHWs, for which local air-sea turbulent heat fluxes were reported as the primary atmospheric driver ([Bond et al., 2015](#); [Chen et al., 2023](#); [Chen et al., 2021](#); [Ge et al., 2023](#); [Holbrook et al., 2019](#)). In addition, momentum flux can also serve as a crucial driver depending on the specific region ([Holbrook et al., 2019](#)). Capotondi et al. ([2022](#)) demonstrated that while the duration of MHWs can be regulated by the timing of climate modes (e.g. El Niño-Southern Oscillation), their intensity is influenced by the local forcing.

Building on previous findings, the same adjoint sensitivity method used in the last section to study MHWs in the NEP is applied here, to study now mechanisms behind long-lasting

MHWs occurring in the NWP with emphasis on the 2022 annual mean subsurface extreme. As the study region, the area (R1)  $163^{\circ} \sim 169^{\circ}\text{E}$ ,  $52^{\circ} \sim 56^{\circ}\text{N}$ , 0-100 m (yellow box in Fig. 4.2.1), which was selected based on the warming pattern shown in Fig. 4.2.1. The subsurface MHWs are defined as periods when the potential temperature exceeds the monthly climatological 90th percentile based on monthly subsurface data from 2008 to 2022 following conventions. The warming trend is not removed, following the approach of Scannell et al. (2020), because the atmospheric conditions used to drive the model contain the influence of warming and it is not obvious how to remove the changes related to warming from the atmospheric conditions. It is noticeable that the selected region was also part of the region investigated by Song et al. (2024). The new findings about MHW forcing in the NWP will be compared with those obtained for the NEP.

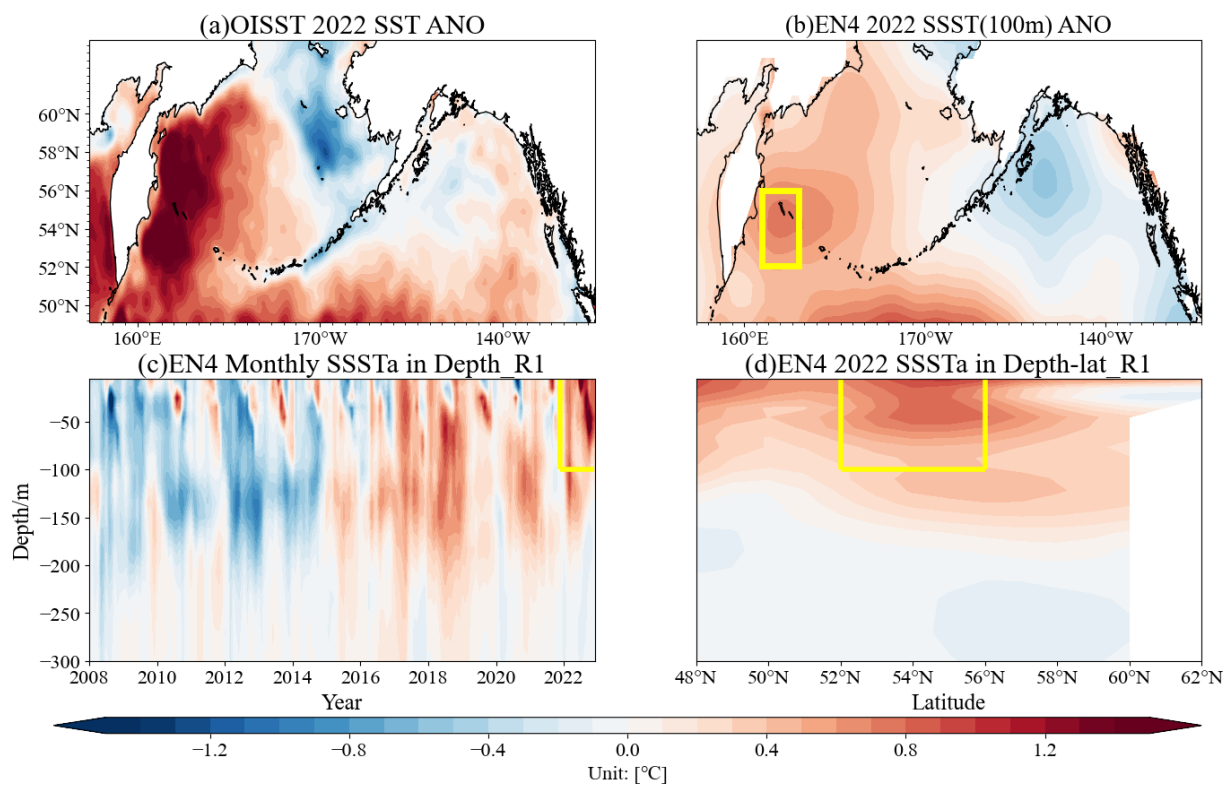


Fig. 4.2.1. (a) Annual mean OISST (Huang et al., 2021) SSTa and (b) EN4 (Good et al., 2013) SSSTa (in the upper 100 m) of 2022 relative to the average over the period 2008-2022. (c) Depth-year cross-section of monthly mean SSSTa and (d) Depth-latitude cross-section of the annual mean SSSTa for 2022, based on the EN4 dataset. Yellow boxes show our study area (R1:  $163^{\circ} \sim 169^{\circ}\text{E}$ ,  $52^{\circ} \sim 56^{\circ}\text{N}$ , 0-100 m) and the vertical yellow line in (c) show our target year 2022.

### 4.2.2. NWP MHW Model Set-up

In this NWP section, experiments were primarily conducted over the past 15 years, from 2008 to 2022, using the same model configuration as in the first section. As such, the AF anomalies are determined in relation to the average values obtained from the period from 2008 to 2022.

To evaluate the model's performance in simulating near-surface temperature anomalies in the NWP, time series of annual mean potential temperature anomalies averaged over the top 100 m in the target region are shown in [Fig. 4.2.2](#) for the period 2008 to 2022. These anomalies can be compared with observations based on EN4 ([Good et al., 2013](#)) upper-ocean temperature estimates and ORAS5 ([Climate Data Store, 2025](#)) global ocean reanalysis data which incorporate satellite data as part of its assimilation process. During the shown period, SSSTa shows a strong warming trend in the target region. EN4's reliance on sparse in-situ data near the KP limits its capacity to resolve extreme events in detail, thereby underestimating the peak temperatures suggested by SST observations. As highlighted by Zhang et al. ([2024b](#)), there is a large spread also in MHW assessments across various SST products in Asia and the Indo-Pacific region. Therefore, it is important to employ multiple datasets to comprehensively evaluate extreme events and reduce uncertainty.

A visual comparison suggests that the model successfully reproduces the annual warming trend of the upper 100 m, despite its limited ability to resolve finer spatial patterns ([Fig. 4.2.2](#)). The simulated annual mean SSSTa exhibit statistically significant correlations with observational datasets against EN4 (solid orange line, 0.83) and ORAS5 (solid red line, 0.91). In particular, the model successfully simulates the pronounced warming observed in 2022. The mean potential temperature anomalies averaged over the upper 100 m (SSSTa) from the model outputs (e.g. R1: 0.82 °C in 2022) remain comparable to the EN4 observations (e.g. R1: 0.64 °C in 2022). While the model underestimates temperatures in 2016 and overestimates over the past five years, it reproduces the triphasic (high-low-high) temperature distribution pattern observed in EN4 observational data between 2018 and 2022.

Given this alignment, the year 2022 is selected as the main target MHW year for analyzing the primary drivers of the record-breaking MHWs. Additionally, the year 2018 will be considered as a reference year for comparative analysis, enabling an investigation into potential differences between the MHW year and non-MHW year. The cost function in this section is

defined as the temperature field in the upper 100 m of the target region ( $163^{\circ} \sim 169^{\circ}\text{E}$ ,  $52^{\circ} \sim 56^{\circ}\text{N}$ ), averaged over a one-year period (Eq. 3.6) and one-month period for monthly MHW cases. The definition is consistent with the cost function used in the NEP. The period of the cost function is selected without considering detrending, as the AF utilized includes inherent trends. Contribution analysis (Eq. 3.7) and perturbation experiments (Eq. 3.13) are also applied subsequently to scale the contribution of different AF to the total variation of SSSTs in the NWP.

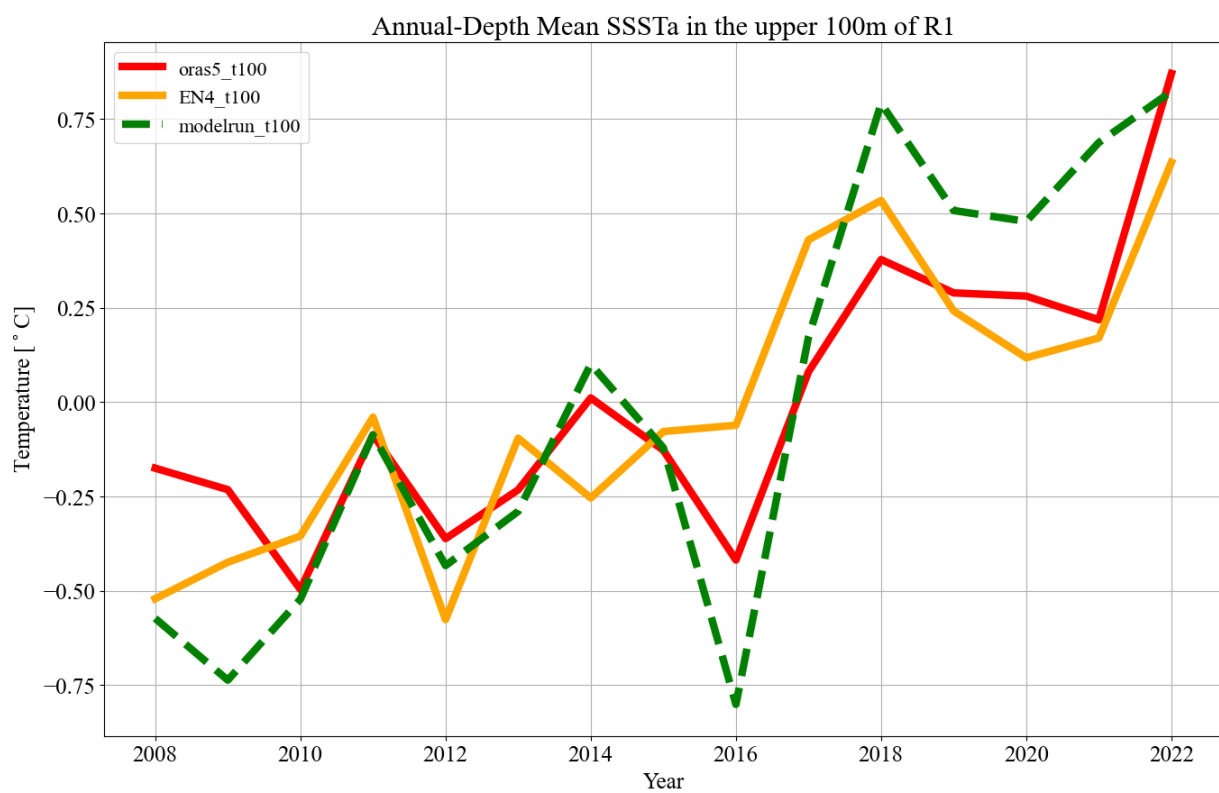


Fig. 4.2.2. Time series of annual mean SSSTa (averaged over the upper 100 m) from 2008 to 2022 in R1 based on different datasets. The dashed green line represents SSSTa from ERA5 forced forward model outputs, the solid red line represents ORAS5 fields and the orange line represents EN4 observations. The correlation coefficient associated with the model and EN4 data is 0.83, while the correlation coefficient associated with the model and the ORAS5 dataset is 0.91.

### 4.2.3. NWP MHW Sensitivities

#### *a. Adjoint Sensitivity Pattern*

The sensitivity of ocean conditions to AF was assessed through two adjoint experiments, using annual mean SSST (Eq. 3.6) as the cost function for the MHW year 2022 (main experiment) and 2018 (reference experiment). Shown in Fig. 4.2.3 are the resulting SW sensitivity fields from both experiments. Because the sensitivity fields related to heat flux components are all consistently positive throughout the year, only the annual mean sensitivities are displayed. Amplitudes below a certain threshold (Veneziani et al., 2009) are excluded from the figure to highlight the significant signals. Positive sensitivity values (purple shading) indicate that any positive perturbation will enhance the annual mean potential temperature in the target region. It is noted that other heat flux components (T2M, SH, LW) are not shown as they exhibited spatially consistent patterns.

Fig. 4.2.3 reveals that surface heat flux primarily contributes locally to warming during each target year, with peak sensitivities occurring in both cases during the target year itself and -1yr. The larger sensitivity of the MHW year to surface heat flux ( $0.00037 \text{ }^\circ\text{C}/\text{W}/\text{m}^2$ ) compared to the reference year ( $0.00033 \text{ }^\circ\text{C}/\text{W}/\text{m}^2$ ) indicates an important role of heat flux terms in influencing NWP warming. Sensitivities decrease for time periods prior to -1yr (Figs. 4.2.3e-h). Notably in the Western Bering Sea (WBS) region, the 2018 experiment (maximum sensitivity  $0.000077 \text{ }^\circ\text{C}/\text{W}/\text{m}^2$ ) exhibits higher sensitivity compared to the 2022 experiment (maximum sensitivity  $0.000057 \text{ }^\circ\text{C}/\text{W}/\text{m}^2$ ) before -2yr, particularly in the region to the right of the target box (Figs. 4.2.3f, h). The presence of a relatively higher sensitivity center is also observed in experiments from other reference years (e.g. maximum sensitivity  $0.0001 \text{ }^\circ\text{C}/\text{W}/\text{m}^2$  for 2014 and  $0.000074 \text{ }^\circ\text{C}/\text{W}/\text{m}^2$  for 2015). However, the sensitivity observed before -2yr is generally too small to cause a significant change when compared to the local effects during the period near the target year. These findings are different from the distributions of heat flux components associated with NEP MHWs, where for individual heat flux components, the spatial sensitivity distribution remains consistent across different years. This allows for the use of a fixed sensitivity field to reconstruct MHW in the NEP, while employing the 2018 sensitivity field to reconstruct 2022 MHW in the NWP will lead to an underestimation of the contributions, which will be discussed later. Overall, near-surface temperature changes in the

target box are sensitive to the heat flux conditions in the local area and the WBS, with the MHW year showing a larger sensitivity to local heat flux exchanges rather than remote effects.

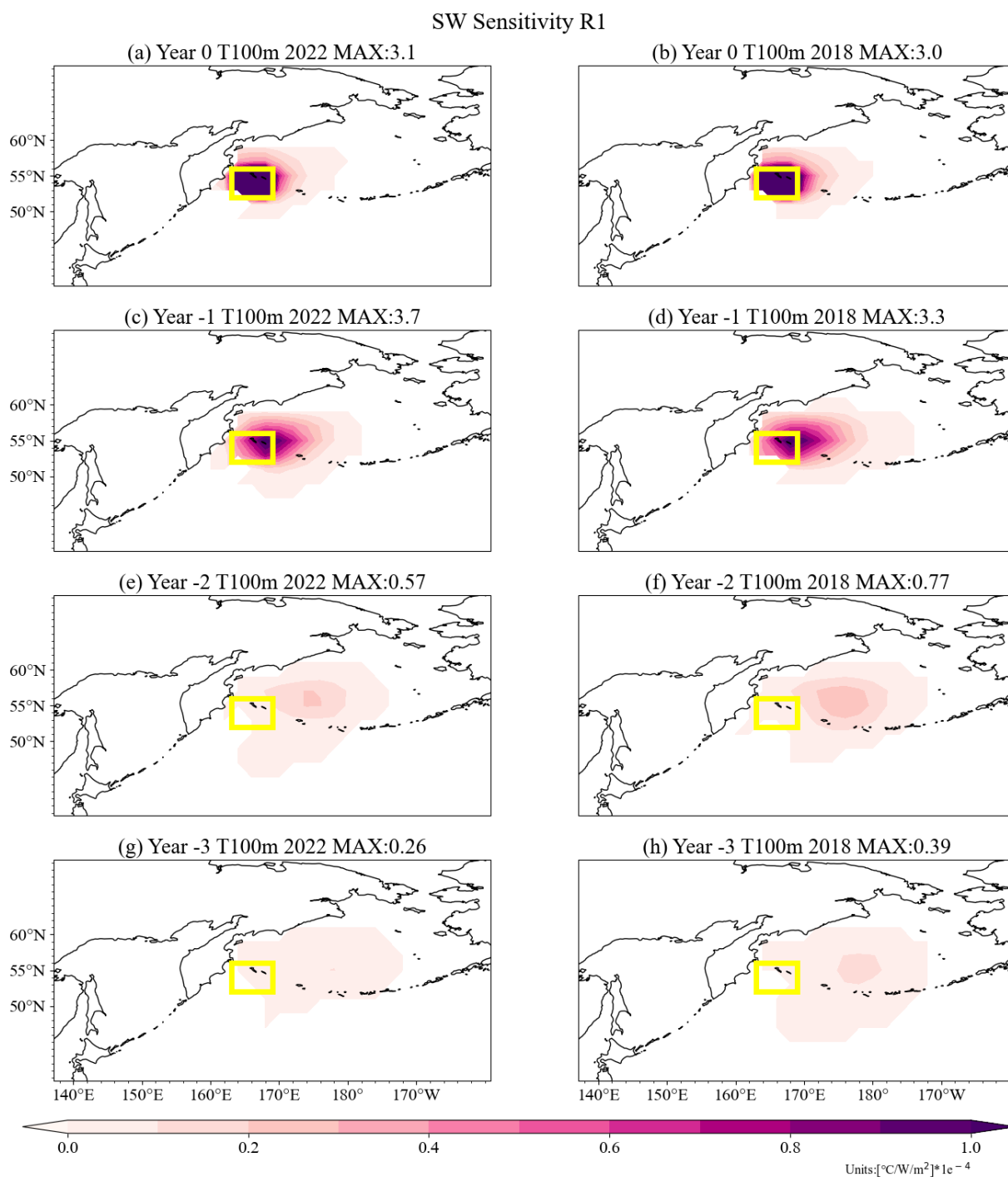


Fig. 4.2.3. Evolution of the adjoint sensitivity of annual mean SSST in 2022 (left panel) and in 2018 (right panel) with respect to SW for R1 (from top to bottom backward in time). The yellow box indicates the target research region. To compare the magnitude of two years, the maximum values of sensitivities are shown in the subtitle of each panel.

To further investigate the most sensitive period, the time evolution of the maximum sensitivity with respect to T2M is presented in [Fig. 4.2.4](#). The most striking difference between the MHW year 2022 (blue line in [Fig. 4.2.4a](#)) and reference year 2018 (green line in [Fig. 4.2.4a](#)) is the nearly tripled sensitivity of 2022-MHW to T2M during the preceding winter. Additionally, while the annual MHW shows increased sensitivity to T2M in the summertime, this sensitivity is only half the size compared to the preceding winter, indicating the significant role of winter ocean memory. This is also consistent with the SW sensitivity shown in [Fig. 4.2.3](#), where maximum sensitivity occurred during -1yr ([Fig. 4.2.3a](#) vs [Fig. 4.2.3c](#)). Furthermore, as previously discussed, the sensitivity of 2018 prior to -1yr is larger than that of 2022 (as indicated by the green line at time point -1/1, -2/2), although the overall magnitude remains substantially lower.

The year 2022 is identified as the MHW year because each month is identified as MHW month according to the definition. However, the summer MHW in 2022 was observed to be more intense than the winter MHW ([Fig. 4.2.1c](#)), and some propagation signal was detected from the surface to the subsurface, particularly in the late summer. To investigate the underlying different sensitivities in terms of different seasons, the sensitivities of both SST and SSST in July and December with respect to AF were further analyzed. The most sensitive areas in terms of monthly MHWs remain consistent with those presented in [Fig. 4.2.3](#). However, there are variations in the periods of relatively higher sensitivity. Therefore, shown here are additionally the maximum sensitivity of monthly mean SST and monthly mean SSST in the respective region with respect to the T2M for July and December in 2022 and in 2018 as examples ([Figs. 4.2.4b, c](#)). Please note that for convenience, Jul-MHW and Dec-MHW refer to monthly MHW, while 2022-MHW denotes annual MHW.

To understand why July 2022 was particularly extreme, it is first compared to July 2018 (orange line in [Fig. 4.2.4b](#)), noting July 2022 exhibits twice the maximum sensitivity to T2M (red line in [Fig. 4.2.4b](#)). This increased sensitivity is evident in two distinct time periods: one is the immediate time effect, during which the ocean's response to sensible heat flux was significantly stronger in July 2022. The other way is the delayed effect from the preceding winter, whereby higher-than-normal winter T2M caused subsurface water to become warmer than average by reducing surface cooling and facilitating the mixing of residual heat from the surface into the subsurface. This warmer water, which was stored below the winter mixed layer

during the previous winter and trapped during the summer due to strong stratification, returned to the upper ocean in the following winter, creating a ‘re-emergence’ effect. According to the sensitivity distribution ([Fig. 4.2.3](#)), the region is susceptible to anomalous warming from regions west of the target area, indicating a certain degree of heat propagation. Furthermore, the short-term effect in July is consistently stronger than the delayed effect from the preceding winter. Interestingly, the magnitude of sensitivity with respect to winter T2M in relation to July-MHW is comparable to that of annual MHW ([Fig. 4.2.4a](#)). In other words, the winter preconditions leading to both monthly MHW and annual MHW are similar; however, the July-MHW is more reliant on the summer heat flux.

Surface MHWs and subsurface MHWs also respond differently to the winter preconditions. In MHW year 2022, SSTa were primarily susceptible to immediate T2M anomalies in their concurrent month, with minimal influence from prior winter conditions (dashed lines in [Fig. 4.2.4c](#)). In contrast, the SSSTa exhibited strong ties to T2M from past winters – even as far back as winter 2020 – due to the ocean’s multi-year thermal memory, where heat trapped in the deeper layer during winter mixing is capped by the summer stratification (solid lines in [Fig. 4.2.4c](#)). Therefore, the role of ocean memory should receive greater attention when analyzing subsurface events.

Overall, monthly MHWs and surface MHWs are predominantly driven by the concurrent month with significant contributions from the previous winter only if capped layers are included in the analysis. In contrast, annual subsurface MHWs are heavily influenced by heat accumulation from prior winters, with a more integrating effect over the rest of the year.

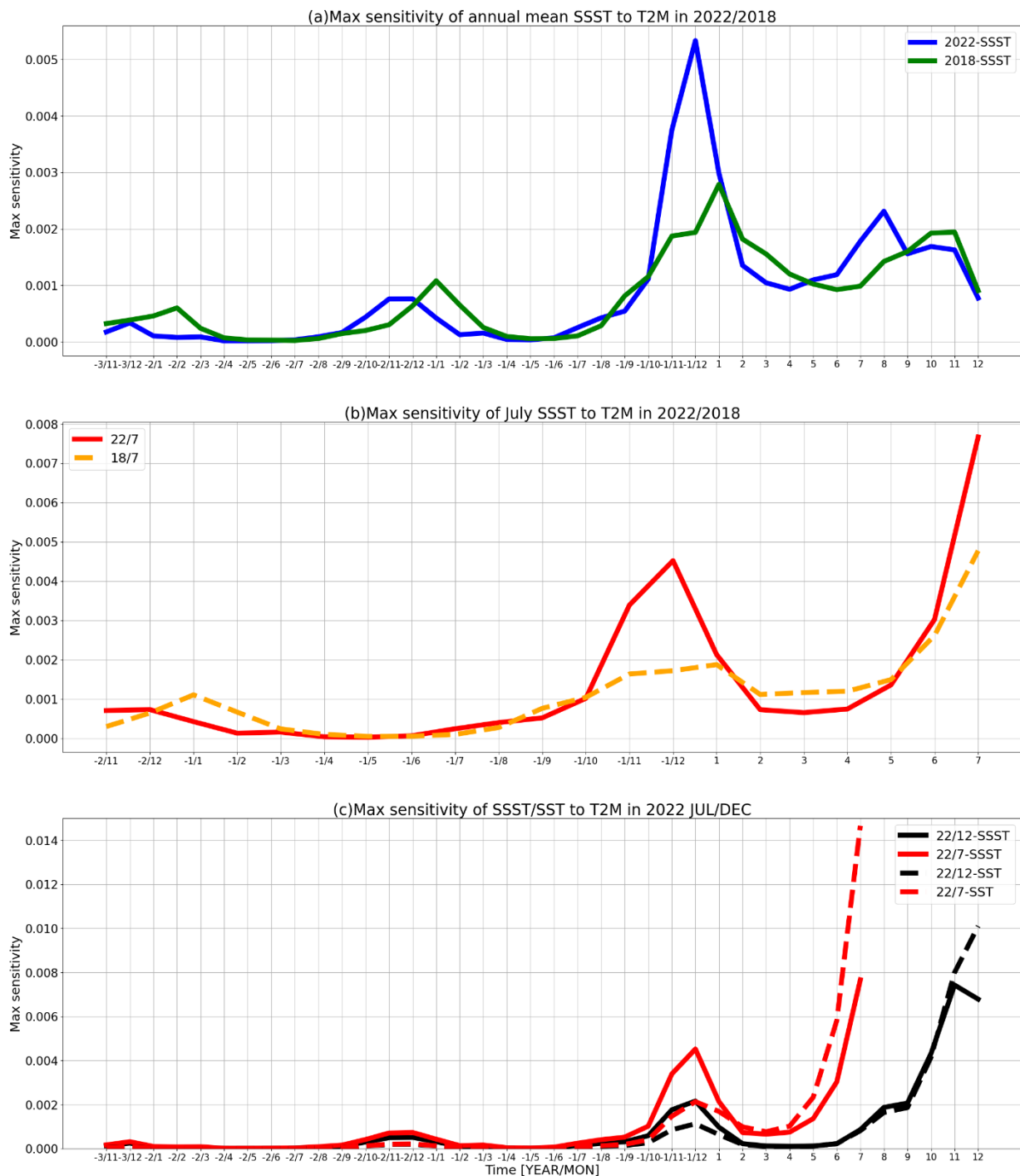


Fig. 4.2.4. The time evolution of the maximum sensitivity of the cost function with respect to T2M. (a) The cost function is annual subsurface MHW (SSST) in 2022 (blue) and 2018 (green); (b) the cost function is monthly subsurface MHW (SSST) in July 2022 (red) and 2018 (orange); (c) the cost function is July surface MHW (SST, dashed red), July subsurface MHW (SSST, solid red), December surface MHW (SST, dashed black) and December subsurface MHW (SSST, solid black) in 2022. For instance, the time point ‘-3/12’ refers to December occurring three years prior to the year of the cost function.

Besides surface heat flux, momentum flux also plays a role in shaping SSST anomalies of an MHW. However, sensitivities to horizontal winds exhibit significant variability over time across different years, and presenting the annual mean may obscure some of the propagation signals, rendering annual mean sensitivity meaningless. Shown in [Figs 4.2.5, 4.2.6](#) are therefore monthly mean sensitivities with respect to V and U, respectively. The red shows an increase in the cost function corresponding to an enhanced westerly/southerly wind anomaly or a reduced easterly/northerly wind anomaly.

For meridional winds, both the 2018 and 2022 target years exhibit a tripolar sensitivity pattern east of the target area between -48mon and -12mon, marked by alternating negative-positive-negative signals. This spatially oscillating wave-like pattern is likely generated by upwelling and downwelling, which result in vorticity anomalies that can propagate slowly westward as Rossby waves. The key difference between the two years is that the 2022-experiment displays stronger positive sensitivity ( $0.00182 \text{ }^{\circ}\text{C}/\text{m}/\text{s}$ ) within the target region and extends to the WBS, occurring at lead 12month ([Fig. 4.2.5a](#)). In contrast, the 2018-experiment is mainly influenced by locally negative sensitivity throughout the entire period, with a significantly lower value ( $-0.0021 \text{ }^{\circ}\text{C}/\text{m}/\text{s}$ ) also occurring at lead 12 month ([Fig. 4.2.5b](#)). Overall, the reference year 2018 is more sensitive to V, while MHW year 2022 demonstrates relatively weaker sensitivity to V at almost all times except for -12mon. This means that only increased southerly winds or decreased northerly winds occurring in -12mon are likely important factors contributing to MHWs.

Zonal wind sensitivities reveal obvious interannual contrasts between two target years which behave differently from V. In 2022, there was dominant positive sensitivity along the coast around -12mon, with both broader distribution and a higher magnitude ( $0.00125 \text{ }^{\circ}\text{C}/\text{m}/\text{s}$ ) compared to negative sensitivity ( $-0.0009 \text{ }^{\circ}\text{C}/\text{m}/\text{s}$ , [Fig. 4.2.6a](#)). This indicates that enhanced westerly winds may significantly contribute to MHW. When the westerly winds strengthen with a latitudinal gradient, they can induce Ekman pumping and suction in the target region, thereby bringing up the heat stored below the mixed layer and redistributing it, as discussed in [Fig. 4.2.4](#). Conversely, the 2018-experiment exhibits comparable values of negative sensitivity within the target region and positive sensitivity to the south of the defined area ([Fig. 4.2.6b](#)), indicating a localized circulation pattern around the target region. Prior to -24mon, tripolar sensitivity distributions emerge in both experiments, with 2018 demonstrating stronger positive

sensitivity than 2022, especially in the WBS region. These tripolar distributions are likely linked to the cooler Bering Sea Gyre to the north and the warmer Western Subarctic Gyre to the south of the Aleutian Islands. A propagation signal is observed from negative sensitivity in both cases, particularly evident in -24mon of the 2022-MHW. This suggests that the enhanced easterly winds can also contribute to warming in the target region through their propagating effect.

Overall, the horizontal wind sensitivity fields indicate that the most sensitive regions for driving changes in SSST in the target are found in the WBS region and the region south of the Aleutian Islands. Additionally, the 2022-MHW is less influenced by remote V but is to some extent sensitive to the enhanced remote easterly winds. Both locally increased westerly and southerly winds in the target year could be a driver for subsequent MHWs through Ekman upwelling or downwelling. The marked interannual variability in sensitivity pattern underscores the dependence of MHW drivers on the background ocean state, which is a distinction from the sensitivity of the NEP region to the ocean state.

VWND Sensitivity R1

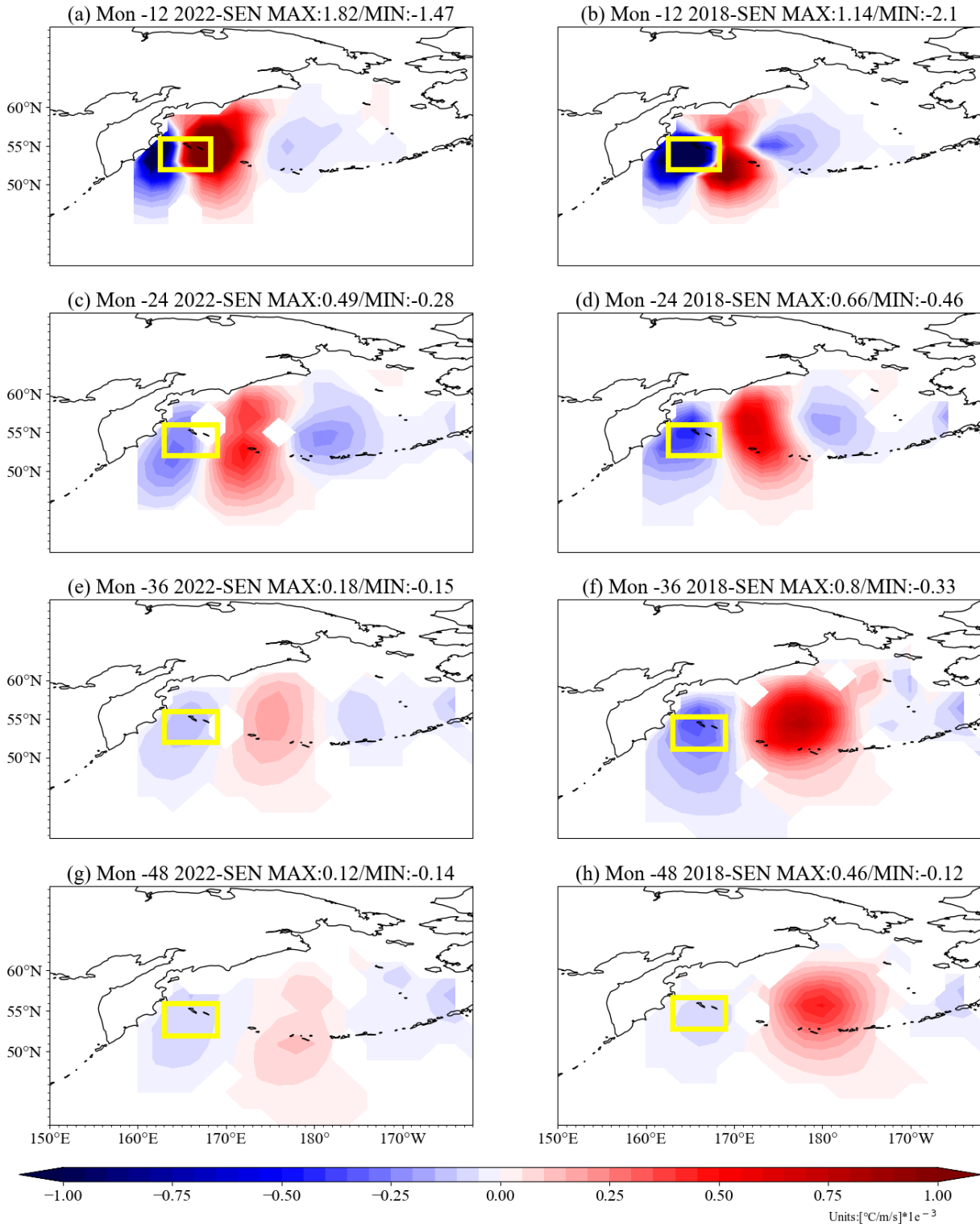


Fig. 4.2.5. Same as Fig. 4.2.3, but with respect to V at certain months (a, b: -12mon; c, d: -24mon; e, f: -36mon; g, h: -48mon). To compare the magnitude of two years, the maximum and minimum values of sensitivities are shown in the subtitle of each panel.

UWND Sensitivity R1

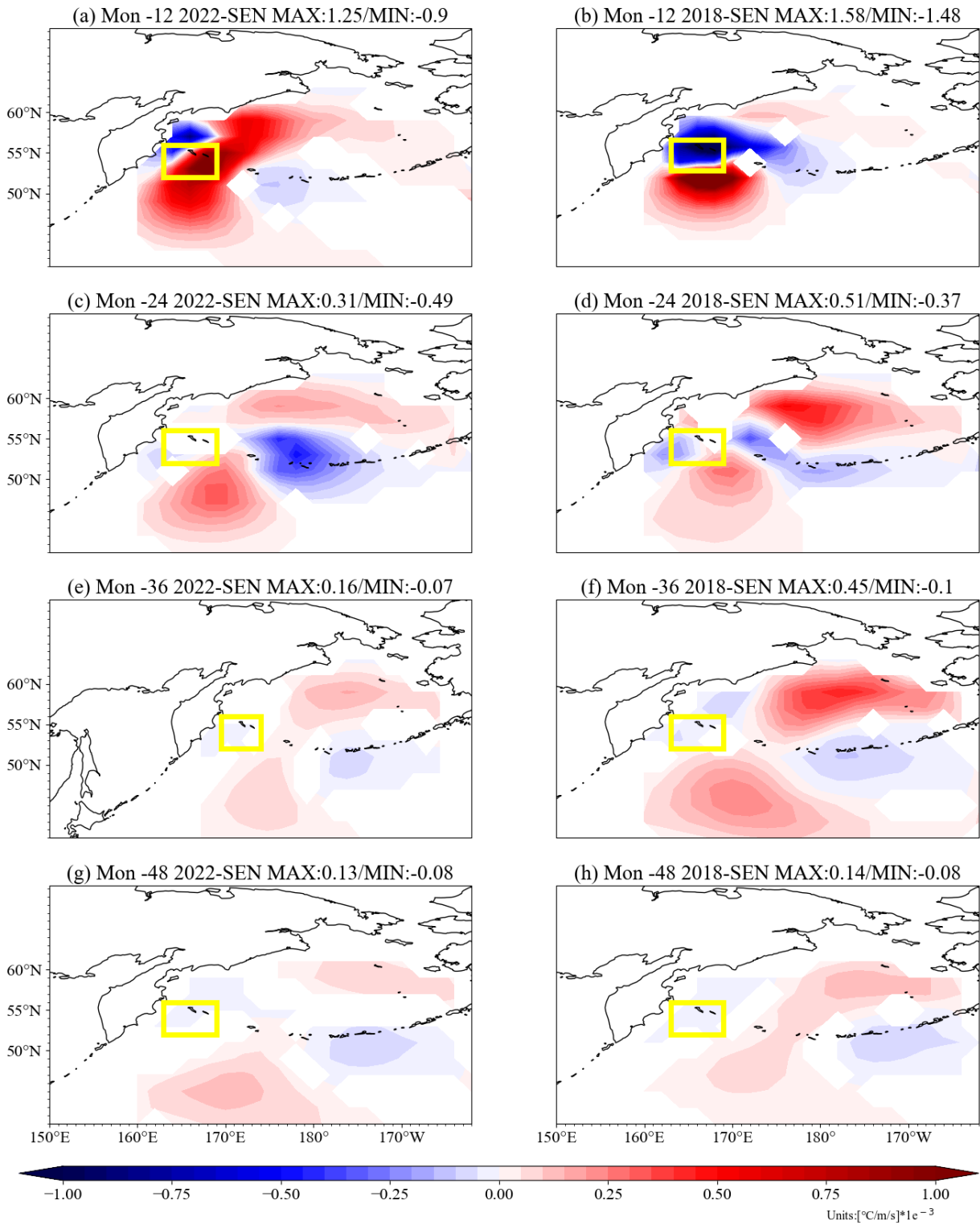


Fig. 4.2.6. Same as Fig. 4.2.5, but with respect to U at certain months.

### *b. AF Contribution Pattern*

While the above sensitivity pattern identifies the most sensitive regions and periods for generating temperature anomalies in the target region, quantifying the relative roles of individual AF based on only the adjoint sensitivities is not possible for concrete events. To address this question, a contributions analysis is used to standardize the relative effects of AF anomalies and to facilitate a quantitative comparison. Using [Eq. 3.7](#), adjoint sensitivity fields are multiplied with the actual AF anomalies to estimate temperature changes attributable to each AF. This approach allows the assessment of contributions across different months and years, facilitating the identification of the most relevant periods, areas, and the key drivers responsible for generating MHWs. Moreover, the resulting contribution pattern highlights the regions with the largest influence on the cost function.

For the adjoint experiment with the 2022 annual mean SSST as the cost function, the backward run is conducted over a 15-year period, running from 2022 to 2008. As sensitivities rapidly decline with integration time, only the contribution from the leading 3 years and their cumulative contribution in R1 are contributing substantially and are displayed in [Fig. 4.2.7](#). The figure illustrates the annual spatial evolution from aggregated monthly contributions ([Eq. 3.8](#)), with percentage contributions indicated in the titles, while [Fig. 4.2.8](#) presents the monthly temporal evolution from spatial aggregation ([Eq. 3.9](#)). Red and blue shading represent warming and cooling contributions, respectively. Discrepancies between summed annual contributions (first three columns) and cumulative totals (last column) arise from the influences of the year preceding the -2yr, which are excluded from the figure for clarity. Contributions prior to -1yr are negligible for all forcing except horizontal wind. The contribution of precipitation for 2022 (less than 1%) is omitted due to minimal impact.

The contribution analysis reveals that with a total contribution of 29% to the warming event in R1, the horizontal wind is the primary contributor with the U contributing 14% and the V 15%. T2M directly follows accounting for approximately 28% of the total warming, with its largest impact occurring between -1yr and 0yr, and nearly one-fourth of this contribution derived from the winter preceding the target year. Contribution from SW, and LW closely follow at levels of about 18% and 15%, respectively. The combined contributions from six AF (SW, LW, U, V, T2M, and SH) account for about 80% of the total between -1yr (2021) and 0yr (2022). During the target year, U has a negative local impact but a positive influence east of the

target area. Positive contribution induced by enhanced westerly winds from the WBS region dominates at -1yr. Overall, there is a net positive contribution (green line in [Fig. 4.2.8a](#)) from both remote and local effects by U.

V primarily contributes during the year preceding the target year (-1yr), exhibiting a positive influence specifically to the east of the target region. The total wind contribution of 30% highlights the importance of induced processes most likely related to wave propagation of upwelling and downwelling signals in the NWP, contrasting with the NEP MHWs and contradicting some previous findings in NWP.

Although the cost function is defined using annual-mean and volume-mean potential temperature, which is a single numerical value, the total contribution map ([Fig. 4.2.7-27](#)) can still identify when and where remote contributions from horizontal winds occur. This is due to the ocean-physics-based nature of the adjoint method, which allows for an accurate representation of linear dynamical ocean processes across different years. For instance, the reference year 2018 identifies distinct mechanisms influencing cost function variations ([Fig. 4.2.8b](#)), with U significantly driving warming, while V and SW suppress it, highlighting a key difference compared to 2022. These findings differ from the results by Song et al. ([2024](#)), who indicated SW as the key driver of the 2022 July warming. For the annual mean event, winds play the dominant role followed by T2M explaining together about 2/3 of the signal only followed by SW in the third place. The key difference is the different time scales of the event, monthly versus annual, and that the subsurface warming up to 100 m depth was also considered. LW consistently contributes positively to warming in both years, supporting the findings of Zhao & Yu ([2023](#)) regarding the significance of LW.

The forcing contributions over the year can be further separated into different seasons, allowing for quantification of contributions during specific periods ([Fig. 4.2.8c](#)). As previously discussed, U (green line) exhibits a negative contribution in the target year. In contrast, prior to the target year, U consistently provides a positive contribution, beginning three years before the target year, with a significant peak in positive contribution observed during the two winters prior to the target years. V (purple line) has a less pronounced remote influence compared to U. Specifically, V contributes positively only from the summer of -1yr to the spring of the target year. T2M (red line) and SH (blue line) exhibit similar patterns, beginning their contributions at the same time as V. However, T2M contributes twice as much as SH during this period. The

staggered influence of SW (grey line) and LW (pink line) reflects their distinct seasonal roles in modulating ocean heat budget. SW begins contributing to warming from the spring of -1yr and reaches its peak during the two summers of the preceding two years (2021 and 2022). In contrast, the contribution of LW peaks between these two summers is likely due to the increased cloud cover during the winter months based on total cloud cover data from ERA-5 reanalysis.

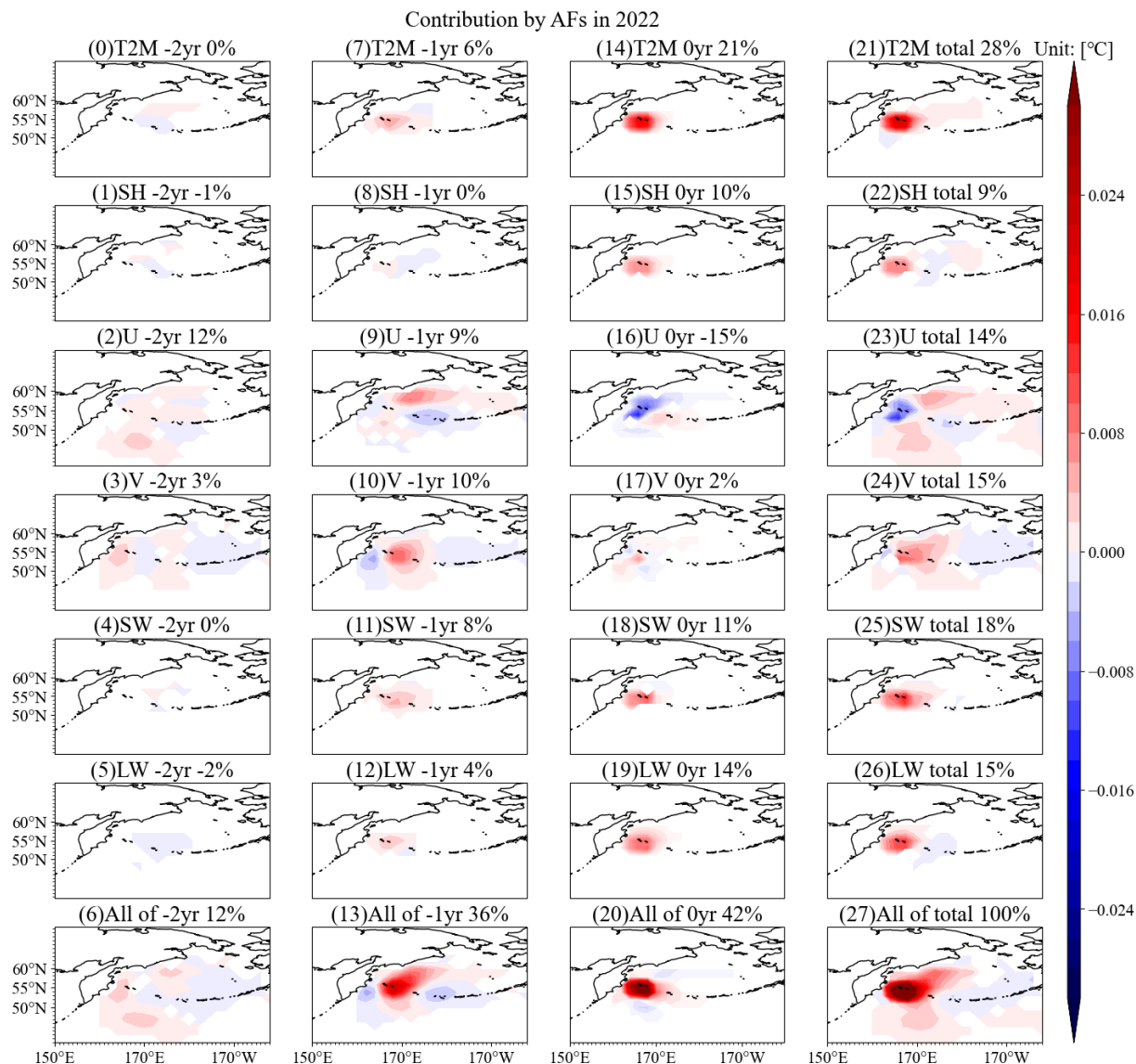


Fig. 4.2.7. Evolution of the annual contribution to 2022 warming calculated by Eq. 3.8 (the contribution is summed annually in time) with respect to different AF (from top to bottom: T2M, SH, U, V, SW, LW, and total) for R1 (from left to right, forward in time, the last column shows the total of 3 years). The numbers in the subtitle show the percentage contribution by each AF. The red shows a positive contribution (warming) and the blue shows a negative contribution (cooling).

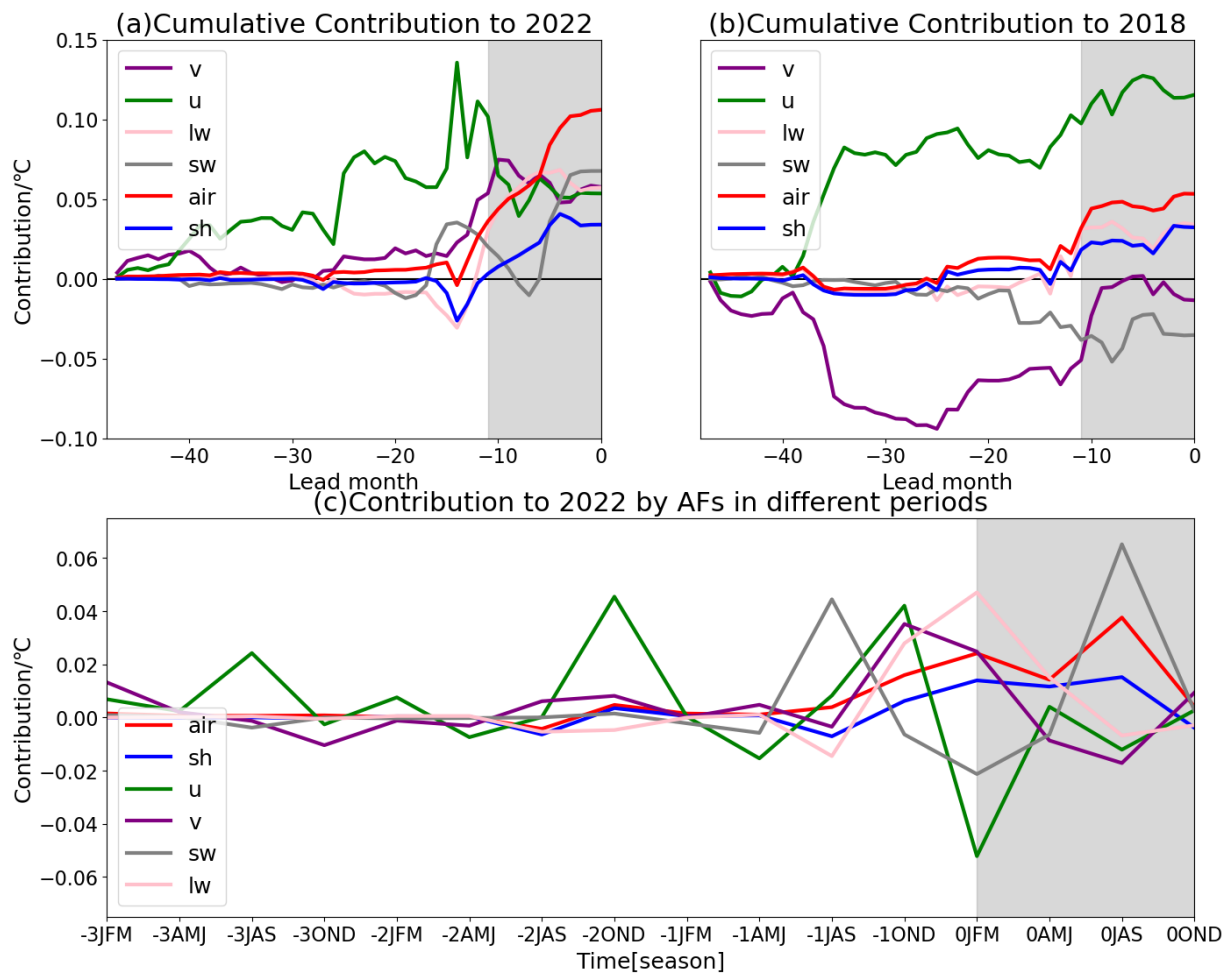


Fig. 4.2.8. Temporal evolution of the monthly cumulative contribution to (a) 2022 warming and (b) 2018 warming calculated by Eq. 3.9 (the contribution is summed in space) for R1. Different colors indicate different AF (purple: V; green: U; pink: LW; grey: SW; red: T2M; blue: SH). (c) As shown in (a) and (b), but the contributions are represented as absolute values accumulated in a seasonal context. For instance, time span -3JFM corresponds to the contributions made during the first three months (January, February, and March) of the -3yr, and time span 0OND corresponds to the contributions made during the last three months (October, November, and December) in the target year 2022 (filled by grey). The black line indicates the baseline zero.

SSST anomalies in 2022 can be reconstructed by aggregating all the cumulative contributions of all AF (Eq. 3.12). The total contribution of R1 is 0.38 °C in total and 0.3 °C for the leading 2-year (including 2021 and 2022). This reconstructed contribution appears underestimated compared to the forward run (0.82 °C, Fig. 4.2.2). However, for NEP MHW cases, reconstructions demonstrate better accuracy with minimal discrepancies (Fig. 4.1.15), as non-linear processes and mixing had limited impact on the NEP MHW. In contrast, NWP mechanisms are more complicated, with varying sensitivity fields across target years (Figs.

[4.2.3](#), [4.2.5-4.2.6](#)). To further validate the contribution analysis, reconstructed data were established from 2011 to 2022 utilizing sensitivity fields from various adjoint runs ([Fig. 4.2.9](#)), excluding precipitation due to its minimal impact. Throughout the reconstruction period, V emerged as a significant driver of the 2016-2017 cooling event, a role that also differs from that observed in the NEP, where U serves as the primary of cooling. Additionally, SH is identified as the least impactful AF in shaping the temperature distribution within the NWP target region. Notably, 2022 is the only year in which all AF contributed positively, with T2M contributing much greater than other years.

The linearized reconstruction exhibits significant discrepancies when compared to the forward run (solid orange line). Two possible explanations for this discrepancy: one is the linear nature of the adjoint model, which cannot effectively capture nonlinear processes; the other one is the exclusion of vertical mixing processes in the backward run due to stability concerns with the adjoint code for KPP mixed layer parameterization. This observation indirectly reflects that mixing may play a crucial role in the selected region within the NWP, especially in the recent several years. An additional reconstruction of the SSTa in the same region was performed by using the same period of AF and the sensitivity fields of surface MHW (SST), instead of the upper 100 m surface MHW (SSST). This reconstruction shows improved agreement with the forward run, exhibiting minimal discrepancy. This suggests that mixing is important for the mixed layer but less significant for surface temperature variations in this region, which aligns with the previous discussion ([Fig. 4.2.4](#)) indicating that surface MHWs are less affected by the deeper mixed layer than subsurface MHWs. Although the contribution of mixing cannot be calculated directly in this experiment, the preliminary conclusion is consistent with previous studies indicating that vertical diffusion in the mixed layer is a significant factor influencing Bering Sea temperatures in both winter and summer ([Hayden & O'Neill, 2023](#)). Therefore, through this imperfect reconstruction, it can be concluded that subsurface MHWs are more influenced by wind-induced mixing processes than surface MHWs, in addition to the winter ocean memory previously demonstrated ([Fig. 4.2.4](#)).

In summary, the contribution analysis indicates significant interannual and regional variability in the mechanisms driving NWP MHWs, with horizontal wind-driven processes emerging as a key distinguishing role from NEP MHWs. While SW may be the dominant factor for the July 2022 monthly MHW event, it is not the most important contributor to the

annual event. In the record-breaking 2022 NWP MHW, all AF positively contribute to warming. Turbulent heat flux – encompassing contributions from T2M and SH – is more influential than radiative flux (SW and LW) in both NEP and NWP MHWs. In contrast to the NEP, where sensible heat flux and latent heat flux contribute equally, the 2022 NWP MHW is more heavily influenced by sensible heat flux. Additionally, the accurate reconstruction in the NEP enables annual MHW predictions up to 3-6 months in advance. In contrast, unresolved mixing processes when employing adjoint methods complicate the prediction in the NWP. Nevertheless, the strong correlation (0.92) between the reconstruction and ORAS5 reanalysis data (solid navy line) facilitates the identification of the dominant drivers qualitatively, warranting further validation through perturbation experiments.

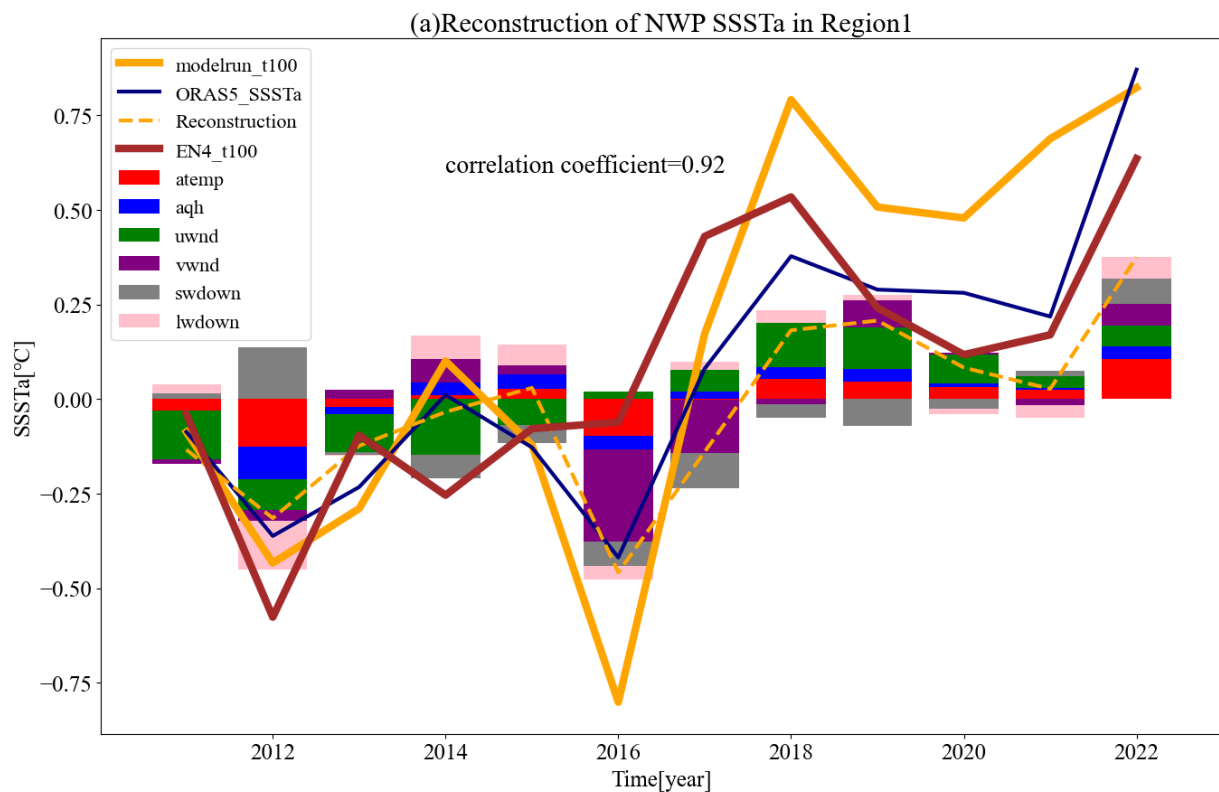


Fig. 4.2.9. Reconstruction of SSSTa at NWP target region from 2011 to 2022. Solid lines show the ORAS5 reanalysis (navy), EN4 observations (brown) and the model forward run (orange); the dashed orange line represents the reconstruction using the first 4-yr mean sensitivity patterns of all adjoint experiments and all AF. Color bars show different contributions from AF (red: T2M; blue: SH; green: U; purple: V; grey: SW; pink: LW). Correlation coefficients between the reconstruction and different datasets: ORAS5 (0.92) shows a strong relationship, while EN4 (0.69) shows a moderate relationship.

#### 4.2.4. NWP MHW Perturbation Experiments

The adjoint sensitivity pattern reveals the optimal perturbation of control parameters leading to SSST changes in the target regions. To understand how the optimal drivers identified from the sensitivities influence the ocean state given realistic AF variability, the sensitivity fields were multiplied with the standard deviations of AF to generate the perturbations (Eq. 3.13). These perturbations were then applied in forward model runs, enabling a direct evaluation of their impact on the ocean state by comparing them to the original control run. Initially, the perturbation fields were generated based on sensitivity patterns (e.g. Figs. 4.2.3, 4.2.5-4.2.6) from the 2022 adjoint experiment. Then they were subsequently applied, both simultaneously (adding T2M, SH, U, V, LW, and SW together) and separately, to the respective forcing fields over a 5-year period preceding 2022 and preceding 2018. Applying the same perturbation to different years (2014 to 2018 and 2018 to 2022) results in different warming scenarios, indicating how SSST changes are sensitive to the background ocean conditions, as suggested by the sensitivities. Specifically, applying the same U perturbation before 2022 led to a warming effect that was twice as strong as when the same perturbation was applied before 2018. This suggests that the ocean state in 2022 is particularly favorable for U to induce warming. However, it should be noted that the perturbations applied are based on the 2022-experiment and they are not the only patterns that can influence the cost function changes.

Given the importance of U and their differing sensitivity distributions between the two experiments for the target year and -1yr (Fig. 4.2.6), U perturbation experiments are primarily focused on by separately introducing positive and negative perturbations according to their responsive regions. While wind stress causes ocean currents, what is important is the horizontal gradient across distances, not just absolute strength (Hu et al., 2015). Therefore, wind stress curl is highlighted in Fig. 4.2.10. Specifically, the left column shows the changes in wind stress curl compared to the control run, resulting from the addition of all AF perturbations (U, V, T2M, SH, SW, LW) to the original forcing field. The middle column illustrates the addition of enhanced westerly winds to the WBS region and the area south of the box, as depicted in Fig. 4.2.6. Meanwhile, the right column presents the effects of enhanced easterly winds to the east of the box, along the Aleutian Islands.

The negative wind stress curl in the target year mainly corresponds to the enhanced easterly winds (left column vs right column). Such curls induce Ekman pumping, pushing water downward and allowing warmer surface water to enter from the sides, deepening the warm surface layer and resulting in a positive SSHa ([Fig. 4.2.11](#)). Propagation signals are also detected in both the wind stress curls fields and the SSHa fields from Year -2 to Year 0. Enhanced easterly winds result in classic Rossby wave excitation, leading to a clear westward propagation of SSH. The propagation speed is estimated to be 1.1 cm/s from the figure, which is consistent with the typical Rossby phase speed observed in mid-latitudes. However, the impact of enhanced easterly winds is actually less than one-third of the impact of enhanced westerly winds.

Enhanced westerly perturbations create a more complex scenario, characterized by a less significant propagating signal and greater warming in the target region. Before the target year, enhanced westerlies cause a quadrupole wind stress curl pattern to shift to a dipole pattern around the target region. This leads to increased Ekman pumping and suction, while SSH changes remain small. This is primarily because the main warming occurs in the subsurface layers rather than at the surface ([Fig. 4.2.12](#)). During Year -1 and Year 0, upwelling is dominant in the target box (middle column in [Fig. 4.2.10](#)) with a clear upward warming movement ([Fig. 4.2.12](#)), leading to noticeable warming at the surface. As previously discussed, the heat stored below the mixed layer is an important precondition for subsequent MHW re-surfacing through upwelling processes. Additionally, during Year -1, anomalous westerlies are already present in the NP (north of 50°N) according to original forcing data. The introduction of enhanced westerly perturbations could further increase wind-driven turbulence, potentially increasing vertical mixing and thereby amplifying the warming effect.

It should be noted that the results of perturbation experiments may not exactly match those of the contribution analysis. The perturbation fields are calculated from the standard deviation of AF which does not reflect the actual forcing fields in the target year. It can help confirm that the sensitivities are valid and suggest possible warming mechanisms. Also, as noted before, the adjoint run excludes non-linear and vertical mixing processes that are incorporated in the forward model. Therefore, the horizontal winds could play a more significant role when considering the full impact of wind-induced mixing processes.

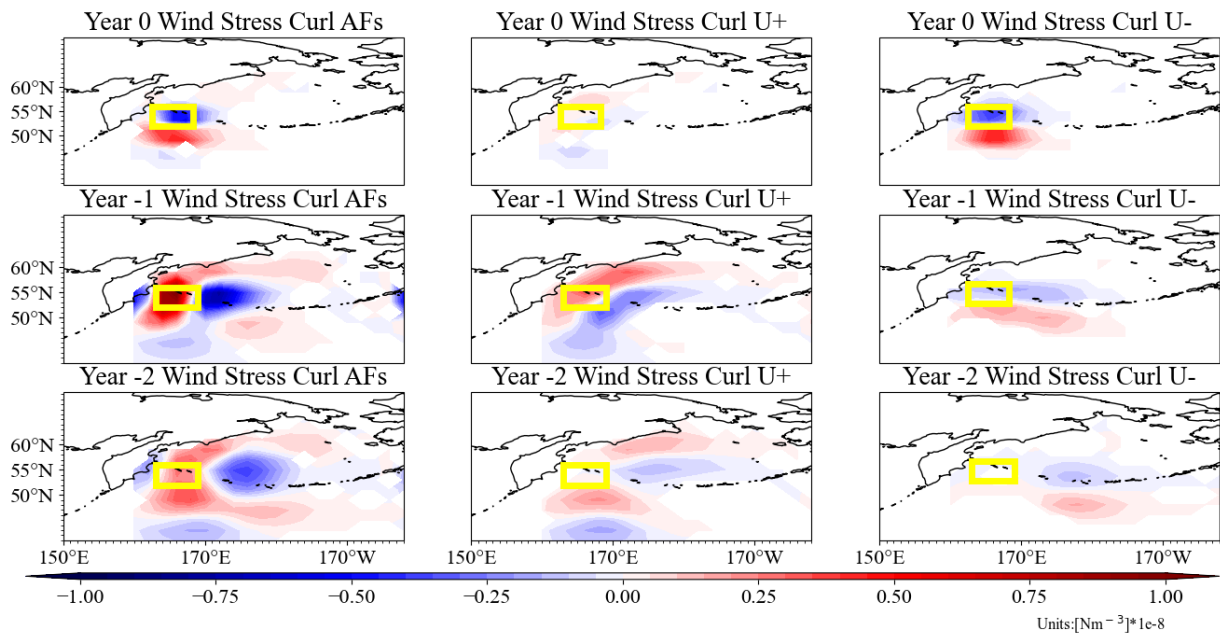


Fig. 4.2.10. (Left column) Time evolution of wind stress curl changes (perturbation run – control run) from -2yr to 0yr (from bottom to top, 0yr is the target year), derived from perturbation experiments that incorporate all perturbations (U, V, T2M, SH, SW, LW) added to the original forcing fields from 2018 to 2022. The perturbation fields are calculated based on the 2022 sensitivity solutions and the standard deviation of all AF (Eq. 3.13). (Middle column) As in the left column, but only enhanced westerly winds are added as the perturbation. (Right column) As in the left column, but only enhanced easterly winds are added as the perturbation.

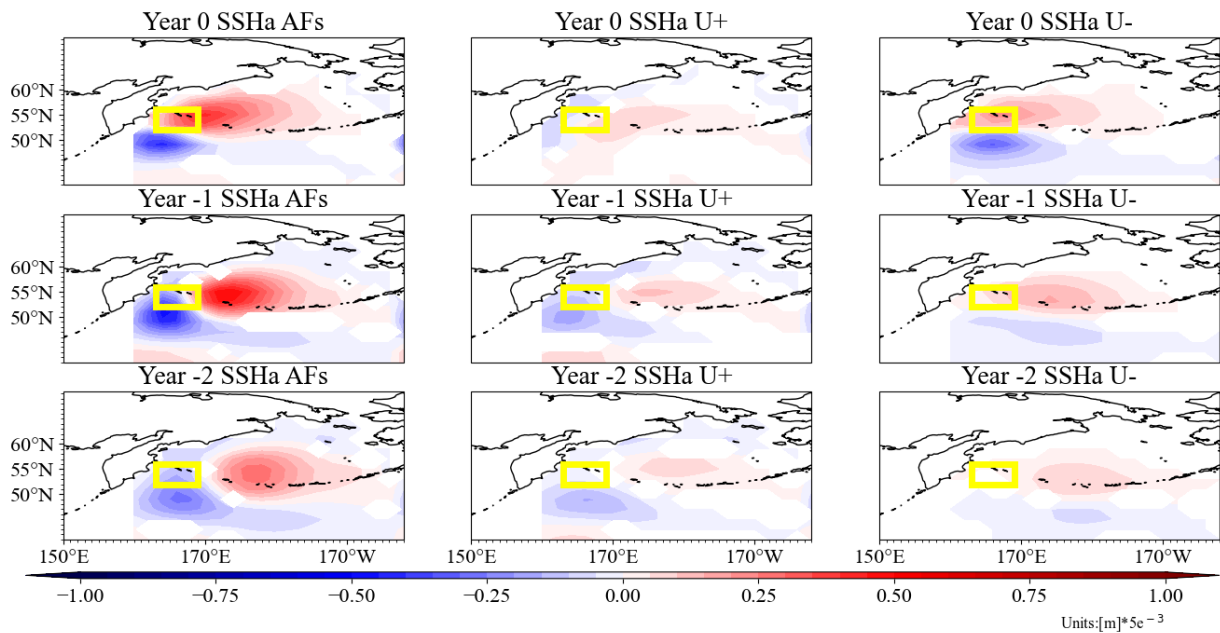


Fig. 4.2.11. As Fig. 4.2.10, but for SSH changes.

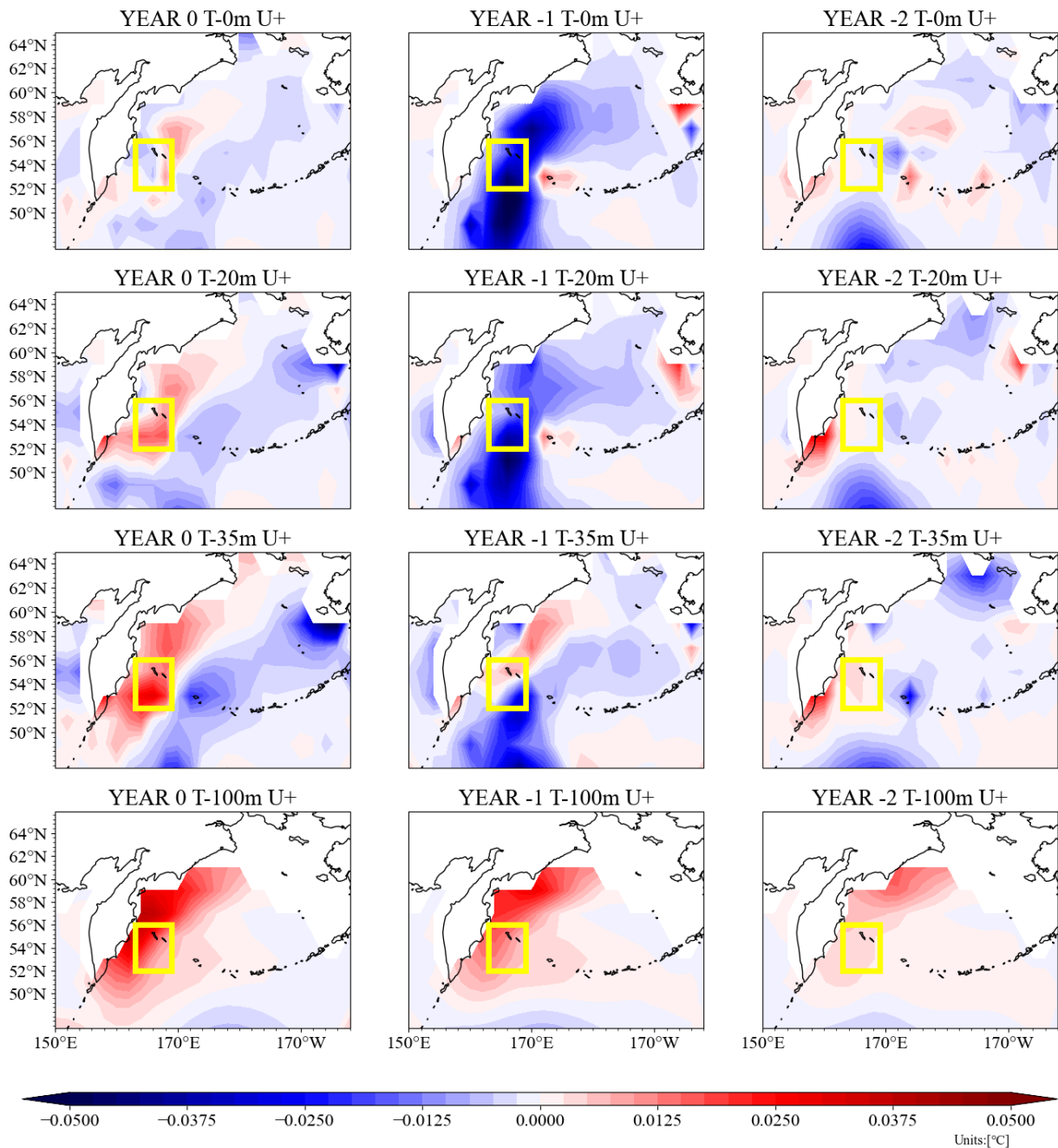


Fig. 4.2.12. Time evolution (from right to left: -2yr to 0yr, 0yr is our target year) of potential temperature changes (perturbation run – control run) at different depths (first row: at the surface; second row: 20 m; third row: 35 m; fourth row: 100 m) for the experiment using enhanced westerly winds perturbation fields calculated by 2022 sensitivity solutions and the standard deviation of  $U$  (Eq. 3.13).

#### 4.2.5. NWP Surface MHW in July 2022

The year-long subsurface MHW was specifically investigated first, emphasizing the role of horizontal wind patterns, particularly U, in sustaining the event. However, for comparative context, a short-lived surface MHW in July 2022 was also analyzed. The cost function is thereby defined as the month mean SST of 2022 July. The target region is indicated by the yellow box in [Fig. 4.2.13a](#) which follows the region chosen by Song et al. (2024). The areas most sensitive to heat flux terms are localized within the selected box, while regions to the east of the KP in the WBS exhibit lower sensitivity. This pattern is similar to that of the annual subsurface MHW ([Fig. 4.2.3](#)). The difference is that monthly MHWs have a shorter response time to AF. The intensity of sensitivity peaks during the leading three months and weakens over longer periods. During -21mon (October), a small sensitivity center is observed in the WBS, exhibiting stronger sensitivity compared to the previous months. This observation aligns with [Fig. 4.2.4](#), which indicates that July MHWs exhibit relatively higher sensitivity to the preceding winters. The sensitivity fields of other AF are not presented, as there is consistency in the identification of the most sensitive regions.

The same contribution analysis was applied to evaluate differing contributions made by various AF ([Fig. 4.2.14](#)). This also facilitates a direct comparison with findings from the heat budget analysis conducted by Song et al. (2024). As they suggested, SW ([Fig. 4.2.14c](#)) serves as a significant contributor to the overall warming; however, it is not the sole factor, as T2M contributes at a comparable level to SW ([Fig. 4.2.14a](#)). SW exhibits immediate, notable impacts during the target month and one month before, likely linked to synoptic-scale atmospheric conditions and enhanced solar heating. However, T2M emerges as the dominant cumulative driver, reflecting its persistent influence on ocean-atmosphere heat exchange by sensible heat flux. SH contributes less than both SW and T2M, predominantly in regions where T2M is the dominant factor, indicating the role of turbulent heat flux and this lower contribution of SH compared to T2M is consistent with previous results of annual MHW. Contributions of LW and V are minimal and can be considered negligible. U component exhibits both warming and cooling effects ([Fig. 4.2.14e](#)). Notably, there is a significant warming contribution in regions where subsurface MHWs have been identified, highlighting the influence of wind-driven oceanic processes. While averaging across the entire region may

lead to a cancellation of opposing contributions, the role of the zonal wind should not be overlooked.

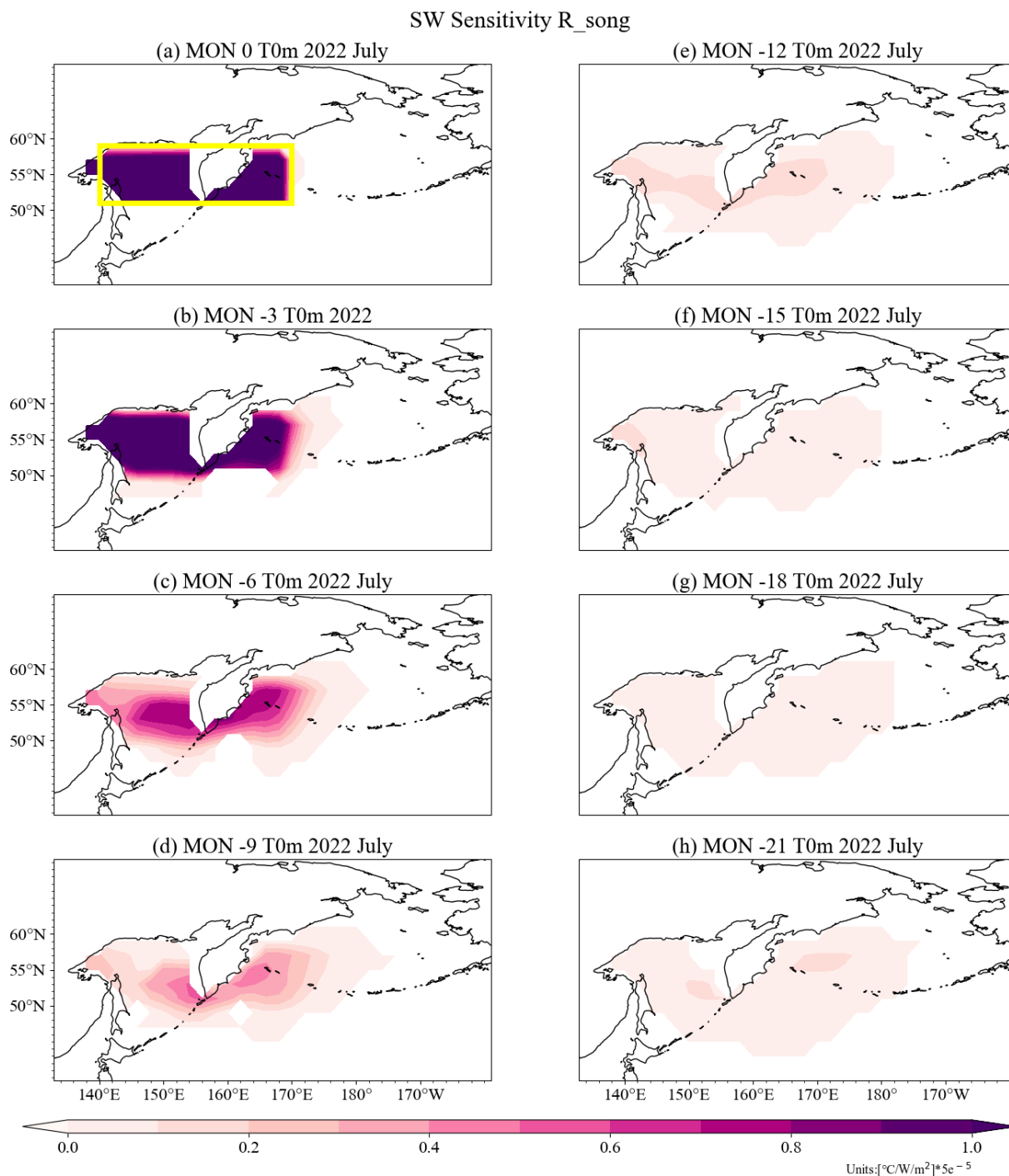


Fig. 4.2.13. Evolution of the adjoint sensitivity of July SST in 2022 with respect to SW (from top left to bottom right backward in time). The yellow box in (a) indicates the target research region.

Total Contribution by AFs

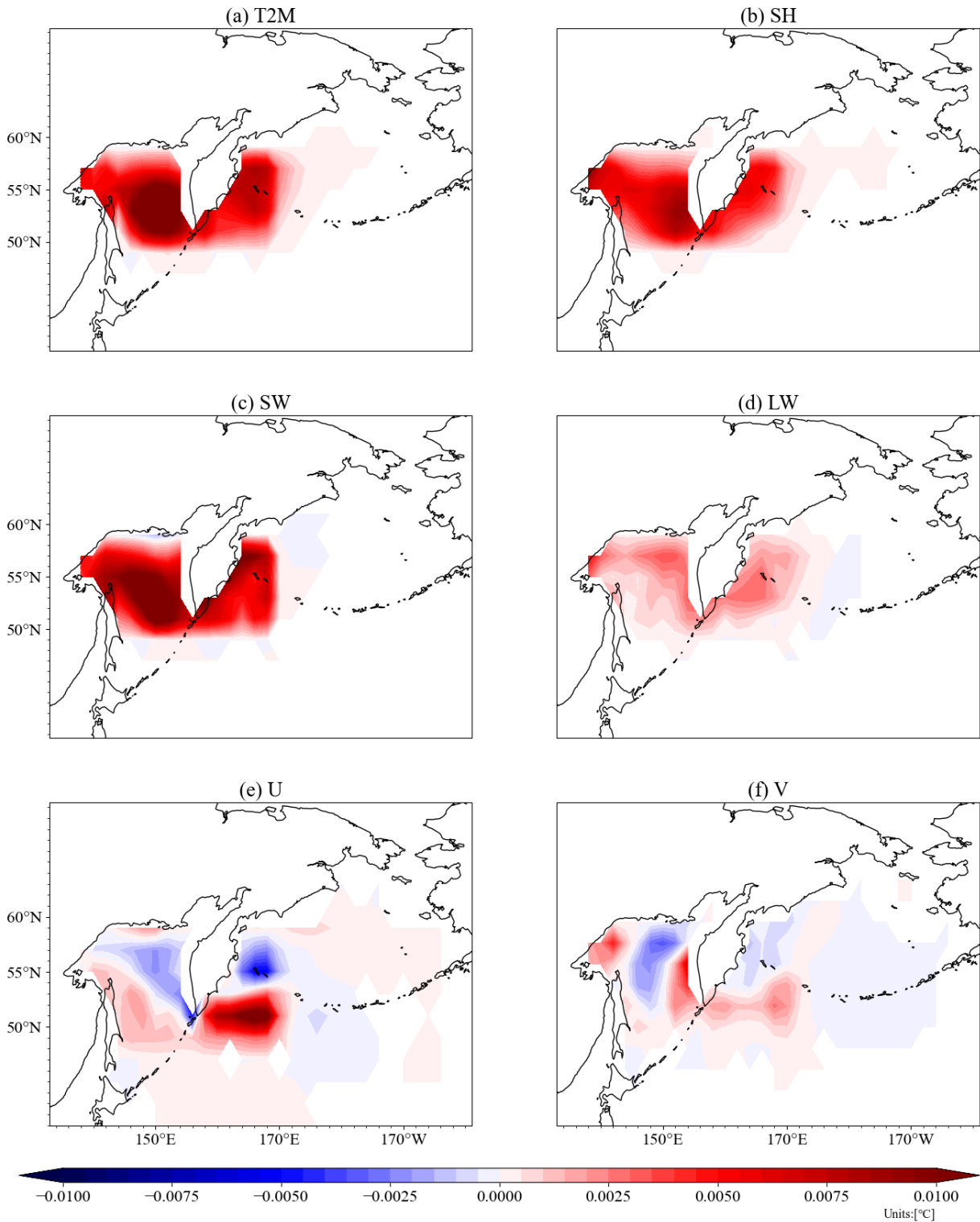


Fig. 4.2.14. The total contribution to 2022 July warming calculated by Eq. 3.8 (the contributions are summed over a total time span of 36 preceding months) with respect to different AF (a) T2M, (b) SH, (c) SW, (d) LW, (e) U, and (f)V. The red shows a positive contribution (warming) and the blue shows a negative contribution (cooling).

Overall, for the July 2022 surface MHW, both surface heat flux and zonal winds are identified as effective contributors. Although the mixing processes are excluded from the analysis, U still plays a significant role. Not considering mixing may also explain the large residual term in Song et al. (2024) since they only consider the advection term ( $\overline{\mathbf{V}} \cdot \nabla T$ ), while the vertical mixing term (e.g. vertical eddy diffusivity  $K_z \frac{\partial^2 T}{\partial z^2}$ ; Vijith et al., 2020; Yang et al., 2024) is part of the residual. Vertical mixing serves as significant as heat flux and horizontal advection in local processes (Holbrook et al., 2020).

Moreover, their target region should be distinctly separated into two areas for analysis, as the contribution distribution reveals different mechanisms across the entire region. The region to the left of the KP is shown to experience high-pressure conditions with upper-level convergence, along with anomalously high net shortwave radiation and low cloud cover. In contrast, the region to the right of the KP is not significantly influenced by this high-pressure system and is more likely situated between an atmospheric ridge and trough with less net shortwave radiation and low cloud cover. The different mechanisms are observed not only at the surface but also in the subsurface. An additional region west of the KP ( $146^\circ \sim 150^\circ\text{E}$ ,  $52^\circ \sim 56^\circ\text{N}$ ) was analyzed as a supporting experiment (Fig. 4.2.15). The contribution analysis for this region shows that heat flux terms dominate the warming with horizontal winds exerting a negative influence. Oceanic processes appear to play a less important role in this region compared to R1 for generating warming. The differences observed suggest that the mechanisms driving MHWs vary significantly based on the location and duration. Understanding these location-specific mechanisms is crucial for improving predictive capability. Given the complex ocean-land interactions and eddy-scale processes in the region to the left of the KP (L'Her et al., 2021), the entire area should be analyzed separately.

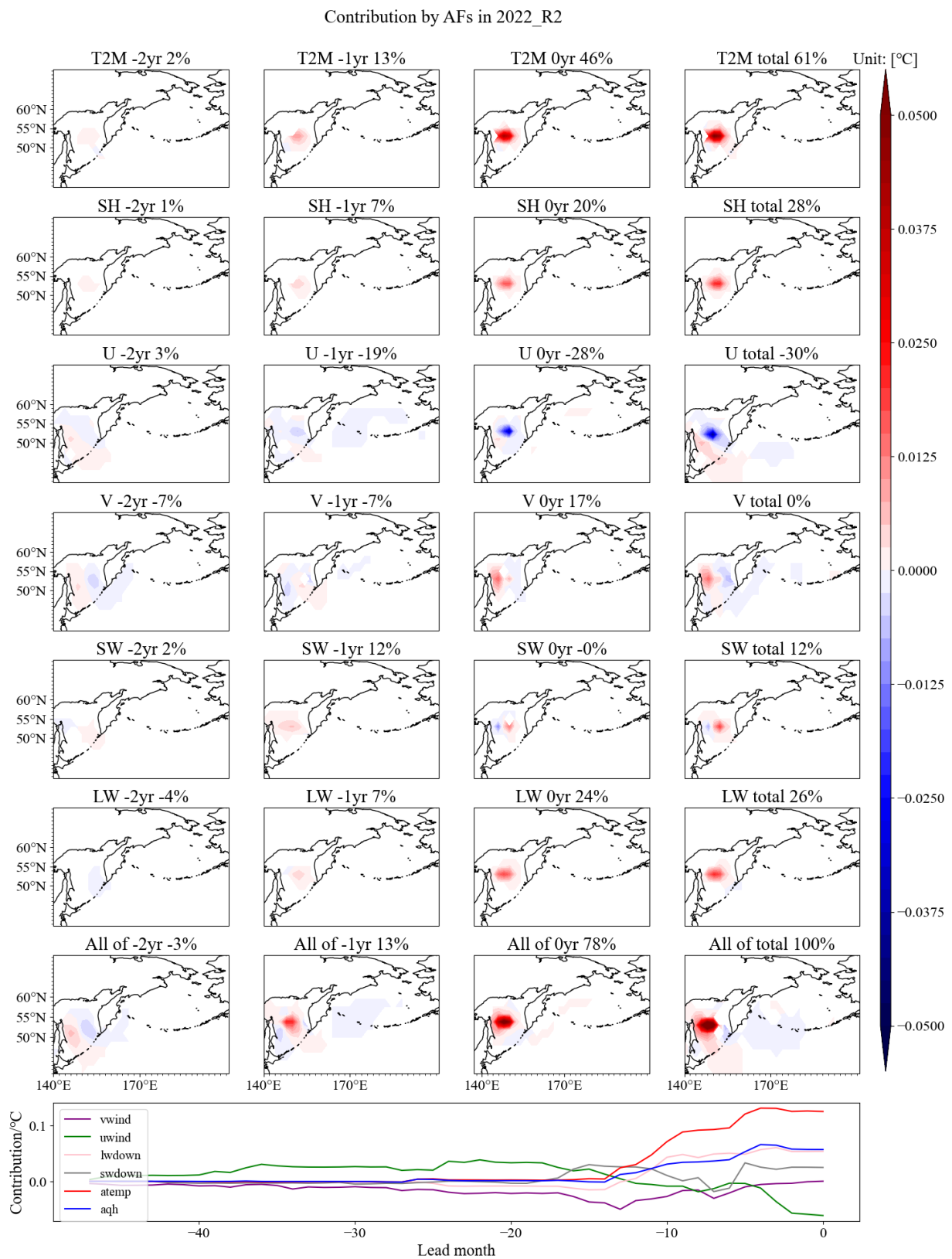


Fig. 4.2.15. As Fig. 4.2.7 and Fig. 4.2.8a, but for the region west of the KP ( $146^{\circ} \sim 150^{\circ}\text{E}$ ,  $52^{\circ} \sim 56^{\circ}\text{N}$ ).

#### 4.2.6. NWP MHW Discussion

The second study investigates the drivers of prolonged subsurface MHWs, which can be more intense and long-lasting than surface MHWs ([Fragkopoulou et al., 2023](#)). Through contribution analysis (multiplying sensitivities with forcing anomalies), the dominant factors driving MHWs in 2022 were identified, with horizontal winds, and T2M emerging as the primary influences. Additionally, winter memory also played a significant role in NWP subsurface MHWs. Perturbation experiments were further employed to validate the linear adjoint method and to explore the detailed mechanisms associated with U anomalies.

Adjoint sensitivities highlight the WBS region and the region south of the Aleutian Islands as the region most responsive to horizontal winds in driving the annual MHW in the target region. Heat flux terms exert a more localized influence, with signals showing slight westward propagation, with its strongest impact occurring between the winter prior to the target year and the target year itself. In contrast, zonal wind effects are detectable up to three years in advance. Contribution analysis confirms that SW significantly contributed to the 2022 warming, whereas it had a negative influence in 2018. While SW has been widely recognized as a key driver of MHWs in the NP ([Liu et al., 2023](#); [Pak et al., 2022](#)), the findings indicate that SW primarily dominates during summer, whereas LW exerts a stronger influence in winter. Overall, T2M emerges as the cumulative driver due to its sustained impact on ocean-atmosphere heat exchange.

Perturbation experiments further validate the sensitivity analysis, revealing the distinct role of zonal winds. Enhanced easterly winds to the east of the target region, which excite Rossby wave propagation, have a weaker impact than the enhanced westerly winds along the coast of the KP. Conversely, enhanced westerly winds (with magnitudes varying with latitude), superimposed on the mean westerly background, strengthen Ekman transport, leading to divergence, which can drive upwelling, bringing subsurface warming to the surface through vertical advection. For example, the unprecedented low levels of sea ice in the Bering Sea during the winter of 2017–2018 ([Duffy-Anderson et al., 2019](#)) resulted in record-high ocean temperatures in 2019 on the southern Bering shelf ([Stabeno et al., 2019](#)). This anomalous warming likely preconditioned the subsequent subsurface MHWs.

The first section of this study identified local air-sea turbulent heat flux as the main driver for NEP MHWs, which is consistent with findings from other studies ([Chen et al., 2021](#); [Ge et](#)

[al., 2023](#)). The second study reveals that the mechanisms of annual NWP MHWs and annual NEP MHWs vary significantly by location and background state. SH is a major driver in the NEP but has a minor impact on the NWP. While other AF contributes in different ways, the role of LW is similar in both NEP and NWP. Several prior studies have also acknowledged the critical contribution of anomalous LW in MHW formation ([Kuroda & Setou, 2021](#); [Schmeisser et al., 2019](#); [Zhao & Yu, 2023](#)), including a strong connection with rising greenhouse gas levels ([Barkhordarian et al., 2022](#)). Low-than-normal wind speeds have been identified as a major driver of MHWs by many studies ([Oliver et al., 2021](#); [Sen Gupta et al., 2020](#); [Travkin et al., 2024](#)) due to their reduced mixing effects. In contrast, the role of increasing wind speeds is seldom addressed ([Gröger et al., 2024](#)). This study could serve as an example to illustrate the re-emergence of MHWs ([Alexander et al., 1999](#); [Capotondi et al., 2024](#)) through the vertical advection of stored ocean heat.

NEP MHWs highly correlate with the NPGO, while several NWP MHWs are more likely related to low PDO and ENSO conditions. NEP MHWs that began in 2014 led to a fundamental change in the PDO ([Werb & Rudnick, 2023](#)), suggesting a potential influence on the subsequent NWP MHWs. For example, the westward-flowing Aleutian Current (a continuation of the Alaska Current) south of the Aleutian Island can bring warmer water from NEP MHWs into the NWP region. For the 2022 NWP case, results show that horizontal wind, especially U, significantly influences NWP MHWs, whereas wind is less critical in the NEP. NEP MHWs rely more on the persistence of the weather system and ocean memory, allowing for predictions in that region. In contrast, NWP MHWs are more complex to forecast. Besides the influences of heat flux and ocean memory, there are various processes driven by wind-induced oceanic vertical advection (upwelling) and potential vertical mixing. However, wind anomalies in the WBS and the westward-extending Aleutian Current should be given greater attention, as the adjoint sensitivities demonstrate significant influence in these regions.

A key limitation of this study is that vertical mixing processes cannot be directly quantified using the adjoint method. Additionally, the current 2-degree model resolution lacks precision for analyzing monthly extremes. Further work should focus on incorporating daily AF or improving the model resolution to better capture short-term MHW variability.

#### 4.2.7. NWP MHW Summary

In this section, the study extends previous research on MHWs in the NWP region. To shed new light on the mechanisms underlying MHWs in the NWP, the adjoint sensitivity of the volume-averaged potential temperature of the NWP target regions (i.e.  $163^{\circ} \sim 169^{\circ}\text{E}$ ,  $52^{\circ} \sim 56^{\circ}\text{N}$ , 0-100 m) at different target years including the MHW year 2022 and the reference year 2018 and different target months including July and December, are investigated. Adjoint sensitivities and contribution analysis show that in the target region surface heat flux and the effect of wind stress are both important for generating a MHW in the NWP, especially the wind pattern in the WBS. For MHW year 2022, the period that exhibits the highest impact on the generation of an MHW occurs 1 year before the target year, contributing up to 80% of the total warming. The results confirm the importance of SW in generating the MHW in 2022, while it has a negative contribution in 2018. It is found that LW plays a similar role as SW; SH contributes the least in NWP, in contrast to the NEP where it serves as the most significant driver. Results thereby reveal that NEP and NWP MHWs are distinct, indicating that the mechanisms driving MHWs are highly dependent on location. In short, NEP MHWs are primarily driven by factors modulating the heat flux, whereas NWP MHWs are influenced by both heat flux and wind-driven oceanic heat convergence. Heat flux terms primarily affect local conditions during the target year, whereas U influences are observed to extend from the preceding three years. Enhanced westerlies appear to exhibit a larger influence compared to enhanced easterlies.

## 5 Conclusion and discussion

### 5.1 Summary

MHWs have garnered significant attention in research efforts in recent times, particularly in the NEP region, due to their profound effects on ocean ecosystems, climate variability, and atmospheric circulation patterns. However, most studies have focused on short-term MHWs using heat budget analysis and statistical methods, leaving long-lasting MHWs poorly understood. This study was driven by the necessity to comprehend the underlying physical processes governing these long-lasting extreme ocean warming events and their interaction with AF.

Therefore, this thesis employed the ECCO technology, which integrates the MITgcm and its adjoint model to investigate the potential drivers of MHWs in the NP and addressed the following key research questions: (1) What are the primary drivers of MHWs in the NEP and NWP, and how do they differ? (2) Can the results be compared to those obtained from other methods and help resolve previously unsolved problems? In brief, the sensitivity fields of the cost function concerning various AF are derived from the adjoint model simulations. These fields are combined with the actual anomalies in AF to conduct a contribution analysis aimed at quantifying the dominant drivers of MHWs. Additionally, perturbation experiments are performed to validate the adjoint solutions through complete non-linear forward model runs.

*Question 1: What are the primary drivers of MHWs in the NEP and NWP, and how do they differ?*

The study explores the mechanisms driving MHWs in both the NEP and NWP, highlighting the regional differences in AF influences. In the NEP, MHWs are primarily driven by local turbulent heat fluxes, with T2M, SH, and LW collectively accounting for up to 80% of the temperature anomaly during MHW years. Horizontal winds are generally not a significant driver of MHW in the NEP region. AF anomalies occurring 3 to 6 months before an MHW event emerge as critical predictors, with extended reconstructions showing that incorporating leading 36-month atmospheric conditions improves predictive skill beyond the persistence method.

In contrast, the NWP MHWs are influenced by both wind-driven processes and heat fluxes, particularly in regions like the WBS. In the 2022 MHW event, horizontal wind and T2M were the leading drivers of the MHW, each contributing approximately 30% to total warming, which is equivalent to the combined effects of LW and SW. However, SH played a minimal role—a stark contrast to the NEP, where it is a primary driver. Horizontal wind patterns, especially enhanced westerly anomalies, significantly influence MHW formation in the NWP through oceanic heat convergence. U influences can persist for up to three years before an MHW event due to the ocean's multi-year memory, which facilitates heat storage and subsequent heat re-emergence.

Ocean winter memory is crucial for both regions, and subsurface MHWs deserve more attention, as the heat stored in deeper layers can serve as an important predictive signal for upcoming extreme warming events. The study of the NWP MHWs also provides valuable insights into the mechanisms driving the MHW re-emergence, which are influenced by heat flux, wind patterns, ocean circulation, and seasonal cycle variations, among other factors.

*Question 2: Can the results be compared to those obtained from other methods and help resolve previously unsolved problems?*

A key contribution of this study is the introduction of a novel approach to identifying physically explainable dominant drivers of long-lasting subsurface MHWs. In contrast to conventional statistic-based approaches, this method facilitates a more direct evaluation of the causal link between AF and ocean temperature anomalies. Additionally, adjoint methods reveal a clear temporal evolution of the drivers, whereas heat budget analysis provides instantaneous or time-averaged snapshots that fail to identify preconditioning events or time-lagged drivers. Overall, the identified driver (i.e., local turbulent heat flux) for NEP MHWs in this adjoint sensitivity study is consistent with many previous studies. This not only strengthens the understanding of the driving mechanisms but also identifies key influential periods and areas related to the physical processes, thereby providing potential signals for MHW predictions. The driver identified for the monthly MHWs in the NWP is not consistent with previous studies. As the mixing processes cannot be quantified in the current model setup, the exact contribution of the larger residual term in other studies remains unconfirmed. However, this study presents several possibilities to explain it and offers suggestions for the direction of subsequent research to address this issue.

## 5.2 Discussion

Although this study effectively examines the key drivers of MHWs in the NP and their evolution using a physical ocean model, it remains an ocean-only model. Therefore, understanding how the identified drivers interact with the complex coupled climate systems is essential. This understanding will enable more accurate predictions by focusing on the most influential factors during their most influential period. The following discussion addresses how various factors influence different regions and the potential for making predictions by applying identified drivers. Additionally, the limitations of the ocean model are also discussed.

**The role of turbulent heat flux:** NP MHWs are both influenced by air-sea turbulent heat flux (sensible and latent heat flux). Their effects are as follows: Sensible heat flux is the transfer of heat caused by temperature differences. In the NEP, an anomalous high-pressure system typically prevails in the summertime ([Amaya et al., 2020](#); [Bond et al., 2015](#); [Di Lorenzo & Mantua, 2016](#)), inhibiting low-cloud formation because the sinking air warms and dries the atmosphere, creating a stable environment and preventing the rising motion needed for condense. Clear skies lead to more solar radiation reaching the surface, warming the water. The increased SST directly heats the air above the ocean, reducing the temperature gradient between the air and the ocean. Additionally, a small fraction (~20%) of solar radiation directly heats the air to reduce the gradient. As a result, the rate of sensible heat loss from the ocean is diminished. This also holds for the latent heat flux representing heat exchange from evaporation. Typically, the ocean cools through evaporation, which absorbs heat as water transitions from liquid to vapor. However, as near-surface air becomes more humid, the humidity difference between the ocean and the air decreases, reducing evaporation and causing warming. Additionally, under high-pressure conditions, where winds tend to be weak, less movement keeps the humidity gradient small and further reduces latent heat exchange. During winter, weaker-than-normal winds in MHW years can limit ocean mixing with deeper layers, trapping heat in the upper ocean. This results in a lower temperature gradient compared to a normal winter ([Bond et al., 2015](#)), reducing turbulent heat loss. Unlike NEP, SH contributes less than T2M in the NWP. This is because the T2M anomaly, which exceeds about three standard deviations, is larger than the SH anomaly, which only exceeds approximately two standard deviations. Winds play a lesser role at middle to high latitudes, where sensible and

latent heat flux are more influenced by temperature and humidity anomalies, whereas in the tropics and subtropics, they are primarily linked to wind speed anomalies ([Alexander, 2010](#)). However, the inconsistency in the distribution of T2M and SH anomalies contributing to the NWP MHW requires further research.

**The role of horizontal winds:** NWP MHWs are more related to wind-induced vertical advection (upwelling) and wind-driven Rossby wave propagation. The selected region in this study is highly sensitive to the WBS conditions and the region south of the Aleutian Islands. When strengthened westerly winds occur to the east of the KP and in the WBS, they can induce divergence due to Ekman transport and result in upwelling. Typically, this upwelling brings cold bottom water to the surface ([Zhabin et al., 2022](#)) unless the subsurface waters are warmer than normal; in that case, the warm water will be upwelled instead. Therefore, the winter heat storage below the mixed layer is a crucial driver for MHW formation. Additionally, if the Alaska Coastal Current south of the Aleutian Islands is warmer, the resulting temperature anomaly can propagate westward to the target region through Rossby wave dynamics, even if the currents are weakened. This is due to Rossby waves transmitting thermocline adjustments through upwelling and downwelling ([Pinault, 2022](#)) rather than moving warm water physically. This can build a potential link between NWP MHWs and NEP MHWs, as NEP MHWs significantly influence the Alaska Current region ([Di Lorenzo & Mantua, 2016](#); [Rallu De Malibrán et al., 2024](#)).

**The role of radiative flux:** Throughout the study, the observed influence of SW was less significant than initially hypothesized. Conversely, LW was found to exert a more substantial impact within the NP region. This phenomenon may be attributable to the annual timescale employed in the study. On a short-term temporal scale, such as a daily timeframe, the presence of cloud cover significantly influences the solar radiation incident upon the ocean surface. Seasonal variations in albedo, driven by the melting and refreezing of sea ice as a consequence of SW, can also significantly impact temperature dynamics. However, within the context of the study area, the influence of sea ice is comparatively minimal. In this study, the primary focus is on the annual scale, particularly regarding the long-lasting phenomenon known as the ‘blob’ and year-long subsurface MHW in the NWP. Therefore, the role of SW is not as important for long-term MHWs as it is for short-term MHWs ([Bailey et al., 2025](#); [Song et al., 2024](#); [Wang et al., 2023b](#)).

**The predictability and the application:** NEP MHWs are potentially predictable due to their consistent sensitivity to AF across years. This discussion emphasizes the use of observed AF data or reanalysis data for MHW prediction. While employing atmospheric forecast data can extend MHW prediction lead time, such products often depend on SST data. Relying on SST-based AF forecasts to subsequently predict MHW creates circular dependencies, thereby undermining reliability. If predictions are made at the beginning of the target year, an accuracy rate of 66% can be achieved using sensitivity solutions and corresponding AF. This approach outperforms persistence-based forecasting methods, which rely on December ocean temperatures for predictions and achieve an accuracy of only 62%. However, NWP MHWs predictions are more challenging due to variations in sensitivity distribution across different years. Nonetheless, there are still predictive signals worth exploring, and these approaches can also be applied to other regions. In general, the prediction focuses on the following aspects: First, it is important to identify the areas of highest sensitivity (e.g. zonal wind anomalies in the WBS for the NWP MHWs and local turbulent heat flux changes in the NEP MHWs) and the critical periods (e.g. preceding winters for the NWP MHWs and preceding 3 months for the NEP MHWs) of AF that contribute to MHW in the target region. Next, attention should shift to heat sources and transport mechanisms. For instance, the heat source may involve determining whether incoming heat flux is increasing due to higher solar radiation under clear skies, if outgoing heat flux is decreasing due to a reduced air-sea temperature/humidity gradient (e.g. NEP MHWs), or if warmer subsurface waters are hidden beneath the mixed layer (e.g. NWP MHWs). Regarding transport, factors such as wind-induced advection through ocean currents, wind-driven Ekman upwelling or downwelling, wind-induced turbulence mixing, and wind-excited Rossby wave propagation should also be considered. Other influencing factors also exist but are not detailed here.

**The limitation of the numerical model and the adjoint method:** The forward model with a 2-degree resolution has inherent limitations in simulating extremely abnormal high temperatures. When used for a backward adjoint run, it may weaken the contributions from AF and miss certain small-scale processes leading to extreme warming. Contribution analysis is based on real-world anomalies but ignores nonlinearity and mixing processes in the current setup. Based on this study, the adjoint method is especially useful in the NEP (compared to the NWP) and at the surface (compared to the subsurface), where wind-induced mixing and nonlinear processes are less significant. Furthermore, an ocean-only model allows us only to

identify dominant AF as external drivers, limiting our ability to determine the causes of atmospheric anomalies. Thus, it is challenging to conclude whether MHWs are linked to climate change or climate modes. Future research should utilize atmosphere-ocean coupled models or alternative methods to investigate the causes of atmospheric anomalies. Alternatively, since T2M is important for both study regions, the atmospheric model with adjoint may also be introduced by setting anomalously high air temperatures as the cost function to identify the underlying drivers.

### 5.3 Outlook

The ocean-only model in this study uses bulk formulas to compute air-sea exchanges based on AF which contains the effect of climate change (e.g. global warming trends) and natural variability (e.g. ENSO-driven wind anomalies). These interconnected factors cannot be separated in the forcing fields, which restricts the model's ability to detect how MHWs might influence or be affected by atmospheric teleconnections and remote interactions. For example, the NEP MHWs are often associated with phases of the PDO or NPGO, whereas those in the NWP rely on the background ocean state. However, this study could not clarify the origins of anomalous heat flux and wind patterns during MHWs, nor does it determine the exact role of global warming in increasing their frequency or intensity. Future studies could focus on diagnosing the drivers of anomalous atmospheric conditions, such as enhanced westerlies or prolonged high-pressure systems, and exploring whether these extreme conditions are linked to the changing climate. Employing a coupled atmosphere-ocean model could bridge these gaps by resolving interactions between tropical and midlatitude processes through atmospheric teleconnections, which would facilitate a more comprehensive understanding of their influence on MHWs.

**The extreme atmospheric conditions:** The formation of NWP MHW can be attributed, to some extent, to both anomalous high westerly winds and warmer-than-normal subsurface ocean conditions. It was discovered in the research that in December 2021, there were exceptionally strong westerly winds in the WBS and the target region in the NWP, along with anomalous high easterly winds in the central NP. This was accompanied by surface divergence and convergence at 250 hPa, indicating the presence of an unusual downdraft caused by a high-pressure system. Furthermore, the winter NPSH in December 2021 was also observed as the

strongest since 1949. Additionally, the first "triple-dip" La Niña events of the twenty-first century between 2020 and 2022 resulted in elevated risks due to the extended periods of the extremes ([Johnson et al., 2023](#)). These extreme conditions may be closely related to significant warming in the NP and need further exploration.

**The changing climate:** It is evident that the NP has been warming in recent years; however, it remains unclear whether this warming is leading to an increase in MHWs or if the MHWs themselves are contributing to the warming. A hiatus period occurred of ongoing global warming between 1998 and 2013 ([Trenberth & Fasullo, 2013](#)). Since then, recent years have witnessed alterations in the NP climate pattern, including accelerated warming starting from 2014. The climatology of surface winds, particularly the zonal winds, indicates a significant intensification of the subtropical westerly winds since the mid-1980s ([Joh et al., 2021](#)). The intensification of atmospheric circulation patterns ([Heede & Fedorov, 2023](#)) and trade winds have contributed to a reduction in the rate of surface warming in the tropical Pacific Ocean ([Latif et al., 2023](#)). During the period from 1993 to 2022, there has been a sustained enhancement of the upper-ocean circulation in the equatorial Pacific region ([Tuchen et al., 2024](#)). Alizadeh and Babaei ([2023](#)) indicate that both the intensity and the meridional position of the NP jet display a distinct seasonal cycle, with a significant latitudinal variability observed in spring compared to other seasons. The distribution of jets is responsible for the increasing frequency and intensity of MHWs, which may be both a cause and a consequence of blocking events ([Rousi et al., 2022](#)). Furthermore, the behavior of the jet stream and the NP Oscillation can be attributed to Arctic warming ([Song et al., 2023b](#)). Both the major ocean gyres ([Yang et al., 2020](#)) and the KE have shifted northward since 1993, primarily due to changes in wind stress curl ([Kawakami et al., 2023](#); [Navarra & Di Lorenzo, 2021](#)). In addition to the northward shift, KE has also experienced an increase in temperature ([Qiao et al., 2024](#); [Shi et al., 2024b](#)) and strength ([Zhang et al., 2020](#)). While Ren et al. ([2023](#)) suggested that the PDO modulated MHWs in the NEP over the past decades, Werb & Rudnick ([2023](#)) proposed that NEP MHWs that began in 2014 had led to a fundamental change in the PDO. Focusing on the dominant mode of SST from 2013 to 2023, the PDO pattern has already tilted to some extent ([Fig. 6.1a](#)). However, during the period from 2014 to 2023, when MHWs became more frequent, the dominant mode was no longer PDO-like ([Fig. 6.1b](#)). Therefore, caution should be exercised when discussing the relationship between MHWs and changing climate modes.

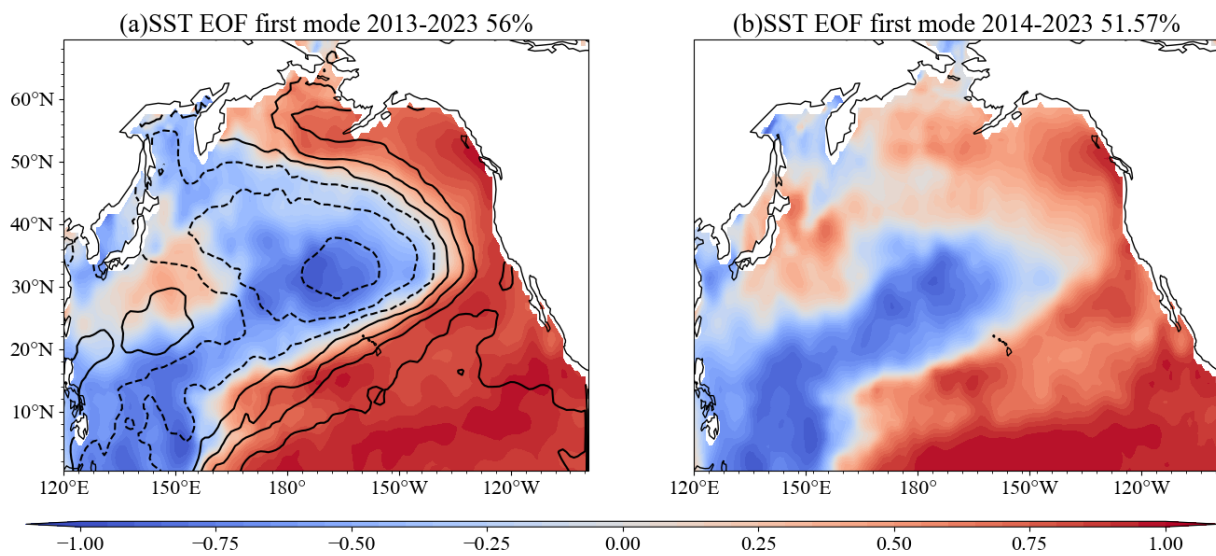


Fig. 6.1. PDO spatial pattern calculated as the first Empirical Orthogonal Function (EOF) mode of detrended HadiSST from (a) 1870 to 2023 (black lines) and 2013 to 2023 (shading) (b) 2014 to 2023 (shading).

**The hypothesis for NP MHW teleconnection:** Based on the results of this study and previous studies, the potential NP MHW mechanisms are hypothesized in [Fig. 6.2](#). Both 2013-15 and 2019-20 NEP MHWs are associated with La Niña events (2010-11 strong La Niña; 2011-12 moderate La Niña; 2017-18 weak La Niña, [Boening et al., 2012](#); [Wang et al., 2023a](#)) that occurred approximately two years prior. During La Niña conditions, there is a significant decrease in SST in the equatorial Pacific Ocean (blue shading). The cooler SST in the central and eastern Pacific creates a greater temperature gradient, which strengthens the trade winds (colorful arrows) and in turn enhances the Walker Circulation and Kuroshio Currents (black arrows, [Kuo & Tseng, 2021](#)). The Kuroshio-Oyashio Extension (KOE, the region resembles KE but is named differently) also serves as a key oceanic frontal zone in the NP, facilitating significant air-sea heat and moisture exchanges ([Joh et al., 2023](#); [Qiu, 2002](#)). Recent studies have suggested the relationship between the KOE and the NEP MHWs ([Silva & Anderson, 2023](#)), as well as the Pacific Decadal Precession ([Anderson et al., 2016](#); [Schneider et al., 2002](#); [Silva & Anderson, 2024](#)). This study indicated that NEP MHWs are somewhat sensitive to air-sea heat and moisture exchanges in that region.

The cooling in the central and eastern Pacific also strengthens the equator-to-pole temperature gradients, which enhances the Polar Jet Stream and induces a southward shift of the jet (colorful lines with arrows). The anomalous convergence of the Polar Jet in the NEP

leads to the development of an anomalous high-pressure system (black dashed lines). This high-pressure system inhibits cloud formation, resulting in clear skies that allow solar radiation to directly heat the air. Subsequently, the anomalous T2M (red shading) and SH (a similar distribution with the T2M since warmer air can hold more moisture), also referred to as the turbulent heat flux, together contribute to the development of NEP MHWs. NEP MHWs can potentially lead to elevated ocean heat content in the NP (e.g. 2017; 2022) and also influence the PDO pattern. Additionally, the warmest ocean conditions in the NP in 2022 were likely dominated by the highest high-pressure and lowest zonal wind on record. Reduced wind stress weakens Ekman transport and vertical mixing, trapping heat in the upper ocean and creating a warm pool. This ocean condition also contributed to NWP MHWs in 2022 by upwelling preconditioned subsurface heat. The warmest ocean conditions in the NP further increase the temperature gradient, which helps maintain La Niña events and contributes to a PDO-like pattern, leading to the occurrence of a triple-year La Niña event. There may be a positive feedback relationship between La Niña events and MHW in the NP to some extent; however, further analysis is needed to confirm this hypothesis.

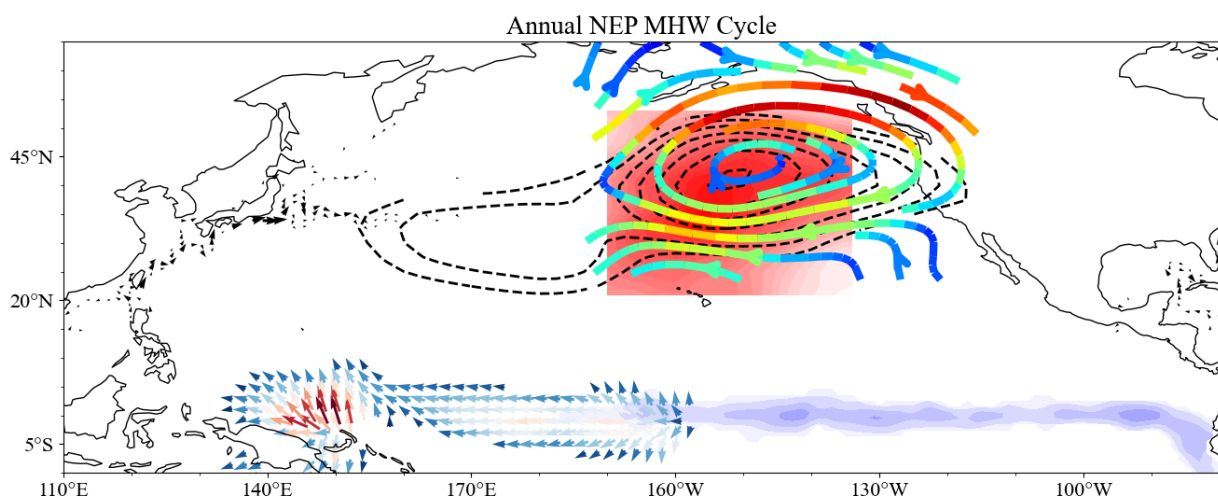


Fig. 6.2. Illustration of the annual MHW cycle (Data shown are anomalous fields based on the 2019/20 case study. The cycle also holds for 2013-15 NEP MHWs). Blue shading indicates the anomalous cooling of HadISST (Rayner et al., 2003) in the equatorial eastern Pacific, which represents La Niña conditions in 2017. Colorful arrows indicate the anomalously strong easterly trade winds (NCEP-RA1; Kalnay et al., 1996) of 2017 in the equatorial western Pacific. Black arrows indicate the anomalous Kuroshio Currents (ORAS5; Climate Data Store, 2025) in 2017. The red shading indicates the anomalous warming of T2M (NCEP-RA1) in 2020. Colorful lines with arrows indicate the Polar Jet Stream at 250 hPa (NCEP-RA1) in 2020. The dashed black lines show the anomalous geopotential height at 500 hPa (NCEP-RA1) in 2020.

## References

- Adcroft, A., Hill, C., Campin, J.-M., Marshall, J., & Heimbach, P. (2004). Overview of the formulation and numerics of the MIT GCM. *Proceedings of the ECMWF Seminar Series on Numerical Methods, Recent Developments in Numerical Methods for Atmosphere and Ocean Modeling*. <http://mitgcm.org/pdfs/ECMWF2004-Adcroft.pdf>
- Alexander, L. V., and coauthors. (2006). Global observed changes in daily climate extremes of temperature and precipitation. *Journal of Geophysical Research: Atmospheres*, *111*(D5). <https://doi.org/10.1029/2005JD006290>
- Alexander, M. (2010). Extratropical Air-Sea Interaction, Sea Surface Temperature Variability, and the Pacific Decadal Oscillation. In *Climate Dynamics: Why Does Climate Vary?* (pp. 123–148). American Geophysical Union (AGU). <https://doi.org/10.1029/2008GM000794>
- Alexander, M. A., Deser, C., & Timlin, M. S. (1999). The Reemergence of SST Anomalies in the North Pacific Ocean. *Journal of Climate*, *12*(8), 2419–2433. [https://doi.org/10.1175/1520-0442\(1999\)012<2419:TROSAI>2.0.CO;2](https://doi.org/10.1175/1520-0442(1999)012<2419:TROSAI>2.0.CO;2)
- Alexander, M. A., and coauthors. (2018). Projected sea surface temperatures over the 21st century: Changes in the mean, variability and extremes for large marine ecosystem regions of Northern Oceans. *Elementa: Science of the Anthropocene*, *6*, 9. <https://doi.org/10.1525/elementa.191>
- Alizadeh, O., & Babaei, M. (2023). Changes in the North Pacific Jet Stream in Recent Decades. *Pure and Applied Geophysics*, *180*(12), 4371–4380. <https://doi.org/10.1007/s00024-023-03363-2>
- Amaya, D. J., and coauthors. (2021). Are Long-Term Changes in Mixed Layer Depth Influencing North Pacific Marine Heatwaves? *Bulletin of the American Meteorological Society*, *102*(1), S59–S66. <https://doi.org/10.1175/BAMS-D-20-0144.1>
- Amaya, D. J., Miller, A. J., Xie, S.-P., & Kosaka, Y. (2020). Physical drivers of the summer 2019 North Pacific marine heatwave. *Nature Communications*, *11*(1), 1903. <https://doi.org/10.1038/s41467-020-15820-w>
- Anderson, B. T., Gianotti, D. J. S., Furtado, J. C., & Di Lorenzo, E. (2016). A decadal precession of atmospheric pressures over the North Pacific. *Geophysical Research Letters*, *43*(8), 3921–3927. <https://doi.org/10.1002/2016GL068206>

- Athanase, M., Sánchez-Benítez, A., Goessling, H. F., Pithan, F., & Jung, T. (2024). Projected amplification of summer marine heatwaves in a warming Northeast Pacific Ocean. *Communications Earth & Environment*, 5(1), 1–12. <https://doi.org/10.1038/s43247-024-01212-1>
- Bailey, S. T., Drake, H. F., Gruenburg, L. K., Abernathey, R. P., & Torres, M. I. (2025). The Thermodynamics of the 2023 Gulf of Mexico Marine Heatwave. *Geophysical Research Letters*, 52(4), e2024GL111768. <https://doi.org/10.1029/2024GL111768>
- Barkhordarian, A., Nielsen, D. M., & Baehr, J. (2022). Recent marine heatwaves in the North Pacific warming pool can be attributed to rising atmospheric levels of greenhouse gases. *Communications Earth & Environment*, 3(1), 1–12. <https://doi.org/10.1038/s43247-022-00461-2>
- Bian, C., Jing, Z., Wang, H., Wu, L., Chen, Z., Gan, B., & Yang, H. (2023). Oceanic mesoscale eddies as crucial drivers of global marine heatwaves. *Nature Communications*, 14(1), 2970. <https://doi.org/10.1038/s41467-023-38811-z>
- Boening, C., Willis, J. K., Landerer, F. W., Nerem, R. S., & Fasullo, J. (2012). The 2011 La Niña: So strong, the oceans fell. *Geophysical Research Letters*, 39(19). <https://doi.org/10.1029/2012GL053055>
- Boland, E. J. D., Jones, D. C., Meijers, A. J. S., Forget, G., & Josey, S. A. (2021). Local and Remote Influences on the Heat Content of Southern Ocean Mode Water Formation Regions. *Journal of Geophysical Research: Oceans*, 126(4), e2020JC016585. <https://doi.org/10.1029/2020JC016585>
- Bond, N. A., Cronin, M. F., Freeland, H., & Mantua, N. (2015). Causes and impacts of the 2014 warm anomaly in the NE Pacific. *Geophysical Research Letters*, 42(9), 3414–3420. <https://doi.org/10.1002/2015GL063306>
- Bryan, F., Kauffman, B., Large, W., & Gent, P. (1996). *NCAR CSM flux coupler. Technical note*. <https://www.semanticscholar.org/paper/NCAR-CSM-flux-coupler.-Technical-note-Bryan-Kauffman/6ec4ace1707bcb84adb52661e12d16318f3f8099>
- Bugnion, V., Hill, C., & Stone, P. H. (2006). An Adjoint Analysis of the Meridional Overturning Circulation in an Ocean Model. *Journal of Climate*, 19(15), 3732–3750. <https://doi.org/10.1175/JCLI3787.1>

- Campbell, S., Remenyi, T. A., White, C. J., & Johnston, F. H. (2018). Heatwave and health impact research: A global review. *Health & Place*, *53*, 210–218. <https://doi.org/10.1016/j.healthplace.2018.08.017>
- Capotondi, A., Newman, M., Xu, T., & Di Lorenzo, E. (2022). An Optimal Precursor of Northeast Pacific Marine Heatwaves and Central Pacific El Niño Events. *Geophysical Research Letters*, *49*(5), e2021GL097350. <https://doi.org/10.1029/2021GL097350>
- Capotondi, A., and coauthors. (2024). A global overview of marine heatwaves in a changing climate. *Communications Earth & Environment*, *5*(1), 701. <https://doi.org/10.1038/s43247-024-01806-9>
- Chauhan, A., and coauthors. (2023). Distribution and impacts of long-lasting marine heat waves on phytoplankton biomass. *Frontiers in Marine Science*, *10*. <https://doi.org/10.3389/fmars.2023.1177571>
- Chen, H.-H., Wang, Y., Xiu, P., Yu, Y., Ma, W., & Chai, F. (2023). Combined oceanic and atmospheric forcing of the 2013/14 marine heatwave in the northeast Pacific. *Npj Climate and Atmospheric Science*, *6*(1), 1–10. <https://doi.org/10.1038/s41612-023-00327-0>
- Chen, Z., Shi, J., Liu, Q., Chen, H., & Li, C. (2021). A Persistent and Intense Marine Heatwave in the Northeast Pacific During 2019–2020. *Geophysical Research Letters*, *48*(13), e2021GL093239. <https://doi.org/10.1029/2021GL093239>
- Cheng, L., and coauthors. (2023). Another Year of Record Heat for the Oceans. *Advances in Atmospheric Sciences*, *40*(6), 963–974. <https://doi.org/10.1007/s00376-023-2385-2>
- Choi, H.-Y., Park, M.-S., Kim, H.-S., & Lee, S. (2024). Marine heatwave events strengthen the intensity of tropical cyclones. *Communications Earth & Environment*, *5*(1), 1–8. <https://doi.org/10.1038/s43247-024-01239-4>
- Christidis, N., Jones, G. S., & Stott, P. A. (2015). Dramatically increasing chance of extremely hot summers since the 2003 European heatwave. *Nature Climate Change*, *5*(1), 46–50. <https://doi.org/10.1038/nclimate2468>
- Climate Data Store. (2025). *ORAS5 global ocean reanalysis monthly data from 1958 to present*. <https://cds.climate.copernicus.eu/datasets/reanalysis-oras5?tab=overview>
- Coumou, D., Di Capua, G., Vavrus, S., Wang, L., & Wang, S. (2018). The influence of Arctic amplification on mid-latitude summer circulation. *Nature Communications*, *9*(1), 2959. <https://doi.org/10.1038/s41467-018-05256-8>

- Czeschel, L., Eden, C., & Greatbatch, R. J. (2012). On the Driving Mechanism of the Annual Cycle of the Florida Current Transport. *Journal of Physical Oceanography*, 42(5), 824–839. <https://doi.org/10.1175/JPO-D-11-0109.1>
- Demirdjian, R., and coauthors. (2020). A Case Study of the Physical Processes Associated with the Atmospheric River Initial-Condition Sensitivity from an Adjoint Model. *Journal of the Atmospheric Sciences*, 77(2), 691–709. <https://doi.org/10.1175/JAS-D-19-0155.1>
- Di Lorenzo, E., and coauthors. (2023). Modes and Mechanisms of Pacific Decadal-Scale Variability. *Annual Review of Marine Science*, 15(Volume 15, 2023), 249–275. <https://doi.org/10.1146/annurev-marine-040422-084555>
- Di Lorenzo, E., & Mantua, N. (2016). Multi-year persistence of the 2014/15 North Pacific marine heatwave. *Nature Climate Change*, 6(11), 1042–1047. <https://doi.org/10.1038/nclimate3082>
- Di Lorenzo, E., and coauthors. (2008). North Pacific Gyre Oscillation links ocean climate and ecosystem change. *Geophysical Research Letters*, 35(8). <https://doi.org/10.1029/2007GL032838>
- Doyle, J. D., Amerault, C., Reynolds, C. A., & Reinecke, P. A. (2014). Initial Condition Sensitivity and Predictability of a Severe Extratropical Cyclone Using a Moist Adjoint. *Monthly Weather Review*, 142(1), 320–342. <https://doi.org/10.1175/MWR-D-13-00201.1>
- Du, Y., Feng, M., Xu, Z., Yin, B., & Hobday, A. J. (2022). Summer Marine Heatwaves in the Kuroshio-Oyashio Extension Region. *Remote Sensing*, 14(13), Article 13. <https://doi.org/10.3390/rs14132980>
- Dubey, A. K., & Kumar, P. (2023). Future projections of heatwave characteristics and dynamics over India using a high-resolution regional earth system model. *Climate Dynamics*, 60(1), 127–145. <https://doi.org/10.1007/s00382-022-06309-x>
- Duffy-Anderson, J. T., and coauthors. (2019). Responses of the Northern Bering Sea and Southeastern Bering Sea Pelagic Ecosystems Following Record-Breaking Low Winter Sea Ice. *Geophysical Research Letters*, 46(16), 9833–9842. <https://doi.org/10.1029/2019GL083396>
- Errico, R. M. (1997). What Is an Adjoint Model? *Bulletin of the American Meteorological Society*, 78(11), 2577–2592. [https://doi.org/10.1175/1520-0477\(1997\)078<2577:WIAAM>2.0.CO;2](https://doi.org/10.1175/1520-0477(1997)078<2577:WIAAM>2.0.CO;2)

- Fazli, H., Kumar, S., Rezamand, A., Daryanabard, G., & Kaur, S. (2025). Caspian Sea fisheries under threat from marine heatwaves. *Estuarine, Coastal and Shelf Science*, 313, 109122. <https://doi.org/10.1016/j.ecss.2024.109122>
- Fragkopoulou, E., and coauthors. (2023). Marine biodiversity exposed to prolonged and intense subsurface heatwaves. *Nature Climate Change*, 13(10), 1114–1121. <https://doi.org/10.1038/s41558-023-01790-6>
- Frederikse, T., and coauthors. (2022). A Hybrid Dynamical Approach for Seasonal Prediction of Sea-Level Anomalies: A Pilot Study for Charleston, South Carolina. *Journal of Geophysical Research: Oceans*, 127(8), e2021JC018137. <https://doi.org/10.1029/2021JC018137>
- Frölicher, T. L., & Laufkötter, C. (2018). Emerging risks from marine heat waves. *Nature Communications*, 9(1), 650. <https://doi.org/10.1038/s41467-018-03163-6>
- Fukumori, I., Lee, T., Cheng, B., & Menemenlis, D. (2004). The Origin, Pathway, and Destination of Niño-3 Water Estimated by a Simulated Passive Tracer and Its Adjoint. *Journal of Physical Oceanography*, 34(3), 582–604. <https://doi.org/10.1175/2515.1>
- Garreaud, R. D., Clem, K., & Veloso, J. V. (2021). The South Pacific Pressure Trend Dipole and the Southern Blob. *Journal of Climate*, 34(18), 7661–7676. <https://doi.org/10.1175/JCLI-D-20-0886.1>
- Ge, Z.-A., Chen, L., Li, T., & Sun, M. (2023). Unraveling the Formation Mechanism of Exceptionally Strong Marine Heatwaves in the Northeast Pacific in 2020. *Journal of Climate*, 36(23), 8091–8111. <https://doi.org/10.1175/JCLI-D-22-0947.1>
- Gent, P. R., & McWilliams, J. C. (1990). Isopycnal Mixing in Ocean Circulation Models. *Journal of Physical Oceanography*, 20(1), 150–155. [https://doi.org/10.1175/1520-0485\(1990\)020<0150:IMIOCM>2.0.CO;2](https://doi.org/10.1175/1520-0485(1990)020<0150:IMIOCM>2.0.CO;2)
- Gentemann, C. L., Fewings, M. R., & García-Reyes, M. (2017). Satellite sea surface temperatures along the West Coast of the United States during the 2014–2016 northeast Pacific marine heat wave. *Geophysical Research Letters*, 44(1), 312–319. <https://doi.org/10.1002/2016GL071039>
- Giamalaki, K., Beaulieu, C., & Prochaska, J. X. (2022). Assessing Predictability of Marine Heatwaves With Random Forests. *Geophysical Research Letters*, 49(23), e2022GL099069. <https://doi.org/10.1029/2022GL099069>

- Giering, R., & Kaminski, T. (1998). Recipes for adjoint code construction. *ACM Trans. Math. Softw.*, 24(4), 437–474. <https://doi.org/10.1145/293686.293695>
- Good, S. A., Martin, M. J., & Rayner, N. A. (2013). EN4: Quality controlled ocean temperature and salinity profiles and monthly objective analyses with uncertainty estimates. *Journal of Geophysical Research: Oceans*, 118(12), 6704–6716. <https://doi.org/10.1002/2013JC009067>
- Gopalakrishnan, G., Cornuelle, B. D., & Hoteit, I. (2013). Adjoint sensitivity studies of loop current and eddy shedding in the Gulf of Mexico. *Journal of Geophysical Research: Oceans*, 118(7), 3315–3335. <https://doi.org/10.1002/jgrc.20240>
- Gröger, M., Dutheil, C., Börgel, F., & Meier, M. H. E. (2024). Drivers of marine heatwaves in a stratified marginal sea. *Climate Dynamics*, 62(5), 3231–3243. <https://doi.org/10.1007/s00382-023-07062-5>
- Guo, X., and coauthors. (2024). Intensification of future subsurface marine heatwaves in an eddy-resolving model. *Nature Communications*, 15(1), 10777. <https://doi.org/10.1038/s41467-024-54946-z>
- Ha, K.-J., and coauthors. (2022). Dynamics and characteristics of dry and moist heatwaves over East Asia. *Npj Climate and Atmospheric Science*, 5(1), 1–11. <https://doi.org/10.1038/s41612-022-00272-4>
- Hartog, J. R., Spillman, C. M., Smith, G., & Hobday, A. J. (2023). Forecasts of marine heatwaves for marine industries: Reducing risk, building resilience and enhancing management responses. *Deep Sea Research Part II: Topical Studies in Oceanography*, 209, 105276. <https://doi.org/10.1016/j.dsr2.2023.105276>
- Hayashida, H., Matear, R. J., Strutton, P. G., & Zhang, X. (2020). Insights into projected changes in marine heatwaves from a high-resolution ocean circulation model. *Nature Communications*, 11(1), 4352. <https://doi.org/10.1038/s41467-020-18241-x>
- Hayden, E. E., & O’Neill, L. W. (2023). Processes Contributing to Bering Sea Temperature Variability in the Late Twentieth and Early Twenty-First Century. *Journal of Climate*, 37(1), 41–58. <https://doi.org/10.1175/JCLI-D-23-0331.1>
- Heede, U. K., & Fedorov, A. V. (2023). Colder Eastern Equatorial Pacific and Stronger Walker Circulation in the Early 21st Century: Separating the Forced Response to Global Warming From Natural Variability. *Geophysical Research Letters*, 50(3), e2022GL101020. <https://doi.org/10.1029/2022GL101020>

- Heimbach, P., Hill, C., & Giering, R. (2005). An efficient exact adjoint of the parallel MIT General Circulation Model, generated via automatic differentiation. *Future Generation Computer Systems*, 21(8), 1356–1371. <https://doi.org/10.1016/j.future.2004.11.010>
- Heimbach, P., & Losch, M. (2012). Adjoint sensitivities of sub-ice-shelf melt rates to ocean circulation under the Pine Island Ice Shelf, West Antarctica. *Annals of Glaciology*, 53(60), 59–69. <https://doi.org/10.3189/2012/AoG60A025>
- Heimbach, P., Menemenlis, D., Losch, M., Campin, J.-M., & Hill, C. (2010). On the formulation of sea-ice models. Part 2: Lessons from multi-year adjoint sea-ice export sensitivities through the Canadian Arctic Archipelago. *Ocean Modelling*, 33(1), 145–158. <https://doi.org/10.1016/j.ocemod.2010.02.002>
- Hersbach, H., and coauthors. (2020). The ERA5 global reanalysis. *Quarterly Journal of the Royal Meteorological Society*, 146(730), 1999–2049. <https://doi.org/10.1002/qj.3803>
- Hibler, W. D. (1980). Modeling a Variable Thickness Sea Ice Cover. *Monthly Weather Review*, 108(12), 1943–1973. [https://doi.org/10.1175/1520-0493\(1980\)108<1943:MAVTSI>2.0.CO;2](https://doi.org/10.1175/1520-0493(1980)108<1943:MAVTSI>2.0.CO;2)
- Hill, C., Bugnion, V., Follows, M., & Marshall, J. (2004). Evaluating carbon sequestration efficiency in an ocean circulation model by adjoint sensitivity analysis. *Journal of Geophysical Research: Oceans*, 109(C11). <https://doi.org/10.1029/2002JC001598>
- Hobday, A. J., and coauthors. (2016). A hierarchical approach to defining marine heatwaves. *Progress in Oceanography*, 141, 227–238. <https://doi.org/10.1016/j.pocean.2015.12.014>
- Hobday, A. J., Oliver, E. C. J., Gupta, A. S., Benthuisen, J. A., & Burrows, M. T. (2018). Categorizing and Naming Marine Heatwaves. *Oceanography*, 31(2), 162–173. <https://doi.org/10.5670/oceanog.2018.205>
- Holbrook, N. J., and coauthors. (2019). A global assessment of marine heatwaves and their drivers. *Nature Communications*, 10(1), 2624. <https://doi.org/10.1038/s41467-019-10206-z>
- Holbrook, N. J., and coauthors. (2020). Keeping pace with marine heatwaves. *Nature Reviews Earth & Environment*, 1(9), 482–493. <https://doi.org/10.1038/s43017-020-0068-4>
- Hu, D., and coauthors. (2015). Pacific western boundary currents and their roles in climate. *Nature*, 522(7556), 299–308. <https://doi.org/10.1038/nature14504>

- Huang, B., and coauthors. (2021). Improvements of the Daily Optimum Interpolation Sea Surface Temperature (DOISST) Version 2.1. *Journal of Climate*, 34(8), 2923–2939. <https://doi.org/10.1175/JCLI-D-20-0166.1>
- Huang, B., and coauthors. (2017). Extended Reconstructed Sea Surface Temperature, Version 5 (ERSSTv5): Upgrades, Validations, and Intercomparisons. *Journal of Climate*, 30(20), 8179–8205. <https://doi.org/10.1175/JCLI-D-16-0836.1>
- Hunke, E., & Lipscomb, W. (2010). CICE: The Los Alamos sea ice model documentation and software user's manual version 4.0 LA-CC-06-012. *Tech. Rep. LA-CC-06-012*.
- Intergovernmental Panel on Climate Change (IPCC). (2023). *Climate Change 2021 – The Physical Science Basis: Working Group I Contribution to the Sixth Assessment Report of the Intergovernmental Panel on Climate Change*. Cambridge University Press. <https://doi.org/10.1017/9781009157896>
- Jacox, M. G., and coauthors. (2022). Global seasonal forecasts of marine heatwaves. *Nature*, 604(7906), 486–490. <https://doi.org/10.1038/s41586-022-04573-9>
- Jacox, M. G., Alexander, M. A., Bograd, S. J., & Scott, J. D. (2020). Thermal displacement by marine heatwaves. *Nature*, 584(7819), 82–86. <https://doi.org/10.1038/s41586-020-2534-z>
- Jain, P., Sharma, A. R., Acuna, D. C., Abatzoglou, J. T., & Flannigan, M. (2024). Record-breaking fire weather in North America in 2021 was initiated by the Pacific northwest heat dome. *Communications Earth & Environment*, 5(1), 1–10. <https://doi.org/10.1038/s43247-024-01346-2>
- Ji, K., Yu, J.-Y., Li, J., Hu, Z.-Z., Tseng, Y.-H., Shi, J., Zhao, Y., Sun, C., & Ding, R. (2024). Enhanced North Pacific Victoria mode in a warming climate. *Npj Climate and Atmospheric Science*, 7(1), 1–8. <https://doi.org/10.1038/s41612-024-00599-0>
- Joh, Y., and coauthors. (2023). The role of upper-ocean variations of the Kuroshio-Oyashio Extension in seasonal-to-decadal air-sea heat flux variability. *Npj Climate and Atmospheric Science*, 6(1), 1–11. <https://doi.org/10.1038/s41612-023-00453-9>
- Joh, Y., & Di Lorenzo, E. (2017). Increasing Coupling Between NPGO and PDO Leads to Prolonged Marine Heatwaves in the Northeast Pacific. *Geophysical Research Letters*, 44(22), 11,663–11,671. <https://doi.org/10.1002/2017GL075930>

- Joh, Y., Di Lorenzo, E., Siqueira, L., & Kirtman, B. P. (2021). Enhanced interactions of Kuroshio Extension with tropical Pacific in a changing climate. *Scientific Reports*, *11*(1), 6247. <https://doi.org/10.1038/s41598-021-85582-y>
- Johnson, G. C., and coauthors. (2023). Global Oceans. *Bulletin of the American Meteorological Society*, *104*(9), S146–S206. <https://doi.org/10.1175/BAMS-D-23-0076.2>
- Jones, D. C., and coauthors. (2019). Heat Distribution in the Southeast Pacific Is Only Weakly Sensitive to High-Latitude Heat Flux and Wind Stress. *Journal of Geophysical Research: Oceans*, *124*(12), 8647–8666. <https://doi.org/10.1029/2019JC015460>
- Jones, D. C., and coauthors. (2018). Local and Remote Influences on the Heat Content of the Labrador Sea: An Adjoint Sensitivity Study. *Journal of Geophysical Research: Oceans*, *123*(4), 2646–2667. <https://doi.org/10.1002/2018JC013774>
- Joyce, P. W. S., Tong, C. B., Yip, Y. L., & Falkenberg, L. J. (2023). Marine heatwaves as drivers of biological and ecological change: Implications of current research patterns and future opportunities. *Marine Biology*, *171*(1), 20. <https://doi.org/10.1007/s00227-023-04340-y>
- Kajtar, J. B., Bachman, S. D., Holbrook, N. J., & Pilo, G. S. (2022). Drivers, Dynamics, and Persistence of the 2017/2018 Tasman Sea Marine Heatwave. *Journal of Geophysical Research: Oceans*, *127*(8), e2022JC018931. <https://doi.org/10.1029/2022JC018931>
- Kalnay, E., and coauthors. (1996). The NCEP/NCAR 40-Year Reanalysis Project. *Bulletin of the American Meteorological Society*, *77*(3), 437–472. [https://doi.org/10.1175/1520-0477\(1996\)077<0437:TNYRP>2.0.CO;2](https://doi.org/10.1175/1520-0477(1996)077<0437:TNYRP>2.0.CO;2)
- Kawakami, Y., Nakano, H., Urakawa, L. S., Toyoda, T., Aoki, K., & Usui, N. (2023). Northward shift of the Kuroshio Extension during 1993–2021. *Scientific Reports*, *13*(1), 16223. <https://doi.org/10.1038/s41598-023-43009-w>
- Kerry, C., Roughan, M., & Azevedo Correia de Souza, J. M. (2022). Drivers of upper ocean heat content extremes around New Zealand revealed by Adjoint Sensitivity Analysis. *Frontiers in Climate*, *4*. <https://doi.org/10.3389/fclim.2022.980990>
- Kistler, R., and coauthors. (2001). The NCEP–NCAR 50-Year Reanalysis: Monthly Means CD-ROM and Documentation. *Bulletin of the American Meteorological Society*, *82*(2), 247–268. [https://doi.org/10.1175/1520-0477\(2001\)082<0247:TNNYRM>2.3.CO;2](https://doi.org/10.1175/1520-0477(2001)082<0247:TNNYRM>2.3.CO;2)

- Köhl, A., & Stammer, D. (2004). Optimal Observations for Variational Data Assimilation. *Journal of Physical Oceanography*, *34*(3), 529–542. <https://doi.org/10.1175/2513.1>
- Köhl, A., Stammer, D., & Cornuelle, B. (2007). Interannual to Decadal Changes in the ECCO Global Synthesis. *Journal of Physical Oceanography*, *37*(2), 313–337. <https://doi.org/10.1175/JPO3014.1>
- Köhl, A., & Vlasenko, A. (2019). Seasonal Prediction of Northern European Winter Air Temperatures From SST Anomalies Based on Sensitivity Estimates. *Geophysical Research Letters*, *46*(11), 6109–6117. <https://doi.org/10.1029/2018GL081800>
- Kuo, Y.-C., & Tseng, Y.-H. (2021). Influence of anomalous low-level circulation on the Kuroshio in the Luzon Strait during ENSO. *Ocean Modelling*, *159*, 101759. <https://doi.org/10.1016/j.ocemod.2021.101759>
- Kuroda, H., & Setou, T. (2021). Extensive Marine Heatwaves at the Sea Surface in the Northwestern Pacific Ocean in Summer 2021. *Remote Sensing*, *13*(19), Article 19. <https://doi.org/10.3390/rs13193989>
- Large, W. G., McWilliams, J. C., & Doney, S. C. (1994). Oceanic vertical mixing: A review and a model with a nonlocal boundary layer parameterization. *Reviews of Geophysics*, *32*(4), 363–403. <https://doi.org/10.1029/94RG01872>
- Latif, M., and coauthors. (2023). Strengthening atmospheric circulation and trade winds slowed tropical Pacific surface warming. *Communications Earth & Environment*, *4*(1), 1–10. <https://doi.org/10.1038/s43247-023-00912-4>
- Levitus, S., & Boyer, T. P. (1994). *World Ocean Atlas 1994. Vol. 4, Temperature*. <https://repository.library.noaa.gov/view/noaa/1381>
- L’Her, A., Reinert, M., Prants, S., Carton, X., & Morvan, M. (2021). Eddy formation in the bays of Kamchatka and fluxes to the open ocean. *Ocean Dynamics*, *71*(5), 601–612. <https://doi.org/10.1007/s10236-021-01449-w>
- Li, D., Chen, Y., Qi, J., Zhu, Y., Lu, C., & Yin, B. (2023). Attribution of the July 2021 Record-Breaking Northwest Pacific Marine Heatwave to Global Warming, Atmospheric Circulation, and ENSO. *Bulletin of the American Meteorological Society*, *104*(1), E291–E297. <https://doi.org/10.1175/BAMS-D-22-0142.1>
- Li, S., & Hu, S. (2024). Evolution and Drivers of Extreme Subsurface Marine Heatwaves in the Western Tropical Pacific Ocean during 2008 and 2010–11. *Journal of Climate*, *37*(22), 6047–6059. <https://doi.org/10.1175/JCLI-D-24-0079.1>

- Li, Z., Holbrook, N. J., Zhang, X., Oliver, E. C. J., & Cougnon, E. A. (2020). Remote Forcing of Tasman Sea Marine Heatwaves. *Journal of Climate*, 33(12), 5337–5354. <https://doi.org/10.1175/JCLI-D-19-0641.1>
- Li, Z., Wu, G., Xu, C., Zhu, X.-H., & Long, Y. (2024). Summer marine heatwaves in the tropical Indian Ocean associated with an unseasonable positive Indian Ocean Dipole event 2012. *Frontiers in Marine Science*, 11. <https://doi.org/10.3389/fmars.2024.1425813>
- Lin, J., & Qian, T. (2019). A New Picture of the Global Impacts of El Niño-Southern Oscillation. *Scientific Reports*, 9(1), 17543. <https://doi.org/10.1038/s41598-019-54090-5>
- Liu, K., Xu, K., Zhu, C., & Liu, B. (2022). Diversity of Marine Heatwaves in the South China Sea Regulated by ENSO Phase. *Journal of Climate*, 35(2), 877–893. <https://doi.org/10.1175/JCLI-D-21-0309.1>
- Liu, Y., Sun, C., & Li, J. (2023). Nonidentical mechanisms behind the North Pacific summer Blob events in the Satellite Era. *Climate Dynamics*, 61(1), 507–518. <https://doi.org/10.1007/s00382-022-06584-8>
- Losch, M., & Heimbach, P. (2007). Adjoint Sensitivity of an Ocean General Circulation Model to Bottom Topography. *Journal of Physical Oceanography*, 37(2), 377–393. <https://doi.org/10.1175/JPO3017.1>
- Losch, M., Menemenlis, D., Campin, J.-M., Heimbach, P., & Hill, C. (2010). On the formulation of sea-ice models. Part 1: Effects of different solver implementations and parameterizations. *Ocean Modelling*, 33(1), 129–144. <https://doi.org/10.1016/j.ocemod.2009.12.008>
- Madec, G., Delécluse, P., Imbard, M., & Lévy, C. (1998). OPA 8.1 Ocean General Circulation Model reference manual. *Notes Du Pôle de Modélisation, Laboratoire d’océanographie Dynamique et de Climatologie, Institut Pierre Simon Laplace Des Sciences de l’environnement Global*, 11.
- Marotzke, J., Giering, R., Zhang, K. Q., Stammer, D., Hill, C., & Lee, T. (1999). Construction of the adjoint MIT ocean general circulation model and application to Atlantic heat transport sensitivity. *Journal of Geophysical Research: Oceans*, 104(C12), 29529–29547. <https://doi.org/10.1029/1999JC900236>

- Marshall, J., Adcroft, A., Hill, C., Perelman, L., & Heisey, C. (1997a). A finite-volume, incompressible Navier Stokes model for studies of the ocean on parallel computers. *Journal of Geophysical Research: Oceans*, 102(C3), 5753–5766. <https://doi.org/10.1029/96JC02775>
- Marshall, J., Hill, C., Perelman, L., & Adcroft, A. (1997b). Hydrostatic, quasi-hydrostatic, and nonhydrostatic ocean modeling. *Journal of Geophysical Research: Oceans*, 102(C3), 5733–5752. <https://doi.org/10.1029/96JC02776>
- Mazloff, M. R. (2012). On the Sensitivity of the Drake Passage Transport to Air–Sea Momentum Flux. *Journal of Climate*, 25(7), 2279–2290. <https://doi.org/10.1175/JCLI-D-11-00030.1>
- McAdam, R., Masina, S., & Gualdi, S. (2023). Seasonal forecasting of subsurface marine heatwaves. *Communications Earth & Environment*, 4(1), 1–11. <https://doi.org/10.1038/s43247-023-00892-5>
- Mohamed, B., Nilsen, F., & Skogseth, R. (2022). Marine Heatwaves Characteristics in the Barents Sea Based on High Resolution Satellite Data (1982–2020). *Frontiers in Marine Science*, 9. <https://doi.org/10.3389/fmars.2022.821646>
- Moisan, J. R., & Niiler, P. P. (1998). The Seasonal Heat Budget of the North Pacific: Net Heat Flux and Heat Storage Rates (1950–1990). *Journal of Physical Oceanography*, 28(3), 401–421. [https://doi.org/10.1175/1520-0485\(1998\)028<0401:TSHBOT>2.0.CO;2](https://doi.org/10.1175/1520-0485(1998)028<0401:TSHBOT>2.0.CO;2)
- NASA Goddard Space Flight Center, A. (2024). *Sea surface temperature from MODIS*. <https://www.cen.uni-hamburg.de/en/icdc/data/ocean/sst-modis.html>
- National Centers for Environmental Information (NCEI). (2022a). *Monthly Climate Reports / Global Climate Report | Annual 2022 | National Centers for Environmental Information (NCEI)*. <https://www.ncei.noaa.gov/access/monitoring/monthly-report/global/202213>
- National Centers for Environmental Information (NCEI). (2022b). *Monthly Climate Reports / Global Climate Report | July 2022 | National Centers for Environmental Information (NCEI)*. <https://www.ncei.noaa.gov/access/monitoring/monthly-report/global/202207>
- National Geophysical Data Center. (1993). *ETOPO5 Global Earth Topography, 5-minute, from NGDC* [Dataset]. Research Data Archive at the National Center for Atmospheric Research, Computational and Information Systems Laboratory. <https://rda.ucar.edu/datasets/dsd759001/>

- Navarra, G. G., & Di Lorenzo, E. (2021). Poleward shift and intensified variability of Kuroshio-Oyashio extension and North Pacific Transition Zone under climate change. *Climate Dynamics*, 56(7), 2469–2486. <https://doi.org/10.1007/s00382-021-05677-0>
- Niu, X., Chen, Y., & Le, C. (2023). Northeast Pacific marine heatwaves associated with high-latitude atmospheric blocking. *Environmental Research Letters*, 19(1), 014025. <https://doi.org/10.1088/1748-9326/ad0e35>
- NOAA Physical Sciences Laboratory. (2024). *Marine Heatwaves: NOAA Physical Sciences Laboratory*. <https://psl.noaa.gov/marine-heatwaves/>
- Noh, E., Kim, J., Jun, S.-Y., Pak, G., Kim, J.-H., & Kim, H.-G. (2023). Atmospheric pathway of marine heatwaves over the Northwestern Pacific. *Scientific Reports*, 13(1), 22821. <https://doi.org/10.1038/s41598-023-49833-4>
- Oh, H., Kim, G.-U., Chu, J.-E., Lee, K., & Jeong, J.-Y. (2023). The record-breaking 2022 long-lasting marine heatwaves in the East China Sea. *Environmental Research Letters*, 18(6), 064015. <https://doi.org/10.1088/1748-9326/acd267>
- Oliver, E. C. J. (2019). Mean warming not variability drives marine heatwave trends. *Climate Dynamics*, 53(3), 1653–1659. <https://doi.org/10.1007/s00382-019-04707-2>
- Oliver, E. C. J., and coauthors. (2021). Marine Heatwaves. *Annual Review of Marine Science*, 13(Volume 13, 2021), 313–342. <https://doi.org/10.1146/annurev-marine-032720-095144>
- Oliver, E. C. J., Lago, V., Hobday, A. J., Holbrook, N. J., Ling, S. D., & Mundy, C. N. (2018). Marine heatwaves off eastern Tasmania: Trends, interannual variability, and predictability. *Progress in Oceanography*, 161, 116–130. <https://doi.org/10.1016/j.pocean.2018.02.007>
- Pak, G., Noh, J., Park, Y.-G., Jin, H., & Park, J.-H. (2022). Governing factors of the record-breaking marine heatwave over the mid-latitude western North Pacific in the summer of 2021. *Frontiers in Marine Science*, 9. <https://doi.org/10.3389/fmars.2022.946767>
- Pearce, A. F., & Feng, M. (2013). The rise and fall of the “marine heat wave” off Western Australia during the summer of 2010/2011. *Journal of Marine Systems*, 111–112, 139–156. <https://doi.org/10.1016/j.jmarsys.2012.10.009>
- Pearce, A., Jackson, G., Moore, J., Feng, M., & Gaughan, D. (2011). The “marine heat wave” off Western Australia during the summer of 2010/11. *Fisheries Research Reports*. [https://library.dpird.wa.gov.au/fr\\_rr/15](https://library.dpird.wa.gov.au/fr_rr/15)

- Perkins, S. E., & Alexander, L. V. (2013). On the Measurement of Heat Waves. *Journal of Climate*, 26(13), 4500–4517. <https://doi.org/10.1175/JCLI-D-12-00383.1>
- Perkins, S. E., & Lewis, S. C. (2020). Increasing trends in regional heatwaves. *Nature Communications*, 11(1), 3357. <https://doi.org/10.1038/s41467-020-16970-7>
- Peterson, W., Robert, M., & Bond, N. (2015). The warm blob—Conditions in the northeastern Pacific Ocean. *PICES Press*, 23(1), 36–38. <https://www.proquest.com/scholarly-journals/warm-blob-conditions-northeastern-pacific-ocean/docview/1665110669/se-2?accountid=11262>
- Pfahl, S., & Wernli, H. (2012). Quantifying the relevance of atmospheric blocking for co-located temperature extremes in the Northern Hemisphere on (sub-)daily time scales. *Geophysical Research Letters*, 39(12). <https://doi.org/10.1029/2012GL052261>
- Pinault, J.-L. (2022). A Review of the Role of the Oceanic Rossby Waves in Climate Variability. *Journal of Marine Science and Engineering*, 10(4), Article 4. <https://doi.org/10.3390/jmse10040493>
- Plecha, S. M., & Soares, P. M. M. (2020). Global marine heatwave events using the new CMIP6 multi-model ensemble: From shortcomings in present climate to future projections. *Environmental Research Letters*, 15(12), 124058. <https://doi.org/10.1088/1748-9326/abc847>
- Qiao, Y.-X., Nakamura, H., & Tomita, T. (2024). Warming of the Kuroshio Current Over the Last Four Decades has Intensified the Meiyu-Baiu Rainband. *Geophysical Research Letters*, 51(2), e2023GL107021. <https://doi.org/10.1029/2023GL107021>
- Qiu, B. (2002). The Kuroshio Extension System: Its Large-Scale Variability and Role in the Midlatitude Ocean-Atmosphere Interaction. *Journal of Oceanography*, 58(1), 57–75. <https://doi.org/10.1023/A:1015824717293>
- Qiu, Z., Qiao, F., Jang, C. J., Zhang, L., & Song, Z. (2021). Evaluation and projection of global marine heatwaves based on CMIP6 models. *Deep Sea Research Part II: Topical Studies in Oceanography*, 194, 104998. <https://doi.org/10.1016/j.dsr2.2021.104998>
- Radfar, S., Moftakhari, H., & Moradkhani, H. (2024). Rapid intensification of tropical cyclones in the Gulf of Mexico is more likely during marine heatwaves. *Communications Earth & Environment*, 5(1), 1–13. <https://doi.org/10.1038/s43247-024-01578-2>

- Rallu De Malibrán, M. C., Kaplan, C. M., & Di Lorenzo, E. (2024). Marine heatwaves suppress ocean circulation and large vortices in the Gulf of Alaska. *Communications Earth & Environment*, 5(1), 1–12. <https://doi.org/10.1038/s43247-024-01785-x>
- Rayner, N. A., and coauthors. (2003). Global analyses of sea surface temperature, sea ice, and night marine air temperature since the late nineteenth century. *Journal of Geophysical Research: Atmospheres*, 108(D14). <https://doi.org/10.1029/2002JD002670>
- Ren, X., Liu, W., Capotondi, A., Amaya, D. J., & Holbrook, N. J. (2023). The Pacific Decadal Oscillation modulated marine heatwaves in the Northeast Pacific during past decades. *Communications Earth & Environment*, 4(1), 1–9. <https://doi.org/10.1038/s43247-023-00863-w>
- Reynolds, C. A., Doyle, J. D., Ralph, F. M., & Demirdjian, R. (2019). Adjoint Sensitivity of North Pacific Atmospheric River Forecasts. *Monthly Weather Review*, 147(6), 1871–1897. <https://doi.org/10.1175/MWR-D-18-0347.1>
- Richaud, B., Hu, X., Darmaraki, S., Fennel, K., Lu, Y., & Oliver, E. C. J. (2024). Drivers of Marine Heatwaves in the Arctic Ocean. *Journal of Geophysical Research: Oceans*, 129(2), e2023JC020324. <https://doi.org/10.1029/2023JC020324>
- Rodrigues, R. R., Taschetto, A. S., Sen Gupta, A., & Foltz, G. R. (2019). Common cause for severe droughts in South America and marine heatwaves in the South Atlantic. *Nature Geoscience*, 12(8), 620–626. <https://doi.org/10.1038/s41561-019-0393-8>
- Roeckner, E., and coauthors. (1996). *The atmospheric general circulation model ECHAM-4: Model description and simulation of present-day climate*. <https://doi.org/10.17617/2.1781494>
- Rousi, E., Kornhuber, K., Beobide-Arsuaga, G., Luo, F., & Coumou, D. (2022). Accelerated western European heatwave trends linked to more-persistent double jets over Eurasia. *Nature Communications*, 13(1), 3851. <https://doi.org/10.1038/s41467-022-31432-y>
- Russo, S., Sillmann, J., & Fischer, E. M. (2015). Top ten European heatwaves since 1950 and their occurrence in the coming decades. *Environmental Research Letters*, 10(12), 124003. <https://doi.org/10.1088/1748-9326/10/12/124003>
- Scannell, H. A., Johnson, G. C., Thompson, L., Lyman, J. M., & Riser, S. C. (2020). Subsurface Evolution and Persistence of Marine Heatwaves in the Northeast Pacific. *Geophysical Research Letters*, 47(23), e2020GL090548. <https://doi.org/10.1029/2020GL090548>

- Scannell, H. A., Pershing, A. J., Alexander, M. A., Thomas, A. C., & Mills, K. E. (2016). Frequency of marine heatwaves in the North Atlantic and North Pacific since 1950. *Geophysical Research Letters*, *43*(5), 2069–2076. <https://doi.org/10.1002/2015GL067308>
- Schaller, N., Sillmann, J., Anstey, J., Fischer, E. M., Grams, C. M., & Russo, S. (2018). Influence of blocking on Northern European and Western Russian heatwaves in large climate model ensembles. *Environmental Research Letters*, *13*(5), 054015. <https://doi.org/10.1088/1748-9326/aaba55>
- Schlegel, R. W., Oliver, E. C. J., Perkins-Kirkpatrick, S., Kruger, A., & Smit, A. J. (2017). Predominant Atmospheric and Oceanic Patterns during Coastal Marine Heatwaves. *Frontiers in Marine Science*, *4*. <https://doi.org/10.3389/fmars.2017.00323>
- Schmeisser, L., Bond, N. A., Siedlecki, S. A., & Ackerman, T. P. (2019). The Role of Clouds and Surface Heat Fluxes in the Maintenance of the 2013–2016 Northeast Pacific Marine Heatwave. *Journal of Geophysical Research: Atmospheres*, *124*(20), 10772–10783. <https://doi.org/10.1029/2019JD030780>
- Schneider, N., Miller, A. J., & Pierce, D. W. (2002). Anatomy of North Pacific Decadal Variability. *Journal of Climate*, *15*(6), 586–605. [https://doi.org/10.1175/1520-0442\(2002\)015<0586:AONPDV>2.0.CO;2](https://doi.org/10.1175/1520-0442(2002)015<0586:AONPDV>2.0.CO;2)
- Sen Gupta, A., and coauthors. (2020). Drivers and impacts of the most extreme marine heatwave events. *Scientific Reports*, *10*(1), 19359. <https://doi.org/10.1038/s41598-020-75445-3>
- Shi, J., and coauthors. (2024a). Northeast Pacific warm blobs sustained via extratropical atmospheric teleconnections. *Nature Communications*, *15*(1), 2832. <https://doi.org/10.1038/s41467-024-47032-x>
- Shi, Y., Xu, X., Liu, T., Yang, G., Liu, S., Lyu, J., Zhang, S., Sheng, H., & Gao, J. (2024b). Recent warming of the Kuroshio Current has promoted offshore sediment transport in the Yellow Sea. *Limnology and Oceanography Letters*, *9*(4), 452–460. <https://doi.org/10.1002/lol2.10396>
- Silva, E. N. S., & Anderson, B. T. (2023). Northeast Pacific marine heatwaves linked to Kuroshio Extension variability. *Communications Earth & Environment*, *4*(1), 1–11. <https://doi.org/10.1038/s43247-023-01010-1>

- Silva, E. N. S., & Anderson, B. T. (2024). Influence of Kuroshio Extension's sea surface temperature variability on the North Pacific atmosphere and Pacific Decadal Precession. *Climate Dynamics*, 62(9), 8947–8960. <https://doi.org/10.1007/s00382-024-07372-2>
- Smale, D. A., and coauthors. (2019). Marine heatwaves threaten global biodiversity and the provision of ecosystem services. *Nature Climate Change*, 9(4), 306–312. <https://doi.org/10.1038/s41558-019-0412-1>
- Smith, K. E., and coauthors. (2023). Biological Impacts of Marine Heatwaves. *Annual Review of Marine Science*, 15(Volume 15, 2023), 119–145. <https://doi.org/10.1146/annurev-marine-032122-121437>
- Smith, K. E., and coauthors. (2021). Socioeconomic impacts of marine heatwaves: Global issues and opportunities. *Science*, 374(6566), eabj3593. <https://doi.org/10.1126/science.abj3593>
- Smith, K. E., and coauthors. (2025). Baseline matters: Challenges and implications of different marine heatwave baselines. *Progress in Oceanography*, 231, 103404. <https://doi.org/10.1016/j.pocean.2024.103404>
- Song, Q., Wang, C., Yao, Y., & Fan, H. (2024). Unraveling the Indian monsoon's role in fueling the unprecedented 2022 Marine Heatwave in the Western North Pacific. *Npj Climate and Atmospheric Science*, 7(1), 1–8. <https://doi.org/10.1038/s41612-024-00645-x>
- Song, Q., Yao, Y., & Wang, C. (2023a). Response of Future Summer Marine Heatwaves in the South China Sea to Enhanced Western Pacific Subtropical High. *Geophysical Research Letters*, 50(14), e2023GL103667. <https://doi.org/10.1029/2023GL103667>
- Song, S.-Y., Yeh, S.-W., Kim, H., & Holbrook, N. J. (2023b). Arctic warming contributes to increase in Northeast Pacific marine heatwave days over the past decades. *Communications Earth & Environment*, 4(1), 1–9. <https://doi.org/10.1038/s43247-023-00683-y>
- Spillman, C. M., Smith, G. A., Hobday, A. J., & Hartog, J. R. (2021). Onset and Decline Rates of Marine Heatwaves: Global Trends, Seasonal Forecasts and Marine Management. *Frontiers in Climate*, 3. <https://doi.org/10.3389/fclim.2021.801217>

- Stabeno, Thoman, & Wood. (2019). Recent Warming in the Bering Sea and Its Impact on the Ecosystem. *NOAA Arctic*. <https://arctic.noaa.gov/report-card/report-card-2019/recent-warming-in-the-bering-sea-and-its-impact-on-the-ecosystem/>
- Stammer, D., Köhl, A., Vlasenko, A., Matei, I., Lunkeit, F., & Schubert, S. (2018). A Pilot Climate Sensitivity Study Using the CEN Coupled Adjoint Model (CESAM). *Journal of Climate*, *31*(5), 2031–2056. <https://doi.org/10.1175/JCLI-D-17-0183.1>
- Stammer, D., and coauthors. (2002). Global ocean circulation during 1992–1997, estimated from ocean observations and a general circulation model. *Journal of Geophysical Research: Oceans*, *107*(C9), 1-1-1–27. <https://doi.org/10.1029/2001JC000888>
- Stefanon, M., D’Andrea, F., & Drobinski, P. (2012). Heatwave classification over Europe and the Mediterranean region. *Environmental Research Letters*, *7*(1), 014023. <https://doi.org/10.1088/1748-9326/7/1/014023>
- Stott, P. A., Stone, D. A., & Allen, M. R. (2004). Human contribution to the European heatwave of 2003. *Nature*, *432*(7017), 610–614. <https://doi.org/10.1038/nature03089>
- Sun, D., Li, F., Jing, Z., Hu, S., & Zhang, B. (2023). Frequent marine heatwaves hidden below the surface of the global ocean. *Nature Geoscience*, *16*(12), 1099–1104. <https://doi.org/10.1038/s41561-023-01325-w>
- Sung, M.-K. (2025). Chapter 6—North Pacific Oscillation. In B. Guan (Ed.), *Atmospheric Oscillations* (pp. 121–136). Elsevier. <https://doi.org/10.1016/B978-0-443-15638-0.00006-X>
- Tan, H.-J., Cai, R.-S., & Wu, R.-G. (2022). Summer marine heatwaves in the South China Sea: Trend, variability and possible causes. *Advances in Climate Change Research*, *13*(3), 323–332. <https://doi.org/10.1016/j.accre.2022.04.003>
- Travkin, V. S., Tikhonova, N. A., & Zakharchuk, E. A. (2024). Characteristics of Marine Heatwaves of the Baltic Sea for 1993–2022 and Their Driving Factors. *Pure and Applied Geophysics*, *181*(7), 2373–2387. <https://doi.org/10.1007/s00024-024-03504-1>
- Trenberth, K. E., & Fasullo, J. T. (2013). An apparent hiatus in global warming? *Earth’s Future*, *1*(1), 19–32. <https://doi.org/10.1002/2013EF000165>
- Tuchen, F. P., Perez, R. C., Foltz, G. R., McPhaden, M. J., & Lumpkin, R. (2024). Strengthening of the Equatorial Pacific Upper-Ocean Circulation Over the Past Three Decades. *Journal of Geophysical Research: Oceans*, *129*(11), e2024JC021343. <https://doi.org/10.1029/2024JC021343>

- Veneziani, M., Edwards, C. A., & Moore, A. M. (2009). A central California coastal ocean modeling study: 2. Adjoint sensitivities to local and remote forcing mechanisms. *Journal of Geophysical Research: Oceans*, *114*(C4). <https://doi.org/10.1029/2008JC004775>
- Verdy, A., Mazloff, M. R., Cornuelle, B. D., & Kim, S. Y. (2014). Wind-Driven Sea Level Variability on the California Coast: An Adjoint Sensitivity Analysis. *Journal of Physical Oceanography*, *44*(1), 297–318. <https://doi.org/10.1175/JPO-D-13-018.1>
- Vijith, V., and coauthors. (2020). Closing the sea surface mixed layer temperature budget from in situ observations alone: Operation Advection during BoBBLE. *Scientific Reports*, *10*(1), 7062. <https://doi.org/10.1038/s41598-020-63320-0>
- Wang, B., and coauthors. (2023a). Understanding the recent increase in multiyear La Niñas. *Nature Climate Change*, *13*(10), 1075–1081. <https://doi.org/10.1038/s41558-023-01801-6>
- Wang, J., Liu, C., Wang, X., Köhl, A., Lyu, Y., Li, Y., & Wang, F. (2022a). Wind-Driven Mechanisms for the Variations of the Pacific Equatorial Undercurrent Based on Adjoint Sensitivity Analysis. *Frontiers in Marine Science*, *9*. <https://doi.org/10.3389/fmars.2022.908939>
- Wang, O., and coauthors. (2022b). Local and Remote Forcing of Interannual Sea-Level Variability at Nantucket Island. *Journal of Geophysical Research: Oceans*, *127*(6), e2021JC018275. <https://doi.org/10.1029/2021JC018275>
- Wang, Q., Zhang, B., Zeng, L., He, Y., Wu, Z., & Chen, J. (2022c). Properties and Drivers of Marine Heat Waves in the Northern South China Sea. *Journal of Physical Oceanography*, *52*(5), 917–927. <https://doi.org/10.1175/JPO-D-21-0236.1>
- Wang, X., Liu, C., Köhl, A., Geng, W., Wang, F., & Stammer, D. (2022d). The adjoint-based Two Oceans One Sea State Estimate (TOOSSE). *Journal of Oceanology and Limnology*, *40*(1), 1–21. <https://doi.org/10.1007/s00343-021-0439-9>
- Wang, Y., Zhang, C., Tian, S., Chen, Q., Li, S., Zeng, J., Wei, Z., & Xie, S. (2023b). Seasonal cycle of marine heatwaves in the northern South China Sea. *Climate Dynamics*, *61*(7), 3367–3377. <https://doi.org/10.1007/s00382-023-06747-1>
- Welch, H., and coauthors. (2023). Impacts of marine heatwaves on top predator distributions are variable but predictable. *Nature Communications*, *14*(1), 5188. <https://doi.org/10.1038/s41467-023-40849-y>

- Werb, B. E., & Rudnick, D. L. (2023). Remarkable Changes in the Dominant Modes of North Pacific Sea Surface Temperature. *Geophysical Research Letters*, 50(4), e2022GL101078. <https://doi.org/10.1029/2022GL101078>
- Wernberg, T. (2021). Marine Heatwave Drives Collapse of Kelp Forests in Western Australia. In J. G. Canadell & R. B. Jackson (Eds.), *Ecosystem Collapse and Climate Change* (pp. 325–343). Springer International Publishing. [https://doi.org/10.1007/978-3-030-71330-0\\_12](https://doi.org/10.1007/978-3-030-71330-0_12)
- Wernberg, T., and coauthors. (2016). Climate-driven regime shift of a temperate marine ecosystem. *Science*, 353(6295), 169–172. <https://doi.org/10.1126/science.aad8745>
- Wilson, C., Horsburgh, K. J., Williams, J., Flowerdew, J., & Zanna, L. (2013). Tide-surge adjoint modeling: A new technique to understand forecast uncertainty. *Journal of Geophysical Research: Oceans*, 118(10), 5092–5108. <https://doi.org/10.1002/jgrc.20364>
- Wyatt, A. S. J., Leichter, J. J., Washburn, L., Kui, L., Edmunds, P. J., & Burgess, S. C. (2023). Hidden heatwaves and severe coral bleaching linked to mesoscale eddies and thermocline dynamics. *Nature Communications*, 14(1), 25. <https://doi.org/10.1038/s41467-022-35550-5>
- Xu, T., and coauthors. (2022). An increase in marine heatwaves without significant changes in surface ocean temperature variability. *Nature Communications*, 13(1), 7396. <https://doi.org/10.1038/s41467-022-34934-x>
- Yang, C.-Y., and coauthors. (2024). Observational evidence of overlooked downwelling induced by tropical cyclones in the open ocean. *Scientific Reports*, 14(1), 335. <https://doi.org/10.1038/s41598-023-51016-0>
- Yang, H., and coauthors. (2020). Poleward Shift of the Major Ocean Gyres Detected in a Warming Climate. *Geophysical Research Letters*, 47(5), e2019GL085868. <https://doi.org/10.1029/2019GL085868>
- Yang, S., & Oh, J.-H. (2020). Effects of modes of climate variability on wave power during boreal summer in the western North Pacific. *Scientific Reports*, 10(1), 5187. <https://doi.org/10.1038/s41598-020-62138-0>
- Yang, W., Liu, C., Köhl, A., Wang, J., Wang, X., & Wang, F. (2023). The Adjoint-Based Favorable Winds for the Generation of the Central Pacific El Niño. *Journal of Climate*, 36(16), 5491–5510. <https://doi.org/10.1175/JCLI-D-22-0548.1>

- Yao, Y., & Wang, C. (2021). Variations in Summer Marine Heatwaves in the South China Sea. *Journal of Geophysical Research: Oceans*, 126(10), e2021JC017792. <https://doi.org/10.1029/2021JC017792>
- Yao, Y., Wang, C., & Wang, C. (2023). Record-breaking 2020 summer marine heatwaves in the western North Pacific. *Deep Sea Research Part II: Topical Studies in Oceanography*, 209, 105288. <https://doi.org/10.1016/j.dsr2.2023.105288>
- Yoon, D., Cha, D.-H., Lee, M.-I., Min, K.-H., Kim, J., Jun, S.-Y., & Choi, Y. (2020). Recent changes in heatwave characteristics over Korea. *Climate Dynamics*, 55(7), 1685–1696. <https://doi.org/10.1007/s00382-020-05420-1>
- Zhabin, I. A., Dmitrieva, E. V., Dubina, V. A., & Luchin, V. A. (2022). Variability of Summer Wind-Driven Upwelling along the Koryak Coast in the Northwestern Bering Sea Based on Satellite Data. *Izvestiya, Atmospheric and Oceanic Physics*, 58(12), 1438–1449. <https://doi.org/10.1134/S0001433822120283>
- Zhan, P., Gopalakrishnan, G., Subramanian, A. C., Guo, D., & Hoteit, I. (2018). Sensitivity Studies of the Red Sea Eddies Using Adjoint Method. *Journal of Geophysical Research: Oceans*, 123(11), 8329–8345. <https://doi.org/10.1029/2018JC014531>
- Zhan, W., Feng, M., Zhang, Y., Shen, X., Zhan, H., & He, Q. (2024). Reduced and smaller phytoplankton during marine heatwaves in eastern boundary upwelling systems. *Communications Earth & Environment*, 5(1), 1–11. <https://doi.org/10.1038/s43247-024-01805-w>
- Zhang, W. G., Wilkin, J. L., Levin, J. C., & Arango, H. G. (2009). An Adjoint Sensitivity Study of Buoyancy- and Wind-Driven Circulation on the New Jersey Inner Shelf. *Journal of Physical Oceanography*, 39(7), 1652–1668. <https://doi.org/10.1175/2009JPO4050.1>
- Zhang, X., Cornuelle, B., & Roemmich, D. (2011). Adjoint Sensitivity of the Niño-3 Surface Temperature to Wind Forcing. *Journal of Climate*, 24(16), 4480–4493. <https://doi.org/10.1175/2011JCLI3917.1>
- Zhang, X., Cornuelle, B., & Roemmich, D. (2012). Sensitivity of Western Boundary Transport at the Mean North Equatorial Current Bifurcation Latitude to Wind Forcing. *Journal of Physical Oceanography*, 42(11), 2056–2072. <https://doi.org/10.1175/JPO-D-11-0229.1>

- Zhang, X., Li, F., Jing, Z., Zhang, B., Ma, X., & Du, T. (2024a). Detecting marine heatwaves below the sea surface globally using dynamics-guided statistical learning. *Communications Earth & Environment*, 5(1), 1–9. <https://doi.org/10.1038/s43247-024-01769-x>
- Zhang, X., Zhao, N., Han, Z., & Dai, Z. (2024b). Large spread in marine heatwave assessments for Asia and the Indo-Pacific between sea-surface-temperature products. *Communications Earth & Environment*, 5(1), 1–9. <https://doi.org/10.1038/s43247-024-01369-9>
- Zhang, Y., Zhang, Z., Chen, D., Qiu, B., & Wang, W. (2020). Strengthening of the Kuroshio current by intensifying tropical cyclones. *Science*, 368(6494), 988–993. <https://doi.org/10.1126/science.aax5758>
- Zhao, Y., Chen, M., Chung, T. H., Chan, L. L., & Qiu, J.-W. (2023). The 2022 summer marine heatwaves and coral bleaching in China’s Greater Bay Area. *Marine Environmental Research*, 189, 106044. <https://doi.org/10.1016/j.marenvres.2023.106044>
- Zhao, Y., & Yu, J.-Y. (2023). Two Marine Heatwave (MHW) Variants under a Basinwide MHW Conditioning Mode in the North Pacific and Their Atlantic Associations. *Journal of Climate*, 36(24), 8657–8674. <https://doi.org/10.1175/JCLI-D-23-0156.1>
- Zhao, Z., Holbrook, N. J., & Oliver, E. C. J. (2022). An eddy pathway to marine heatwave predictability off eastern Tasmania. *Frontiers in Climate*, 4. <https://doi.org/10.3389/fclim.2022.907828>
- Zhou, M., & Wang, S. (2024). The risk of concurrent heatwaves and extreme sea levels along the global coastline is increasing. *Communications Earth & Environment*, 5(1), 1–10. <https://doi.org/10.1038/s43247-024-01274-1>
- Zschenderlein, P., Fink, A. H., Pfahl, S., & Wernli, H. (2019). Processes determining heat waves across different European climates. *Quarterly Journal of the Royal Meteorological Society*, 145(724), 2973–2989. <https://doi.org/10.1002/qj.3599>
- Zuo, H., Balmaseda, M. A., Tietsche, S., Mogensen, K., & Mayer, M. (2019). The ECMWF operational ensemble reanalysis–analysis system for ocean and sea ice: A description of the system and assessment. *Ocean Science*, 15(3), 779–808. <https://doi.org/10.5194/os-15-779-2019>

## Data and Code Availability

ETOPO5 data are available at <https://data.ucar.edu/dataset/etopo5-global-earth-topography-5-minute-from-ngdc>.

PDO index is available at <https://climatedataguide.ucar.edu/climate-data/pacific-decadal-oscillation-pdo-definition-and-indices>.

NPGO index is available at <https://marine.copernicus.eu/access-data/ocean-monitoring-indicators/north-pacific-gyre-oscillation-observations-reprocessing>.

ENSO index is available at <https://psl.noaa.gov/data/correlation/nina34.anom.data>.

## Acknowledgments

I would like to express my sincere gratitude to my superiors for their guidance and support throughout this research. Their encouragement and valuable insights have greatly contributed to the development and success of this study.

First of all, I want to especially thank Prof. Dr. Detlef Stammer, who offered me the opportunity to start my PhD in Germany during the COVID-19 pandemic, which helped me emerge from the extended lockdown in my hometown. I truly appreciate his patient attitude and the freedom he granted me to explore the research topics that interest me.

I also want to thank Dr. Armin Köhl for guiding me in numerical modeling and for sharing his brilliant ideas that helped me solve various problems. I would like to express my gratitude to my parents for supporting me in any decisions I made. A special thanks to Hairu, who was the reason I didn't hesitate to come to Germany.

Additionally, I want to thank Kaiyan, Yi, Dong, Chavely, Sri, Philip, Abhirup, and Maite; their companionship made office life much sweeter. I also want to thank the new friends I have met here for their company and support outside of the office.

Last but not least, I want to thank myself for having the courage to embrace this experience.

The whole study is supported by the DFG-funded Koselleck project "EarthRA". All computations were performed at the Deutsches Klima Rechenzentrum (DKRZ), Germany. The German abstract has been generated using a language model (chatGPT) to ensure clarity and logical coherence.

**Eidesstattliche Versicherung | Declaration on Oath**

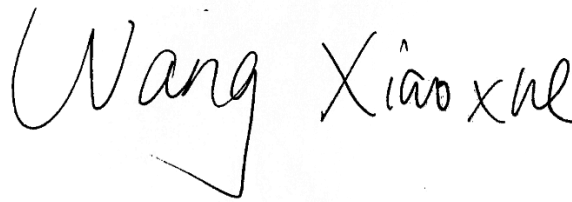
I hereby declare and affirm that this doctoral dissertation is my own work and that I have not used any aids and sources other than those indicated.

If electronic resources based on generative artificial intelligence (gAI) were used in the course of writing this dissertation, I confirm that my own work was the main and value-adding contribution and that complete documentation of all resources used is available in accordance with good scientific practice. I am responsible for any erroneous or distorted content, incorrect references, violations of data protection and copyright law or plagiarism that may have been generated by the gAI.

Ort, den | City, date

Unterschrift | Signature

HAMBURG, 2025, 3, 28

A handwritten signature in black ink that reads "Wang Xiaoxue". The signature is written in a cursive style with a large, sweeping initial 'W'.